Modelling of electronic and transport properties of hybrid perovskites

Antoine Lacroix

THÈSE

Pour obtenir le grade de

DOCTEUR DE L'UNIVERSITE GRENOBLE ALPES

Spécialité : **Physique des matériaux**

Arrêté ministériel : 25 mai 2016

Présentée par

Antoine Lacroix

Thèse dirigée par **Didier Mayou, Directeur de recherche, Institut Néel, CNRS**, et
codirigée par **Jean-Pierre Julien, Maître de conférences, Université Grenoble Alpes**

préparée au sein du **Laboratoire Institut Néel, CNRS**
dans **l'École doctorale de physique**

Modélisation des propriétés électroniques et de transport des pérovskites hybrides

Modelling of electronic and transport properties of hybrid perovskites

Thèse soutenue publiquement le **14 décembre 2020**,
devant le jury composé de :

Madame Marie-Bernadette LEPETIT
Directeur de recherche CNRS, Institut Néel Grenoble, Présidente du jury
Monsieur Nicolas CAVASSILAS
Professeur des universités, Université Aix-Marseille, Rapporteur
Madame Paulina PLOCHOCKA
Directeur de recherche CNRS, LNCMI Toulouse, Rapporteur
Monsieur Dmitry ALDAKOV
Chargé de recherche CNRS, CEA Grenoble, Membre
Monsieur Jean-François GUILLEMOLES
Directeur de recherche CNRS, IPVF Palaiseau, Membre
Monsieur Didier MAYOU
Directeur de recherche CNRS, Institut Néel Grenoble, Directeur de thèse

Invité :

Monsieur Jean-Pierre JULIEN
Maître de conférences, Université Grenoble Alpes, Codirecteur de thèse

"If I have seen further it is by standing on the shoulders of giants."
Isaac Newton

Acknowledgements

This thesis was funded by the Grenoble doctoral school of physics and realised at the Néel Institute, in the PLUM department. I wish to express my gratitude to Etienne Bustarret, the director of the Institute, and to Serge Huant, the head of the department, for allowing this project to happen, and placing their trust in me.

I then wish to thanks my supervisor Didier Mayou, for the three years of guidance, discussion and trust he gave me. From the beginning of my internship, he started building an environment based on trust, in which I never felt under pressure. It gave me the freedom to evolve, both professionally and personally. I always felt respected in my opinions, and this allowed me to discuss and explore different paths, while still benefiting from his incredible knowledge.

I then want to express my gratitude to Jean-Pierre Julien, my co-supervisor. With time, he proved to be a great tutor as well as a friend. I am thankful for his input through the thesis, the opportunity he gave me to teach at the university, and his kind guidance through all of it. Our discussions often exceeded the scope of physics, and were more helpful than I could ever have asked for.

I know both of them went through difficult times during these 3 years, but this never impacted our relation. For this alone, I am grateful.

I also want to thanks and acknowledge the contribution of many colleagues that contributed to this work. Guy Trambly de Laissardière for accompanying me and introducing me to the diffusion algorithm, and Pascal Quémerais, Alain Ibanez, Julien Zaccaro, and Dang Le-Si, for many fruitful discussions during this thesis.

I wish to thanks the members of my jury, Nicolas Cavassilas, Paulina Plochocka, Dmitry Aldakov, Jean-François Guillemoles, and Marie-Bernadette Lepetit, for the

time they invested and their interest in our work. Dmitry Aldakov also participated in my yearly supervisory committee alongside Xavier Blase, and I thank them both for their ongoing involvement, interest, and trust.

This thesis is not only the result of three years of work, but also of a lifetime of support. For this, my thoughts go to my family, both my wonderful parents, and my extraordinary brother and sister. Each of you would deserve a whole section of this thesis, and you are the most valuable thing I have. I do not forget my extended family, my grandparents, uncle and aunts, cousins and little cousins, and I carry each of you in my heart.

I want to express my gratitude towards my friends, who are too numerous to cite. I want to make an exception though for Alexis and Marina, which have become more than friends since the first year of university, and grew into family. You have shaped me more than you probably know, and I am forever grateful. I also want to thank my partner Marie, who was of great comfort and motivation when I deeply needed it. Finally, I wish to thank Juliette for being there during hard and decisive times, through which we both grew a lot.

Last but not least, I want to thank my colleagues, Kevin and Ghassen, who are now gone, and Guillaume and Maxime, who are still here for a little longer. You all made the office a lot more pleasant to come to.

Contents

Chapter 1

Introduction

Contents

Energy is one of the most important matter of modern times and is at the heart of our society's development. It has both become a fundamental human need, improving and sustaining the life of billions around the globe, as well as a limiting factor to what is considered technologically achievable as of now. Furthermore, with the fast technological and economical growth in emerging countries and the increasing consumption in developed countries, this demand is only expected to grow.

To meet this demand, we have relied for the last decades mostly on non-renewable fossil energies, nuclear power, and hydroelectricity, as shown in figure 1.1. However the current ecological crisis linked to global warming, caused by the gases released when burning fossil fuels, and the inherent dangers of nuclear fission, have led to a point where this chase for energy could lead to major catastrophes, not only for mankind, but for all life on earth. In light of this, it has become a major priority to find new and appropriate energy sources, and ways to exploit

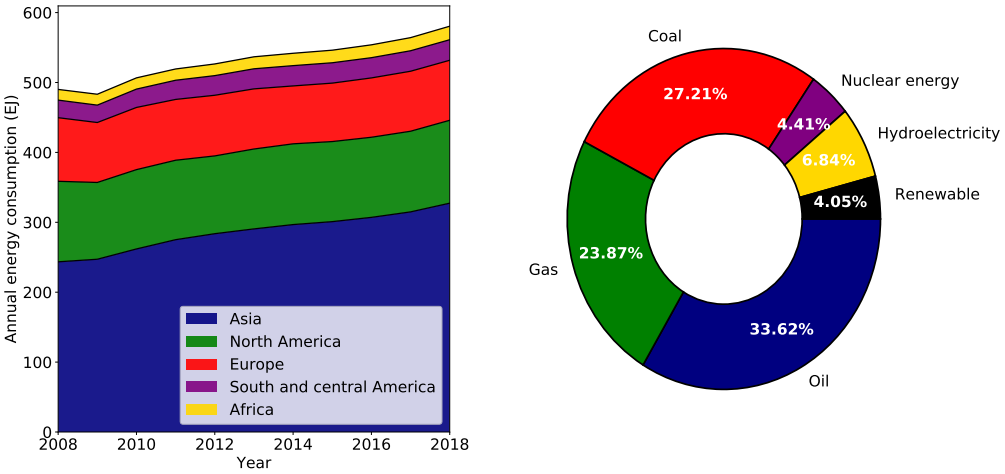

Figure 1.1: Left: World energy consumption over the last years, separated by continent. The general increase is of the order of 2% per year. Right: Primary energy consumption by fuel for the year 2018. Data obtained from [1]

them.

1.1 Earth Energy resources

Let's first take a look at what is available to us on earth. As a thermodynamic system, the planet can receive, produce and even store energy over time.

- Power earth receives from outer space mostly comes from the sun, in the form of radiation ranging from infrared to gamma rays. The estimation for the total power received per square meter perpendicular to the sun-earth axis above the atmosphere can be derived from black body equations quite accurately, it is called the solar constant and has been measured at $1.36 kW/m^2$[2]. Integrating over earth's sun exposed surface, which is roughly a disk with a radius of 6371km, this value is often used to estimate the amount of energy received, and thus usable, from the sun. This amounts to $5,49.10^{24} J$ per year. 70% of this power is absorbed inside earth's global thermal system, and 30% is reflected into space due to the albedo. While not all of this energy is usable for energy production, it is still in the right order of magnitude of

what is achievable. This value is gigantic and represents approximately 10 000 times the total energy consumed by the world in 2018 [1].

This energy is the driving force behind earth's water and wind cycles, plant photosynthesis, which is the basis of most, if not all, life on earth, and the primary heating source of the atmosphere. As such hydroelectricity, wind turbines, and biomass are all renewable energy indirectly harvesting solar power. This power input shows slight variation of around 3% depending on time of the year, and may also vary due to the sun's magnetic activity cycle of the order of the percent over ten to eleven years cycles. Beyond this, this power source is expected to remain stable over human scale, with an expected increase in the next billion years to come.

- Earth also produces energy, in the form of heat, from the radioactive decay of the isotopes in the mantle and the crust, that were trapped during it's creation. It is also still releasing part of the primordial heat that was build up during earth's formation, which still has not been completely dissipated. This energy is the reason why the core of the earth is still partly liquid and the planet still has a tectonic and volcanic activity.

  The geothermal activity of earth appears to have been halved over the last 2 billion years but is very much a stable source of energy over human timescale[3]. This represents around $1,5.10^2121J$ reaching the ground every year in the form of heat, three times the annual world consumption. While being much smaller than what the sun offers, it is still more than human consumption, and a very stable constant source of heat. It is for example very much suited for house heating due to it's all year round, all day round availability.

- Finally, one can account for energy earth has stored over it's existence. This corresponds to resources that are non renewable due to their nature, for example isotopes required both for nuclear fusion and fission, or that are renewed on timescales much larger than human scale, like oil and coal. Oil, gas and coal are the major sources of energy currently used to meet energy needs, accounting for 85% of the consumption.

These resources have a high impact on the environment due to their effect on global warming and the potentially dangerous chemicals released during their combustion. These resources are also becoming scarcer and, assuming consumption to remain constant, are expected to last 50 years[1] for oil, gas and coal. The total consumption of these resources would however have dramatic consequences on the environment. The case of nuclear fission is much more speculative however.

With current technologies and accessible uranium sources, reserves are expected to last 150 years. But if advances are made in the development of so-called breeder reactors, which can generate more fissile fuel than they consume, these reserves could last for thousands to millions of years. Nuclear fusion also is a promising prospect for the future, potentially being able to provide energy for billions of years depending on the type of fusion achievable, but is still very far from mass power generation, and is an uncertain prospect.

In light of this, an energy transition appears to be inevitable in the years to come, and solar power is the most available and abundant source of energy on earth. The ability to tap into even just a fraction of it would most likely satisfy our needs for decades to come. Avoiding, or limiting at least, the disastrous events associated with global warming and environment pollution, makes this research all the more urgent. These are the motivations behind this thesis's work, and research on electricity generation from solar light.

1.2 Current solar cell technologies

With such a case for solar energy one can wonder why it is not a bigger portion of our production. We propose to look quickly at the historical development of solar cells before reviewing the current state of the technology. The photovoltaic effect is the creation of an electric current via exposure of a material to light, and was first reported by French physicist Edmond Becquerel in 1839 [4]. The first solar cell was created in 1883 by the hands of Charles Fritts, who achieved a

1% conversion efficiency with a selenium based solar cell [5]. In comparison this development happened nearly a hundred years after James Watt's steam engine.

So, solar energy had a hundred year delay at least compared to heat engines, and while the 19th century saw great advances in thermodynamics, solar cells development had to wait for the beginning of the 20th century, with Einstein's work on the photo-effect [6] and the birth of quantum mechanics to see any progress. Many of the first major technological developments started in the 1960's with the first space applications. The few other available power sources in space led to the development of solar cells, even at an elevated cost. The prices eventually dropped with the technological advancements and cells became available for earthly energy production.

Current technologies stems from this research and are traditionally divided in three categories. Best research-cell efficiency by type of solar cell can be found in figure 1.2. These categories are as follow.

- **First generation solar cells** are the first cell to appear historically and are made of crystalline silicon (c-Si). These represent 90% [7] of the solar cell market today. They appear in blue in figure 1.2 and generally are characterized by their high efficiencies, between 20 to 25%. These are made of solar-grade silicon, which requires a very high purity level, with less than one impurity per million atoms, meaning 99.9999% pure. While silicon is an abundant material of the crust, the purification process of c-Si is the major drawback of this technology, with high energy consumption, production toxicity and waste material being an issue.

- **Second generation solar cells** refer to thin-film solar cells, which tried to circumvent some of these problems. These technologies (in green in Fig 1.2) have a generally lower efficiency compared to c-Si, between 15 and 20%. They try to reduce the amount of active material in the cell. The film thickness varies from between a few nm to a few μm, when the active layer in c-Si is usually a few hundreds μm thick.

  As such they require less raw material, less energy to produce, and are easier to manufacture. Their thin size allows them to be made into flexible and/or transparent cells. Common materials include amorphous silicium, Cadmium

telluride, and copper indium gallium selenide. Despite these advantages, their market share did not took off and currently sits at around 5%. This is due primarily to drops in c-Si production prices and the complexity of having to deal with multiple technologies and multiple starting materials.

- **Third generation solar cells** are often referred to as emerging photovoltaics, and comprise a wide variety of different technologies. These include tandem solar cell, organic and dye sensitized solar cells, and the one of interest for this thesis, the perovskite solar cell. On figure 1.2, they are referenced under multijunction cells and emerging photovoltaic. Tandem solar cells are generally very efficient but very costly, due to to the multiple layers of high purity material required, while organic and dye sensitized solar cells are usually very cheap, but less efficient and stable.

  Perovskite cells sit in the middle of both world, with efficiency comparable to that of c-Si cells, while being made of inexpensive and easily manufactured material. They also show a record growing conversion efficiency that jumped from 3.8% in 2009 [8] to more than 25% currently.

While the photovoltaic technology started nearly a hundred year after the beginning of the combustion engine, it quite clearly is catching up. The photovoltaic market is booming with a solar levelized cost of electricity (LCOE) ranging between 0.04 to 0.11€$/kWh$, depending on system size[9]. This is comparable, and even sometime lower, than coal and natural gas production prices. Furthermore, the production prices of carbon based energy are expected to remain constant as the technology is already well developed, while the photovoltaic LCOE is expected to continue dropping, of approximately 10% per year, following the so called Swanson's law [10, 11].

Following this trend the global cumulative photovoltaic capacity has been growing nearly exponentially for the last 20 years[11], and solar energy is no longer a niche research subject for space application, but very much a major contestant as mankind near future primary energy source. Consequently, it is the subject of massive investments, research, and industrial developments. Let's now review the operating principles of solar cells, before introducing the specificities of perovskite cells.

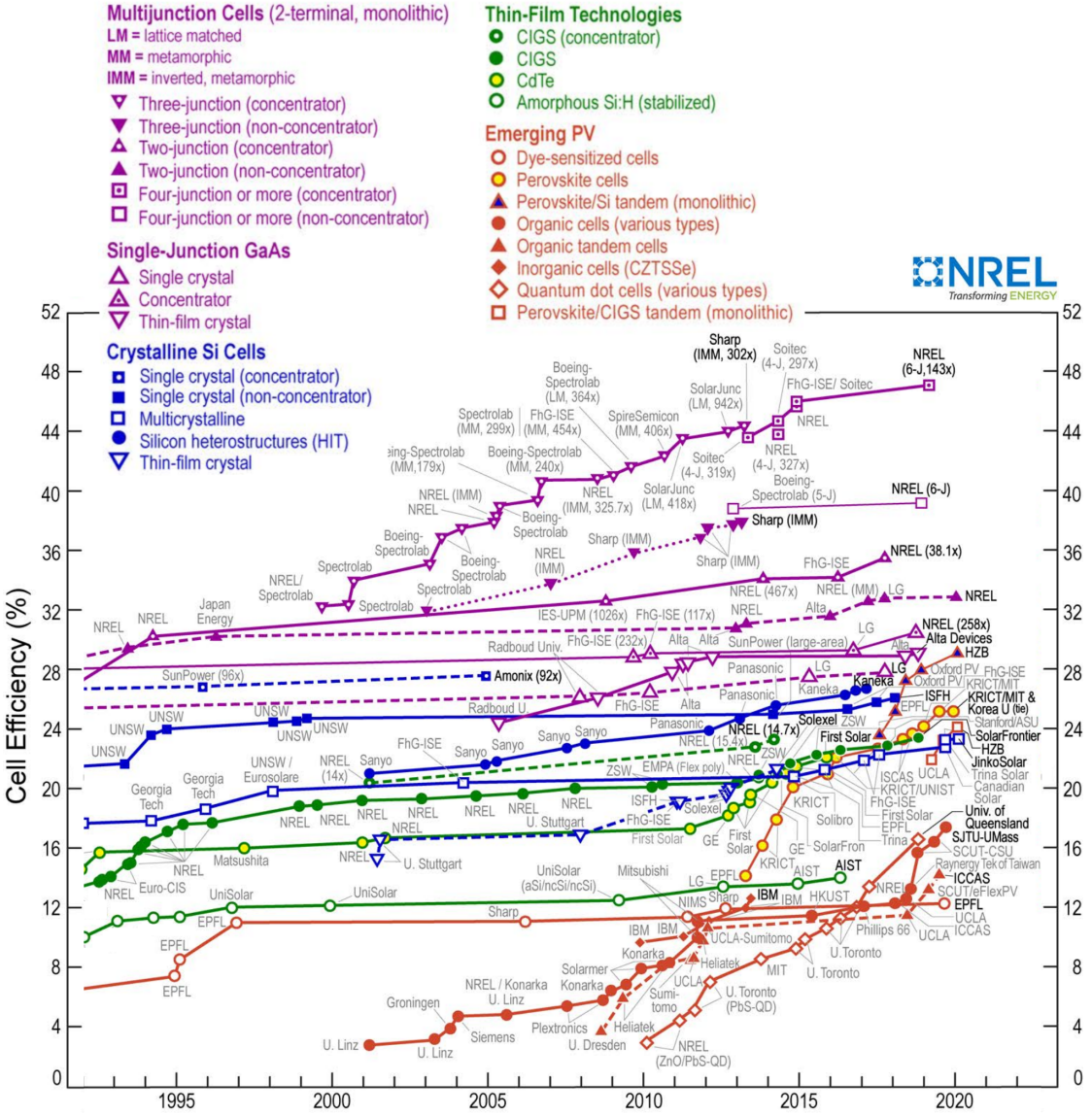

Figure 1.2: Best research-cell efficiencies for different technologies, as a function of time. Note the drastic improvement in efficiency for perovskite solar cell (orange), over a very short period of time. This plot is courtesy of the National Renewable Energy Laboratory, Golden, CO.

1.3 On the inner working of a solar cell

Light is made out of particles called photons, which are characterized by their wavelength and energy. The solar spectrum is a collection of photons with energies

ranging from infrared to ultraviolet mainly, with a maximum intensity in the green to yellow light, at wavelength of around $550nm$. In order to produce current, one needs to convert this radiation energy into electrical potential energy. This is done using semiconductor materials. A very important concept of solid state physics is that of band structure.

The band structure of a solid describes the energy levels that electrons can have or not inside the solid. These bands arise from the superposition of the atomic orbitals within the solid. The atomic orbitals give the number of electron and the available energy levels of the system, and Pauli's exclusion principle states that no two electrons can occupy the same level. As such one builds the band structure by filling the energy levels with the electrons of the system. The level of the last electron one puts in the band structure defines the Fermi level of the material, and much of it's properties depend on where this level lies, and what states are available close to it. Because we have filled all the lower energy states in the solid, electrons deep in the band structure have no empty states they can move to when we provide an excitation, with an electric field or light for example. The electrons near the Fermi level however have access to empty energy states close to them.

If the Fermi level is in the middle of a continuum of states, the electrons can move continuously between these states and conduct electricity and energy, this is the case of metals. It can also happen that there is an energy region void of states above the Fermi level. This void is a separation between two continuous bands, and is called the bandgap, or simply gap, of the semiconductor. The band below the gap is called the valence band and the one above, the conduction band. This implies that any energy excitation that is not at least as big as this gap can not interact with the electrons. A semiconductor will only conduct current if the exciting electrical field is greater than the gap, or if we have pumped electrons into the conduction band, or out of the valence band.

Figure 1.3 shows a representation of a band in a semiconductor and the associated processes. Note that when one excites an electron from the valence band to the conduction, one leaves an electron void in the valence band. This void behaves exactly like a positively charged electron would, and is treated as a quasi-particle, called a hole. As such when a photon is absorbed in a semiconductor, an electron jumps to the conduction band, and a hole appears in the valence band.

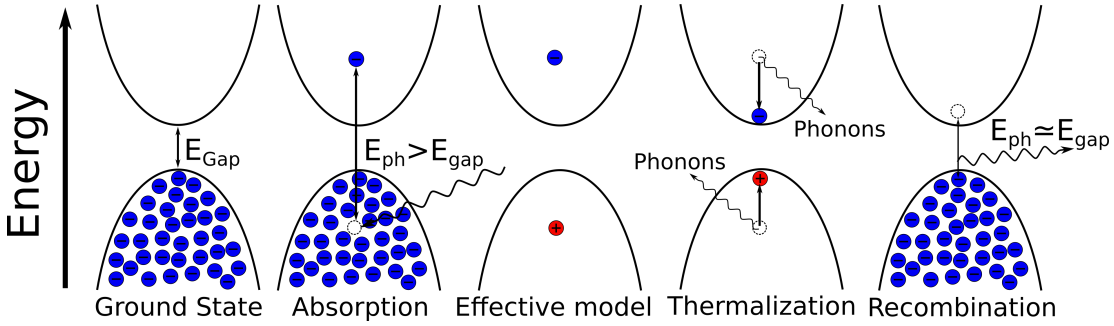

Figure 1.3: Different solar cell process as seen from a an energetic point of view. In the ground state, the valence band at the bottom contains the electrons (in blue), and the conduction band is empty. The forbidden region between the band is the semiconductor bandgap. Through absorption of a photon of greater energy than this gap, an electron can jump into the conduction band, and leaves a hole at it's original position. Because electrons are not discernible particles, we only need to follow the behaviour of the hole left behind by the electron, and not that of all the electrons in the valence band. The problem becomes a two particles problem, with one negative electron in the conduction band, and one hole in the valence band. These particles then cool down to the band edges, via emission of phonon, during the thermalization process, and can eventually undergo recombination.

This electron/hole pair is responsible for the transport of current and energy in the semiconductor. Once the pair is created, one of two things can happen. The electron and the hole can recombine via multiple complex processes, some via emission of phonon, others via emission of a photon, and the system returns to it's basis state, with no electrical current generated. This is generally not a desired event in solar cell, where electrical current is what is of interest, but is the basis of light-emitting diodes and optoelectronics. Current generation happens as follow:

- **Absorption:** First, light with sufficient energy is absorbed by electrons in the valence band, and an excited electron/hole pair is created.
- **Thermalization:** Depending on the energy of the absorbed photon, the hole and the electron can be more or less deep into the valence and conduction bands. Through interaction and collision with the atomic network, they will dissipate energy in the form of heat in the material via emission of phonons.

  This process stops once the pair reaches thermal equilibrium with the network, meaning the electron is close to the conduction band minimum and

the hole is close to the valence band maximum. This implies that excess photon energy is lost as heat in the material, the recoverable energy is always proportional to the bandgap. Therefore greater bandgap implies greater cell voltage, but lowers the number of absorbed photon. In the case of single material solar cell, there exists an ideal gap value to maximize the ratio between the voltage and the number of pair created, depending on the spectra of incident light. For sunlight, this value is of $1.34eV$, with a theoretical maximal efficiency of 34% [12].

The gap in silicon is of $1.1eV$, close to the optimal bandgap, which is one of the reasons for it's success. Gallium Arsenide is a material for high end solar cells with a bandgap of $1.44eV$, which gives even better efficiency, but is much more expensive. For reference, the most common perovskite for solar cells, $MaPbI_3$, has a bandgap of around $1.55eV$.

- **Diffusion:** Charge carriers now need to diffuse through the material to reach the electrodes from which they are injected into the actual electrical device the cell is powering. Without an external electrical field this process is a random walk via successive collision through the network, and without selective electrodes, no electrical current appears. Indeed if the electrodes are not selective, statistically as many holes as electrons reach each electrode, and because their charges are opposite, the total current is zero. To bypass these problems, one need to play with the energy levels within the material and/or of the electrodes.

  This is done via a process called doping in which impurities are inserted in selected regions of the semiconductor. These impurities bring either excess holes or excess electrons. A semiconductor is called p-doped if it has excess holes, or n-doped if it has excess electrons. When a p and a n type semiconductors are put in contact, their excessive charges attract each other and recombine at the interface. This creates a separation region, called space charge region between the elements, in which an electrochemical field appears, which can be used to separate electrons and holes. Energy levels through the cross section of a solar cell using a p-n junction can be seen in Figure 1.4, and is typical of how a silicon solar cell operates.

Another option, popular in organic and perovskite cells, where doping is uneasy, is to use selective contacts. Charge carrier are left to diffuse randomly in the material and are only selected at the electrodes. One electrode will only let electrons pass, and the other will only let holes pass. The efficiency of such cell then depends of how well charge carriers can diffuse, and if they can effectively reach their designated electrode before recombination.

- **Recombination:** Sooner or later, the electron and the hole will eventually recombine. This means charge carriers will return to their ground state, inside the valence band for the electron, and inside the conduction band for the hole. In solar cell we want this recombination to be slower than the charge extraction process, which allows their energy to be collected. If they recombine before being extracted, their energy difference is dissipated as light in the case of radiative recombination, or as thermal energy otherwise. Note that the generation of photon of very precise wavelength is possible via radiative recombination and is one of the subject of optoelectronics.

1.4 Perovskite solar cells

A perovskite solar cell refers to a cell that uses a perovskite structured compound as a light absorbing material. See figure 3.1 for a visual representation of the structure. The general formula for hybrid perovskites is ABX_3, where A and B are both cations and X is an anion. As an example, the most promising perovskite for solar cells has for formula $CH_3NH_3PbI_3$. The CH_3NH_3 is a methylammonium molecule, often shortened MA, and $CH_3NH_3PbI_3$ is also referred to as $MaPbI_3$, or MAPI. These perovskites possess very unique features that set them apart from other semiconductors. The materials used and the processing techniques are both low cost and adaptable. The absorbing perovskite layer can be obtained by wet chemistry techniques, such as spin coating and printing, or vapour deposition techniques, and the material can be adapted depending on the need.

The most common cation **B** used is lead, but the **X** anion can be any of the halogen ions, iodide, bromide or chloride, or a combination in different proportions

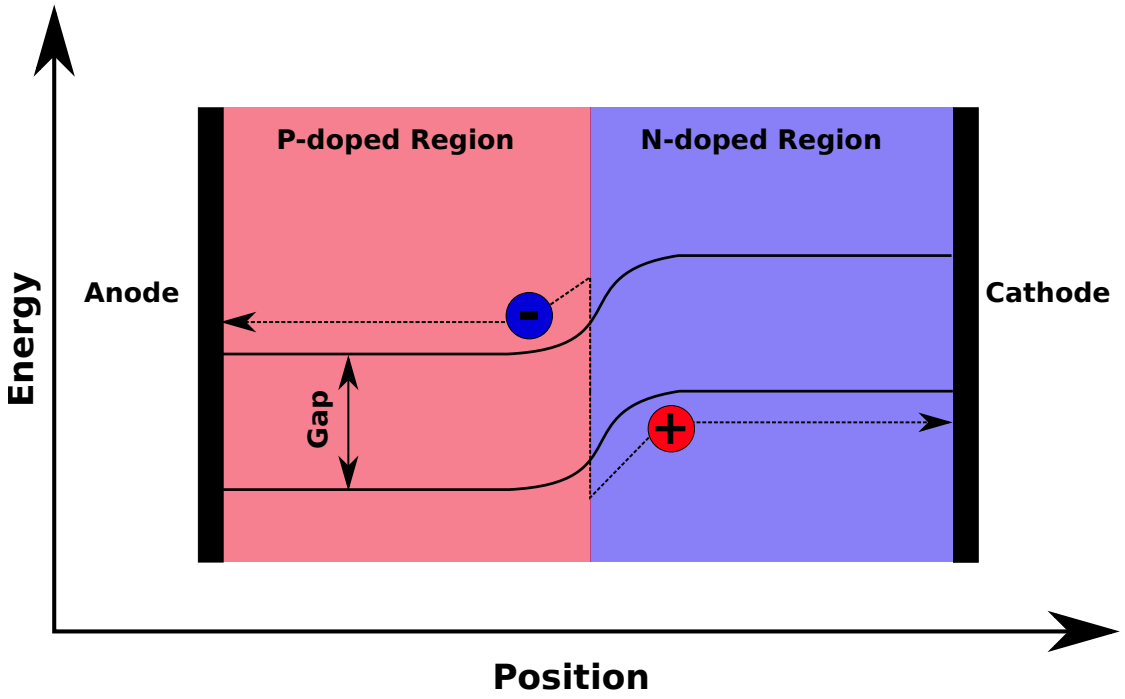

Figure 1.4: Visual representation of the potential in a P-N junction, and the path followed by the charge carriers after light absorption. This is typically the operating principle of a silicon solar cell.

of each of them. The **A** cation is often selected between the inorganic cesium, or the organic methylammonium and/or formamidinium (CH_5N_2) ions. All these choices in material and deposition techniques allow for very fine tuning and flexibility of the material's properties. For example, depending on halide content, the semiconductor gap can be tuned between 1.55eV, almost perfect for solar application, to 2.2eV, with a more robust material better suited for x-rays detection.

These perovskites do not come without drawbacks however. The fact that they can be solution processed indicates that the material is water soluble, and produced cells are very sensitive to degradation by moisture, oxidation, UV lights and the likes. Cells need to be shielded from the environment and extensive research is directed toward producing longer lasting materials. All the different alloying possibilities and growth techniques create a very wide range of materials with different qualities and defects, but because of their soft lattices, even the most defect-free samples appear strongly disordered at room temperature. The organic

molecule is weakly bounded to the inorganic lattice, and can freely rotate at room temperature [13, 14]. The inorganic network itself shows an-harmonic behaviour, and is often riddled with defects from the deposition process. The deposition technique generates multiple small crystals, of a few hundred nanometres, with different orientation that connect at grain boundaries, as well as various impurities from the processing solution.

Despite this, perovskites seem to be very resistant to all these defects, and exhibit very remarkable properties nonetheless. They show moderate to low charge carrier mobilities while boasting long charge carrier diffusion lengths and lifetimes. The physics behind these unusual phenomenons remains uncertain, and while both semi-classical and polaron based approaches have tried to tackle the problem, no completely satisfactory answer has been reached[15, 16, 17, 18, 19]. In this context we propose to study the electronic structure and the transport properties in these materials, and in particular MAPI, from a fundamental quantum point of view, with a special focus on the role of thermal disorder on charge carriers.

1.5 Thesis content

In this context, the goal of this thesis is to develop a model capable of describing the electronic structure and charge transport in these exotic perovskite materials, using MAPI as a reference, due to it's prevalence in solar cell applications.

In chapter 2, we first introduce the methodology required to numerically compute and resolve problems of electronic structure and charge carrier transport. Most of these methods have already successfully been used in studies concerning carbon nano-tubes, graphene and organic semiconductors. These include the development of functions and operators over polynomials based on the Hamiltonian, the recursion method and the chain model.

In chapter 3 we build the actual tight binding model describing MAPI. We start from the isolated atomic orbitals, and derive the coupling parameters that best describe the band structure compared to *ab-initio* simulations. From this perfect case we introduce disorder in the structure. We describe independently intrinsic disorder at room temperature on the atomic positions, atomic charge positions, and rotation of the MA molecules. We then discuss the behaviour and intensity

of these disorders.

In chapter 4, we build the Drude-Anderson model. This model is essential to us as we can use it to extract the physical parameters of transport from the quantum diffusion results. To do so, we start by presenting the standard Drude theory of transport, which has been extensively used to study perovskites. We highlight the limitations of this model, and present the phenomenon of Anderson localization, and why we believe it might play a role in MAPI. Then we present the fully quantum Kubo formalism for conductivity. From this formalism, we build the Drude-Anderson model of transport, which is a phenomenological extension of the Drude model, based on fully quantum concepts.

Then in chapter 5, using the tools developed in chapter 2, we extract results from the model of chapter 3, which we analyse using the Drude-Anderson model, from chapter 4. We present results about electronic structure, photoluminescence, and charge carrier mobility and terahertz conductivity. For all of these quantities, we find a good agreement with the experimental data. We are able to study the impact of disorder on these quantities, and to isolate their respective impact, on both electronic structure and conductivity. We discuss the possibility of polaron formation at room temperature, and find this scenario unlikely due to the strong scattering caused by longitudinal optical phonon modes. We instead propose a scenario for charge transport based on the so-called Thouless regime, in which charge carriers localize quickly, but are still allowed to diffuse thanks to the dynamic of the lattice. Finally we discuss in more details the fluctuating electrical potential (FEP) that exists in MAPI. This FEP is essential for transport properties and we discuss the condition for its existence in any material, and its consequences on electrical properties.

Finally, chapter 6 is a conclusion and retrospective on the model developed and the results obtained. It serves both to set the significance of this work in the context of perovskite for photovoltaic and charge transport in general, and opens on yet to be studied important phenomenon.

Bibliography

[1] "Bp statistical review of world energy 2019,"

[2] G. Kopp and J. L. Lean, "A new, lower value of total solar irradiance: Evidence and climate significance," *Geophysical Research Letters*, vol. 38, no. 1, 2011.

[3] R. Arevalo, W. F. McDonough, and M. Luong, "The k/u ratio of the silicate earth: Insights into mantle composition, structure and thermal evolution," *Earth and Planetary Science Letters*, vol. 278, no. 3, pp. 361 – 369, 2009.

[4] E. Becquerel, "Mémoire sur les effets électriques produits sous l'influence des rayons solaires," *Comptes rendus hebdomadaires des séances de l'Académie des sciences. Volume 9 : 561–567.*, 1839.

[5] J. Perlin, *Let It Shine: The 6000-Year Story of Solar Energy.* 2013.

[6] A. Einstein, "Über einen die erzeugung und verwandlung des lichtes betreffenden heuristischen gesichtspunkt," *Annalen der Physik*, vol. 322, no. 6, pp. 132–148, 1905.

[7] S. Philipps, "Photovoltaics report," *Fraunhofer ISE and Werner Warmuth, PSE Conferences and Consulting GmbH*, 2020.

[8] A. Kojima, K. Teshima, Y. Shirai, and T. Miyasaka, "Organometal halide perovskites as visible-light sensitizers for photovoltaic cells," *Journal of the American Chemical Society*, vol. 131, no. 17, pp. 6050–6051, 2009. PMID: 19366264.

[9] C. Kost and T. Schlegl, "Levelized cost of electricity- renewable energy technologies," 2018.

[10] R. M. Swanson, "A vision for crystalline silicon photovoltaics," *Progress in Photovoltaics: Research and Applications*, vol. 14, no. 5, pp. 443–453, 2006.

[11] J. D. Farmer and F. Lafond, "How predictable is technological progress?," *Research Policy*, vol. 45, no. 3, pp. 647 – 665, 2016.

[12] W. Shockley and H. J. Queisser, "Detailed balance limit of efficiency of p-n junction solar cells," *Journal of Applied Physics*, vol. 32, no. 3, pp. 510–519, 1961.

[13] S. Govinda, B. P. Kore, M. Bokdam, P. Mahale, A. Kumar, S. Pal, B. Bhattacharyya, J. Lahnsteiner, G. Kresse, C. Franchini, A. Pandey, and D. D. Sarma, "Behavior of methylammonium dipoles in $MAPbX_3$ (X = Br and I)," *The Journal of Physical Chemistry Letters*, vol. 8, no. 17, pp. 4113–4121, 2017. PMID: 28812901.

[14] N. P. Gallop, O. Selig, G. Giubertoni, H. J. Bakker, Y. L. A. Rezus, J. M. Frost, T. L. C. Jansen, R. Lovrincic, and A. A. Bakulin, "Rotational cation dynamics in metal halide perovskites: Effect on phonons and material properties," *The Journal of Physical Chemistry Letters*, vol. 9, no. 20, pp. 5987–5997, 2018.

[15] L. D. Whalley, J. M. Frost, Y.-K. Jung, and A. Walsh, "Perspective: Theory and simulation of hybrid halide perovskites," *The Journal of Chemical Physics*, vol. 146, no. 22, p. 220901, 2017.

[16] C.-J. Yu, "Advances in modelling and simulation of halide perovskites for solar cell applications," *Journal of Physics: Energy*, vol. 1, p. 022001, jan 2019.

[17] A. J. Neukirch, W. Nie, J.-C. Blancon, K. Appavoo, H. Tsai, M. Y. Sfeir, C. Katan, L. Pedesseau, J. Even, J. J. Crochet, G. Gupta, A. D. Mohite, and S. Tretiak, "Polaron stabilization by cooperative lattice distortion and

cation rotations in hybrid perovskite materials," *Nano Letters*, vol. 16, no. 6, pp. 3809–3816, 2016. PMID: 27224519.

[18] J. M. Frost, L. D. Whalley, and A. Walsh, "Slow cooling of hot polarons in halide perovskite solar cells," *ACS Energy Letters*, vol. 2, no. 12, pp. 2647–2652, 2017. PMID: 29250603.

[19] C. Wolf, H. Cho, Y.-H. Kim, and T.-W. Lee, "Polaronic charge carrier–lattice interactions in lead halide perovskites," *ChemSusChem*, vol. 10, no. 19, pp. 3705–3711, 2017.

Chapter 2

Numerical methods

Contents

2.1 Introduction

In this chapter are presented the mathematical formalism and tools useful in our study of electronic structure and quantum transport.

We begin with an introduction of a few of the operators we need in this thesis as well as how they are approximated, via a polynomial expansion generated from the Hamiltonian.

We then present the recursion method and the chain model in section 2.3, as these are our bread and butter and have been continuously used through all the

thesis. Sections 2.4 to 2.5 relate to various method of extracting information from the chain model.

Then we introduce the time evolution operator and the mean quadratic spread operator, which are essential to compute charge carrier diffusion; which then gives us the mobility and the low frequency conductivity of the material. We show how the time evolution operator can be approximated via a polynomial expansion, and how it allows us to compute the mean quadratic spread operator. Finally, we present the algorithm for quantum diffusion, showing how all these different tools are used together.

2.2 Polynomial expansion of functions and operators

Let's consider a positive density $n(E)$ so that $\int dEn(E) = 1$ and define, in the space of the complex functions of E, the Hermitian product:

$$\langle f|g\rangle = \int n(E)f^*(E)g(E)dE, \tag{2.1}$$

which is the projection of g over f. There exists a basis of orthogonal polynomials, $P_n(E)$, so that

$$\langle P_n|P_m\rangle = \delta_{n,m}, \tag{2.2}$$

where P_n and P_m are respectively of degree n and m, and are real. It is known from the theory of orthogonal polynomials that they follow the three term recurrence relation

$$EP_n = a_nP_n + b_nP_{n+1} + b_{n-1}P_{n-1}, \tag{2.3}$$

where $b_{-1} = 0$, and ,for $n \geq 0$, a_n and b_n are real coefficients that depend on n(E). From there, any function can be evaluated in the $\{P_n\}$ basis, as the sum of its projection over each polynomial :

$$f(E) = \sum_{n=0}^{\infty} c_n(f) P_n(E), \tag{2.4}$$

with a convergence in average and

$$c_n(f) = \langle P_n | f \rangle = \int n(E) P_n(E) f(E) dE. \tag{2.5}$$

Functions of a given operator can also be evaluated in this way. There are three operators that depend on the Hamiltonian $\hat{H}$, and are particularly important to this work. They are:

$$f(x, \hat{H}) = \delta(E - \hat{H}), \text{ with } x = E, \tag{2.6}$$

$$f(x, \hat{H}) = \frac{1}{z - \hat{H}}, \text{ with } x = z, \tag{2.7}$$

$$f(x, \hat{H}) = \hat{U}(t, \hat{H}) = e^{-i\hat{H}t/\hbar}, \text{ with } x = \hbar/t. \tag{2.8}$$

The first two are related to the density of states $n_\alpha(E)$ and the Green's function $G_\alpha(z)$ on any state $|\alpha\rangle$

$$n_\alpha(E) = \langle \alpha | \, \delta(E - \hat{H}) \, | \alpha \rangle \,, \tag{2.9}$$

and

$$G_\alpha(z) = \langle \alpha | \, \frac{1}{z - \hat{H}} \, | \alpha \rangle \,. \tag{2.10}$$

The last operator is the time evolution operator $\hat{U}(t)$ which allows us to compute the evolution of a wave packet $|\phi(t)\rangle$ over time and is defined as

$$\hat{U}(t, \hat{H}) = e^{-i\hat{H}t/\hbar}, \tag{2.11}$$

with

$$|\phi(t)\rangle = \hat{U}(t, \hat{H}) \, |\phi(0)\rangle \,. \tag{2.12}$$

Furthermore it has been shown that [1, 2]

$$\delta(E - \hat{H}) = N(E) \sum_n P_n(E) P_n(\hat{H}), \tag{2.13}$$

provided that the spectrum of $N(E)$ contains the spectrum of $\hat{H}$. From this, one can construct the spectral decomposition of any function $f(x, \hat{H})$:

$$f(x, \hat{H}) = \int f(E)\delta(E - H)dE = \sum_n c_n(x) P_n(\hat{H}), \tag{2.14}$$

where

$$c_n(x) = \int N(E) P_n(E) f(X, E) dE \tag{2.15}$$

depends on f, but not on the operator $\hat{H}$, or on the space where it acts. As such this operator expansion is actually the cornerstone that allows us to solve our problems in terms of energy, as in equation 2.17.

Most of the time we wish to evaluate functions of operators applied to a specific state and we usually work in the Krylov subspace [3]. The Krylov subspace of order N is defined as the subspace generated by the N first images of a vector b under the first N powers of a matrix A, with $A^0 = Id$. In our case the original vector b is the original phase state of our system, which we call $|\phi_0\rangle$, and the matrix is the Hamiltonian $\hat{H}$. The subspace we span is then

$$\mathcal{K}_N(\hat{H}, |\phi_0\rangle) = span\left\{ |\phi_0\rangle, \hat{H}|\phi_0\rangle, ..., \hat{H}^{N-1}|\phi_0\rangle \right\}. \tag{2.16}$$

Note that the Lanczos method [4] which is closely related to the formalism presented here also relies on the Krylov space. Finally, we note that for $G_\alpha(z)$, there is an alternative development based on the continuous fraction expansion presented below in section 2.4, and that the time evolution operator is developed over the rescaled Chebyshev polynomials, as detailed in section 2.6.

2.3 Chain model and recursion method

A big part of what we will need to do is computing the density of states and operators expectation values, especially for the position operator $\hat{X}$ when we look at diffusion. The expectation value of any operator A overs the states of energy E is:

$$\langle \hat{A} \rangle_E = \frac{Tr[\delta(E - \hat{H})\hat{A}]}{Tr[\delta(E - \hat{H})]}, \tag{2.17}$$

with the total density of states being

$$n(E) = Tr[\delta(E - \hat{H})], \tag{2.18}$$

and

$$Tr(A) = \sum_j \langle j| A |j\rangle . \tag{2.19}$$

Having access to the expectation value as a function of energy is important to account for thermal occupation of the states at the considered temperatures. Starting from the eigenstates $|j\rangle$ of our system, which is computationally very expensive as the system size grows, would be technically impossible with the system sizes we consider. To circumvent this, we present the chain model and the recursion method [5, 6], which are the most used tools in this thesis. It is an exact representation of any time independent Hamiltonian, which is expressed in the minimal necessary Hilbert space, which is the Krylov space. It is constructed by generating an orthogonal basis in which the Hamiltonian is tridiagonal. In order to do so one can use a recursion method, based on the Gram-Schmitt process.

When applying the Hamiltonian to the selected initial state $|\phi_0\rangle$, one gets a new state, which can be split into two components, one parallel to it $a_0 |\phi_0\rangle$, and one perpendicular to it, which is $b_0 |\phi_1\rangle$.

$$\hat{H} |\phi_0\rangle = a_0 |\phi_0\rangle + b_0 |\phi_1\rangle . \tag{2.20}$$

As $|\phi_0\rangle$ and $|\phi_1\rangle$ are orthonormal, the following relations apply: $\langle \phi_0 | \phi_0 \rangle = 1$,

$\langle\phi_1|\phi_0\rangle = 0$, and $\langle\phi_1|\phi_1\rangle = 1$. So, one is able to compute the parameters $a_0 = \langle\phi_0|\,\hat{H}\,|\phi_0\rangle$ and $b_0^2 = |(\hat{H} - a_0)\,|\phi_0\rangle\,|^2$. By choosing $b_0 > 0$, we compute $|\phi_1\rangle$ from

$$b_0\,|\phi_1\rangle = \hat{H}\,|\phi_0\rangle - a_0\,|\phi_0\rangle\,. \tag{2.21}$$

By applying the Hamiltonian to the newly constructed state $|\phi_1\rangle$ one constructs an other state which can also be projected on the already constructed vectors and has an additional perpendicular component. Thus we get the following recursion relation:

$$\hat{H}\,|\phi_1\rangle = \tilde{b}_0\,|\phi_0\rangle + b_1\,|\phi_2\rangle + a_1\,|\phi_1\rangle\,, \tag{2.22}$$

where $|\phi_2\rangle$ is perpendicular to both $|\phi_0\rangle$ and $|\phi_1\rangle$. We have:

$$a_1 = \langle\phi_1|\hat{H}|\phi_1\rangle\,, \tag{2.23}$$

$$\tilde{b}_0 = \langle\phi_0|\hat{H}|\phi_1\rangle = \langle\phi_1|\hat{H}|\phi_0\rangle = b_0, \tag{2.24}$$

because the Hamiltonian is Hermitian. Then

$$b_1\,|\phi_2\rangle = \hat{H}\,|\phi_1\rangle - a_1\,|\phi_1\rangle - b_0\,|\phi_0\rangle\,. \tag{2.25}$$

b_1 is chosen positive and $\langle\phi_2|\phi_2\rangle = 1$. Quite generally $\hat{H}\,|\phi_n\rangle$ decomposes on all previous $|\phi_m\rangle$ with $m \leq n$ and on $|\phi_{n+1}\rangle$ which is orthogonal to them. But because the Hamiltonian is Hermitian, it only couples neighbouring states so that

$$\langle\phi_{n+p}|\hat{H}|\phi_n\rangle = \langle\phi_n|\hat{H}|\phi_{n+p}\rangle^* = 0 \text{ if } |p| \geq 2. \tag{2.26}$$

Therefore we can write the general relation for any $n > 0$, the recurrence relation:

$$b_n\,|\phi_{n+1}\rangle = \hat{H}\,|\phi_n\rangle - a_n\,|\phi_n\rangle - b_{n-1}\,|\phi_{n-1}\rangle\,. \tag{2.27}$$

So we are able to build an orthonormal basis to express our Hamiltonian, step by step, via recursion. In this basis every state $|\phi_n\rangle$ is coupled to itself through the parameter a_n and to $|\phi_{n-1}\rangle$ and $|\phi_{n+1}\rangle$ by the parameters b_{n-1} and b_n, with

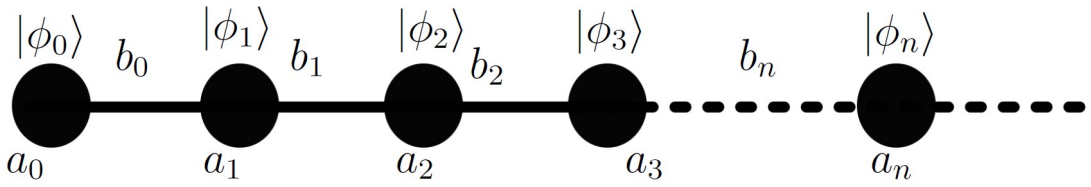

Figure 2.1: Visual representation of the tridiagonal Hamiltonian of any system after using the recursion method. The states are represented by the wave function $|\phi_n\rangle$ which are linear combination of orbitals of our system. The coefficients a_n represent the onsite energy of every wave function and the coefficients b_n the coupling between them.

the condition that the state $|\phi_0\rangle$ is only coupled to himself and $|\phi_1\rangle$. In this basis the Hamiltonian is tridiagonal :

$$\hat{H} = \begin{bmatrix} a_0 & b_0 & 0 & \dots & \\ b_0 & a_1 & b_1 & 0 & \\ \ddots & \ddots & \ddots & \ddots & \\ & 0 & b_{n-2} & a_{n-1} & b_{n-1} \\ & & 0 & b_{n-1} & a_n \end{bmatrix}.$$

This Hamiltonian is most easily understood as a chain, which is a visual representation of the basis, as in figure 2.1.

Now, this tridiagonal Hamiltonian is an exact interpretation of the original Hamiltonian, but is much smaller and simpler than the full Hamiltonian. Physically, the chain is the minimal Hilbert space in which a state initially at $|\phi(t=0)\rangle = |\phi_0\rangle$ develops in time. We usually only have to compute a few thousand $|\phi_n\rangle$ compared to the millions of orbitals we had before, to get enough eigenstates.

From the recurrence relation we see that

$$|\phi_n\rangle = P_n(\hat{H})\,|\phi_0\rangle\,, \tag{2.28}$$

where $P_n(\hat{H})$ is a real polynomial of $\hat{H}$ of degree n, which coefficients depend on a_n and b_n. They verify the following relations:

$$\hat{H}P_n = a_n P_n + b_n P_{n+1} + b_{n-1} P_{n-1}, \tag{2.29}$$

and

$$\langle \phi_n | \phi_m \rangle = \langle \phi_0 | P_n(\hat{H}) P_m(\hat{H}) | \phi_0 \rangle = \delta_{n,m}. \tag{2.30}$$

What we seek to determine is the density of states on the initial state $|\phi_0\rangle$, defined as:

$$n_0(E) = \langle \phi_0 | \delta(E - \hat{H}) | \phi_0 \rangle \,. \tag{2.31}$$

To do so, we reuse equation 2.13, to develop equation 2.30 as a function of E:

$$\begin{aligned} \langle \phi_n | \phi_m \rangle = \int \langle \phi_0 | P_n(E) P_m(E) \delta(E - H) | \phi_0 \rangle \, dE \\ \int n_0(E) P_n(E) P_m(E) dE = \delta_{n,m}, \end{aligned} \tag{2.32}$$

which is the link between the computed polynomials and the density of states of the system. Therefore $P_n(E)$ are the orthogonal polynomials associated to the weight $n_0(E)$.

Numerically, the recursion proceeds as follows. Let us consider a state $|\phi_n\rangle$ from our chain. We build the state $|\phi_{n+1}\rangle = \hat{H} \, |\phi_n\rangle$, which is not yet orthogonal to $|\phi_n\rangle$. Then we compute a_n as

$$a_n = \langle \phi_{n+1} | \, | \phi(n) \rangle \,. \tag{2.33}$$

The only information we need from the previous steps of recursion is that of state $|\phi_{n-1}\rangle$ and b_{n-1}, and so we have kept them in memory from before. We orthogonalize the states $|\phi_{n+1}\rangle$ doing

$$|\phi_{n+1}\rangle = |\phi_{n+1}\rangle - a_n \, |\phi(n)\rangle - b_{n-1} \, |\phi_{n-1}\rangle \,, \tag{2.34}$$

compute parameter b_n,

$$b_n = \langle \phi_{n+1} | \, | \phi_{n+1} \rangle \,, \tag{2.35}$$

and normalize the state

$$|\phi_{n+1}\rangle = |\phi_{n+1}\rangle / b_n. \tag{2.36}$$

We have computed the parameters a_n and b_n, and build the state needed to further the recursion. We can see that we only need to keep in memory three states at any time, $|\phi_{n-1}\rangle$, $|\phi_n\rangle$, and $|\phi_{n+1}\rangle$, which means that this method has a fixed memory cost, and scales linearly with the number of atomic orbitals and the number of recursion steps, making it ideal to study large Hamiltonians.

2.4 Green's functions and the continuous fraction

One requirement of our work is the determination of the local density of states. We can make use of the Green's operator $G(z) = (z - H)^{-1}$, also called the resolvent. The Green's function which will be of interest to us is the Green's function on the original phase state, ϕ_0 and defined as:

$$G_0(z) = \langle \phi_0 | \frac{1}{z - \hat{H}} | \phi_0 \rangle \,, \tag{2.37}$$

where z is defined as E + $i\epsilon$. E is the energy at which we consider our system and ϵ is a small positive real number that tends to zero. Green's function are related to the local density of states according to the relation:

$$n_{loc}(E) = \langle \phi_0 | \delta(E - \hat{H}) | \phi_0 \rangle = -\frac{1}{\pi} Im(G_0(z)) \tag{2.38}$$

The quantity $(z - \hat{H})$ can be expressed as:

$$(z - \hat{H}) = \begin{bmatrix} z - a_0 & b_0 & 0 & \dots & \\ b_0 & z - a_1 & b_1 & 0 & \\ \ddots & \ddots & \ddots & \ddots & \\ & 0 & b_{n-2} & z - a_{n-1} & b_{n-1} \\ & & 0 & b_{n-1} & z - a_n \end{bmatrix}.$$

And it can be shown that, by using Cramer's rule:

$$G_0(z) = \frac{1}{z - a_0 - b_0^2 \tilde{G}_1(z)}, \tag{2.39}$$

where $\tilde{G}_1(z)$ represent $G_0(z)$ but for a chain where the first site has been cut off. By repeating the above, we are able to obtain and give the general relation:

$$\tilde{G}_n(z) = \frac{1}{z - a_n - b_n^2 \tilde{G}_{n+1}(z)}, \tag{2.40}$$

where $\tilde{G}_n(z)$ represent $G_0(z)$ but for a chain where the first n sites have been cut off, and we are able to obtain the continuous fraction expansion of $G_0(z)$:

$$G_0(z) = \cfrac{1}{z - a_0 - \cfrac{b_0^2}{z - a_1 - \cfrac{b_1^2}{\cdots}}}. \tag{2.41}$$

This formulation of the Green's function can easily be implemented numerically and, in combination with the recursion method, can be used to derive the density of states of any system.

The question left pending now is where to stop and how to end the continuous fraction, as our system can theoretically be infinite and the chain semi-infinite. The simplest way is to simply cut-off the fraction by setting the first unknown parameter to zero, which writes:

$$G_0(z) = \cfrac{1}{z - a_0 - \cfrac{b_0^2}{....z - a_{n-1} - \cfrac{b_{n-1}^2}{z - a_n - \cfrac{b_n^2}{z}}}}. \tag{2.42}$$

The advantage of this termination is it's simplicity and that the error it causes decreases as the number of computed coefficients increases.

An alternative way of terminating the continuous fraction is via a square-root termination. It is possible to do so in cases where the coefficient a_n and b_n eventually converge to a value. If we assume that after some number of iteration

steps the coefficients have converged to their asymptotic limits a_{rec} and b_{rec} then we can write the last Green's function as:

$$\tilde{G}_n(z) = \frac{1}{z - a_{rec} - \Sigma(z)}, \tag{2.43}$$

where Σ is the self-energy and, as every step of the continuous fraction is now the same, is self defined as:

$$\Sigma(z) = \frac{b_{rec}^2}{z - a_{rec} - \Sigma(z)}. \tag{2.44}$$

This self energy can be seen as the interaction of the particles or orbitals considered with the rest the environment. This expression is a quadratic expression and can easily be solved to give:

$$\Sigma(z) = \frac{z - a_{rec} \pm \sqrt{(z - a_{rec})^2 - 4b_{rec}^2}}{2}, \tag{2.45}$$

which leaves us with three solutions:

$$\text{if } |z - a_{rec}| < 2b_{rec} \qquad \Sigma(z)_C = \frac{z - a_{rec} - i\sqrt{4b_{rec}^2 - (z - a_{rec})^2}}{2}, \tag{2.46}$$

and

$$\text{if } |z - a_{rec}| > 2b_{rec} \qquad \Sigma(z)_R = \frac{z - a_{rec} \pm \sqrt{(z - a_{rec})^2 - 4b_{rec}^2}}{2}. \tag{2.47}$$

As the density of states is proportional to the imaginary part of the Green's function, we can determine that the energy continuum for such a system is between $-2b_{rec} < E - a_{rec} < 2b_{rec}$. For a semi-infinite chain with a constant hopping integral set to 1, which we will be using later, the energy continuum is therefore between $-2 + a_{rec}$ and $2 + a_{rec}$

2.5 Diagonalization and Gaussian widening

While the continuous fraction expansion is a very powerful tool, cases arise where the coefficients do not converge, and a proper termination of the continuous fraction becomes impossible. Furthermore, using Green's functions to compute the density of states implies using a finite ϵ, which is equivalent to a widening of the eigenvalues by a Lorentz distribution. This distribution decreases proportionally to $1/x^2$, which implies that the computed density of states sometimes decreases slowly, even far from the eigenvalues.

These two phenomenons become especially problematic in semiconductors around the bandgap, which becomes ill-defined and difficult to tackle. In this situation it becomes necessary to diagonalize the tridiagonal Hamiltonian, obtained via recursion. While this method is much more time consuming than the continuous fraction, it allows widening of the eigenstates via a Gaussian, that have much smaller tails than a Lorentzian. This gives finer details about the distribution of the eigenvalues, thanks to the obtained energy resolution. Here, the density of states is computed as

$$n(E) \simeq \frac{1}{\sqrt{2\pi}\sigma} \sum_{n=1}^{N} w_n(0) e^{\frac{(E-e_n)^2}{2\sigma^2}} \tag{2.48}$$

where N is the number of eigenstates, equal to the number of recursion steps, e_n is the eigenstate energy, and w_n is the projection of the eigenvector $|n\rangle$ on the original state, $|\phi_0\rangle$, $w_n(0) = |\langle n|\phi_0\rangle|^2$.

Having access to the eigenstates also allows us to generate specific phases states of a chosen energy. This is particularly useful for photoluminescence computation (see chapter 5) where we want to compute the probability of transition between states near the edges of the valence and conduction bands specifically. The energy filtering is done after the first diagonalization, which gives us the eigenstates, and also uses the Krylov space as

$$|\phi(e_n)\rangle = \sum_{i=0}^{N} w_n(i) |\phi_i\rangle , \tag{2.49}$$

where $|\phi(e_n)\rangle$ represents a phase state centred around energy e_n, $w_n(i) = \langle n|\phi_i\rangle$,

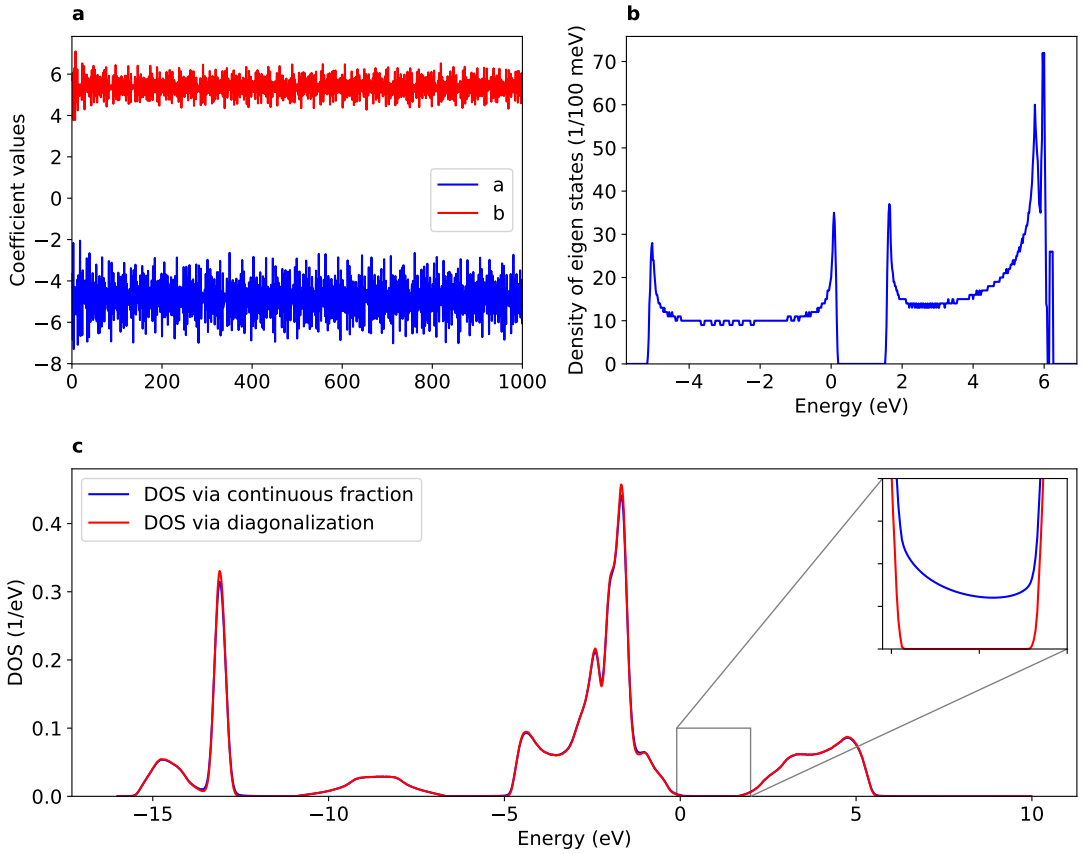

Figure 2.2: a: First thousand a and b coefficients for the density of states. The coefficients are oscillating with no distinctive pattern over an average value, making it impossible to find a satisfying continuous fraction termination. **b:** Density of eigenstates around the band edges. The average spacing between states is of 10meV, diminishing when approaching the band edges. Our resolution is therefore between 5 to 15 meV.**c:** Entire density of states computed either via continuous fraction (blue) or via diagonalization (red). The inset is a zoom on MAPI's bandgap. While the two density are extremely similar, the density of states never reaches zero in the bandgap when using the continuous fraction method, making it impossible to compute thermal mobilities and occupations.

and $|\phi_i\rangle$ are the basis states of the recursion chain. Because eigenstates of the tridiagonal Hamiltonian are not exactly eigenstates of the real Hamiltonian, the states generated this way have a non zero width, which is typically of the order of the distance between two eigenstates, around 5-15 meV. This is the limit of our

resolution for results on photoluminescence.

2.6 The time evolution operator

In order to compute the diffusion of a wave packet over time, we need to solve the time dependent Schrödinger equation, which means computing the action on the initial state of the time evolution operator:

$$\hat{U}(T) = exp(-\frac{i\hat{H}T}{\hbar}). \tag{2.50}$$

Numerous numerical method for the resolution of this equation exist, ranging from exact diagonalization method to Runge-Kutta approximation. However most of them are limited by the size of the Hamiltonian they can solve or the computing time they require, and our study of perovksite as plastic materials forces us to use large systems to properly estimate the impact of disorder. As such we must restrain ourselves to the only solutions still reasonable for us, which are the methods based on successive iteration of the Hamiltonian on our systems and the use of the Krylov space. These methods consist in using $\hat{\mathrm{H}}$ based polynomials, and thus the time evolution operator is approximated, and as shown in section 2.2, we can write

$$\hat{U}(t) \simeq \sum_{n=0}^{N} c_n(t) P_n(\hat{H}). \tag{2.51}$$

This equation converges more or less rapidly depending on the choice of the density n(E) associated to the family of $\{P_n\}$ in equation 2.1 when $N \to \infty$. We recall that in order to compute $c_n(t)$ we only need the recursion coefficient a_n and b_n associated to the chosen density, and the function $f(E) = e^{-iEt/\hbar}$ associated to the operator $\hat{U}(t) = e^{-i\hat{H}t/\hbar}$.

The Chebyshev polynomials of the first kind will be our polynomials of choice for the development of the time evolution operator. They are associated to the density $n(E) = 1/\pi\sqrt{1-E^2}$, defined on the interval $[-1, 1]$. By substituting variables, we adapt these polynomials to the interval $[a_C - 2b_C, a_C + 2b_C]$, containing all the spectrum of the Hamiltonian. The density considered is then:

$$n(E) = \frac{1}{2\pi b_C \sqrt{1-(E-a_C)^2/4b_C^2}}. \tag{2.52}$$

The semi infinite chain associated is the one where all onsite energies $a_n = a_C$, $b_0 = \sqrt{2}b_C$ and $b_n = b_C$ for all other n. These polynomials are used a lot to approximate functions on a given interval, they have the interesting property of converging in an almost uniform fashion over the complete interval $[a_C - 2b_C, a_C + 2b_C]$.

The coefficients $c_n(t)$ can be expressed from the Bessel functions [7] but we compute them as follows. It is useful for us to consider a fictitious tridiagonal Hamiltonian $\hat{H}_{\hat{U}(t)}$ associated to the Chebyshev polynomials. It is a semi infinite chain with onsite energies a_C and hoping parameters $b_0 = \sqrt{2}b_C$ and $b_n = b_C$ for $n \geq 1$. This chain is similar to the one used in the recursion method. We can compute the coefficients $c_n(t)$ with a sufficient precision by cutting this chain after a few hundreds to a few thousands sites, which gives us an Hamiltonian of reasonable size to diagonalize. Note that for this fictive chain, associated to the Chebyshev polynomials, it is also possible to diagonalize it analytically. Applying equation 2.51 on this chain we get

$$|\phi_0(t)\rangle = \sum_{n=0}^{N} c_n(t)\,|\phi_n\rangle \tag{2.53}$$

These coefficients can thus be expressed by summation over the $N+1$ eigenstates $|E_i\rangle$ of the chain as

$$c_n(t) = \langle n|\phi_0(t)\rangle \tag{2.54}$$

and, by spectral decomposition on the eigenstates of the chain

$$c_n(t) \simeq \sum_{i=0}^{N} \langle n|E_i\rangle\, e^{-iE_it/\hbar}\, \langle E_i|0\rangle\,. \tag{2.55}$$

2.7 Algorithm for quantum diffusion

Computation of electronic transport proceeds as follow. First we generate the Hamiltonian of our system, computing orbital interaction and disorder. More explanation on how the Hamiltonian of MAPI is built can be found in chapter 3. Then we generate the starting state $|\phi_0\rangle$ of our system. In order to have an even distribution of states over the whole spectra we build it as a random phase state over all atomic orbitals,

$$|\phi_0\rangle = \frac{1}{\sqrt{N}} \sum_{n=0}^{N} e^{2i\pi r_n} |\mu_n\rangle \,, \tag{2.56}$$

where r_n is a random number and N is the number of orbitals in the system. From this we can compute the tridiagonal Hamiltonian via recursion. We build the states $|\phi_1\rangle$ as:

$$|\phi_1\rangle = (\hat{H} |\phi_0\rangle - a_n |\phi_0\rangle)/b_1 \tag{2.57}$$

and all subsequent states using equation 2.27:

$$b_n |\phi_{n+1}\rangle = \hat{H} |\phi_n\rangle - a_n |\phi_n\rangle - b_{n-1} |\phi_{n-1}\rangle \,. \tag{2.58}$$

To do so we only keep at each instant in memory only 3 states, $|\phi_{n-1}\rangle$, $|\phi_n\rangle$, and $|\phi_{n+1}\rangle$, and store the a_n and b_n coefficients as we go.

When using samples of 32 million orbitals, this only represent a memory usage of a few Go. The number of eigenstates one has access to is equal to the number of recursion steps taken, and we found that a few thousand steps, typically 3000 in our case, gives us an energy resolution of 5 to $15meV$.

From this we can compute the density of states as a function of energy, using either Green's functions and the continuous fraction method, or via diagonalization and Gaussian widening. Now we have the DOS and the spectrum interval, and we can compute the Chebyshev polynomials. We define a_C and b_C so that the interval $[a_C - 2b_C, a_C + 2b_C]$ contains the whole spectra and diagonalize the chain associated with these coefficients. We then compute the coefficients $c_n(t)$ after equation 2.55 for every time we wish to compute, and we are now ready to compute the evolution

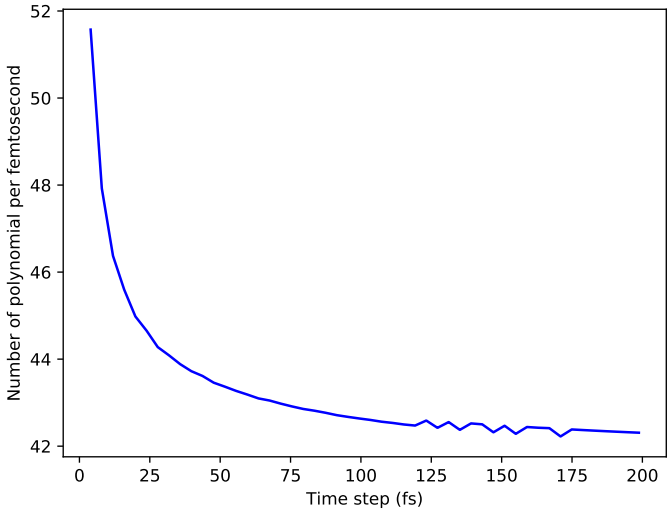

Figure 2.3: Number N of Chebyshev polynomials divided by the time step $T_{p+1} - T_p$ as a function of the time step considered in femtoseconds. This graphs shows that it is computationally more efficient to approximate the time evolution operator with large time steps rather than doing small time increments. In particular for time steps smaller than a femtosecond, this number increases quickly and tends to diverge. This is why this method is more efficient than Runge-Kutta methods [8], which require small time steps.

of $|\phi_0\rangle$ over time.

In parallel to this evolution we want to compute the mean square spreading of the wave function over the lattice, defined as :

$$X^2(E,t) = \left\langle (\hat{X}(t) - \hat{X}(0))^2 \right\rangle_E \tag{2.59}$$

where $\hat{X}$ is the position operator and $\hat{X}(t) = U(t)^* \hat{X}(0) U(t)$. This develops into the following expression:

$$\begin{aligned} X^2(E,t) &= \langle\phi| \left(\hat{X}(t) - \hat{X}(0)\right)^* \delta(E - \hat{H}) (\hat{X}(0) - \hat{X}(t)) |\phi\rangle \\ &= \langle\phi| \left([\hat{X}(t), \hat{U}(t)]^* \delta(E - \hat{H}) [\hat{X}(t), \hat{U}(t)] |\phi\rangle \right. . \end{aligned} \tag{2.60}$$

For simplification we define two wave functions $|\phi(t)\rangle$ and $|\psi(t)\rangle$:

$$|\psi(t)\rangle = [X, U(t)]\,|\phi_0\rangle\,, \tag{2.61}$$

and

$$|\phi(t)\rangle = U(t)\,|\phi_0\rangle\,, \tag{2.62}$$

where $|\phi_0\rangle$ is the original random phase state of the system. These two wave vectors must be computed together as their are dependant on one another, as shown below, and they provide the information we need.

This notation simplifies equation 2.60 in :

$$X^2(E,t) = \langle\psi(t)|\,\delta(E-\hat{H})\,|\psi(t)\rangle\,, \tag{2.63}$$

which is equivalent to computing a density of states on state $|\psi(t)\rangle$, and is done via recursion. Note that if we simply write $[X, U(t)]\,|\phi_0\rangle = (Xe^{-iHt/\hbar} - e^{-iHt/\hbar}X\,|\phi_0\rangle$, this expression is not compatible with periodic boundary conditions, due to the discontinuity in position X when crossing the boundaries.

We circumvent this difficulty by working only with commutators $[X, f(\hat{H})]$ as shown below. Using the fact that $[A, BC] = [A, B]C + B[A, C]$ to develop the commutator

$$[X, U(T_p + t)] = [X, U(t)U(T_p)] = [X, U(t)]U(T_p) + U(t)[X, U(T_p)]. \tag{2.64}$$

This relation is used to compute the evolution at time $T_p + t$ when we have already computed time T_p. Injecting this result in equation 2.61 gives us 3 terms that need to be computed, two for the evolution of $|\psi\rangle$ and one for $|\phi\rangle$:

$$|\psi(T_p + t)\rangle = [X, U(t)]\,|\phi(T_p)\rangle + U(t)\,|\psi(T_p)\rangle\,, \tag{2.65}$$

and

$$|\phi(T_p + t)\rangle = U(t)\,|\phi(T_p)\rangle\,. \tag{2.66}$$

Note that in the case where $T_p = 0$, $\langle\psi(T_p)|\psi(T_p)\rangle = 0$ by definition and does

not need to be computed. These two equations can also be rewritten as:

$$|\psi(T_{p+1})\rangle = [X, U(T_{p+1} - T_p)]\,|\phi(T_p)\rangle + U(T_{p+1} - T_p), |\psi(T_p)\rangle\,, \tag{2.67}$$

and

$$|\phi(T_{p+1}))\rangle = U(T_{p+1} - T_p)\,|\phi(T_p)\rangle\,. \tag{2.68}$$

We consider now how to compute $[X, U(t)]\,|\phi(T_p)\rangle$ using the Chebyshev orthogonal polynomials. In such a development, the time evolution operator is expressed:

$$U(t) = \sum_n c_n(t) P_n(\hat{H}). \tag{2.69}$$

For simplification, we further define

$$|\alpha_n(T_p)\rangle = P_n(\hat{H})\,|\phi(T_p)\rangle\,, \tag{2.70}$$

$$|\beta_n(T_p)\rangle = [\hat{X}, P_n(\hat{H})]\,|\phi(T_p)\rangle\,, \tag{2.71}$$

and

$$|\gamma_n(T_p)\rangle = P_n(\hat{H})\,|\psi(T_p)\rangle\,. \tag{2.72}$$

These relations allow us to simplify equations 2.65 and 2.66 as:

$$|\phi((T_p + t))\rangle = \sum_{n=0}^{N} c_n(t)\,|\alpha_n(T_p)\rangle \tag{2.73}$$

$$|\psi(T_p + t)\rangle = \sum_{n=0}^{N} c_n(t)\,|\beta_n(T_p)\rangle + c_n(t)\,|\gamma_n(T_p)\rangle\,. \tag{2.74}$$

The polynomials $P_n(\hat{H})$ obey the recursion relation, using the Chebyshev coefficient a_C and b_C:

$$b_C P_{n+1}(\hat{H}) = (\hat{H} - a_C) P_n(\hat{H}) - b_C P_{n-1}(\hat{H}), \tag{2.75}$$

and, for commutators,

$$\begin{aligned} b_C[\hat{X}, P_{n+1}(\hat{H})] &= [\hat{X}, (\hat{H} - a_C)P_n(\hat{H})] - b_C[\hat{X}, P_{n-1}(\hat{H})] \\ &= [\hat{X}, \hat{H}]P_n + \hat{H}[\hat{X}, P_n] - a_c[\hat{X}, P_n] - b_c[\hat{X}, P_{n-1}] \end{aligned} \tag{2.76}$$

From the recurrence of the polynomials applied to the states ϕ and ψ defined above, we get the three following recursion relations:

$$b_C \left|\alpha_{n+1}(T_p)\right\rangle = (\hat{H} - a_C) \left|\alpha_n(T_p)\right\rangle - b_C \left|\alpha_{n-1}(T_p)\right\rangle , \tag{2.77}$$

$$b_C \left|\gamma_{n+1}(T_p)\right\rangle = (\hat{H} - a_C) \left|\gamma_n(T_p)\right\rangle - b_C \left|\gamma_{n-1}(T_p)\right\rangle , \tag{2.78}$$

$$b_C \left|\beta_{n+1}(T_p)\right\rangle = (\hat{H} - a_C) \left|\beta_n(T_p)\right\rangle - b_C \left|\beta_{n-1}(T_p)\right\rangle + [\hat{X}, \hat{H}] \left|\alpha_n(T_p)\right\rangle . \tag{2.79}$$

This expression works well with periodic boundary conditions, as we only need the commutator between the position operator and the Hamiltonian, $[X, \hat{H}]$, for which only the distance between orbitals is required, and not the absolute position. Of course the extension of the wave function $X(E, t)$ must sill be smaller than the size of the cell with periodic boundary conditions.

In the end, what we need to compute are three recursion series, two if $T_p = 0$, which are defined over the Chebyshev polynomials. The interesting thing about this development is that it's proportionally more time effective to compute large time evolution step rather than smaller ones as shown in fig 2.3.

We can see that it's possible to compute $|phi\rangle$ and $|\psi\rangle$ at times $T_p + t_i$ which are intermediate between T_p and T_{p+1}. In order to do that we need to compute, in a first step, all the coefficients $c_n(t_i)$ for the chosen t_i for n between 0 and N. Then we define a $|phi(T_p + t_i)\rangle$ and $|\psi(T_p + t_i)\rangle$ for each t_i. Each time we compute a $|\alpha_n(T_p)\rangle$, $|\gamma_n(T_p)\rangle$, and $|\beta_n(T_p)\rangle$, we add the corresponding contributions to the wave functions.

As such we do not compute the $|\phi(T_p)\rangle$ and $|\psi(T_p)\rangle$ one after the other. Lets assume we want to evolve a state at $t = T_p$ to 10 other times, so that the last time is $t = T_p + 10\delta t$. It is shorter to compute the 10 times simul-

taneously as $|\phi(T_p + n\delta t\rangle = U(n\delta t)\,|\phi(T_p)\rangle$, rather than doing $|\phi(T_p + n\delta t\rangle = \sum_{i=1}^{n} U(\delta t)\,|\phi(T_p)\rangle$. We can do so because $|\alpha_n(T_p)\rangle$, $|\gamma_n(T_p)\rangle$, and $|\beta_n(T_p)\rangle$ only depend on the starting time and not the time of arrival. They are the same for all the times we want to compute, and only need to be computed once. The downside of this method is that we need to store 10 sets of $|\phi\rangle$ and $|\psi\rangle$, whereas we only need one if we compute the times by iteration. Then if we want to continue the development at further time, we define $t = T_p + 10\delta t$ as our new starting point T_{p+1}, and start again.

2.8 Conclusion

We have presented the methods we will be using throughout the thesis. Let us emphasize that the main interest of these methods is that they are non perturbative and do not require periodicity, as they can be expressed in real space. Thanks to that they have proved to be very well adapted to the problem of disordered systems. Concerning transport, this is, to our knowledge, the first time that these methods are applied to a 3D system, with complex electronic structure. We believe that this opens interesting perspectives in the field of modelling for material science.

Bibliography

[1] D. Mayou, "Calculation of the conductivity in the short-mean-free-path regime," *Europhysics Letters (EPL)*, vol. 6, pp. 549–554, jul 1988.

[2] D. Mayou and S.N. Khanna, "A real-space approach to electronic transport," *J. Phys. I France*, vol. 5, no. 9, pp. 1199–1211, 1995.

[3] M. H. Gutknecht, "A brief introduction to krylov space methods for solving linear systems," pp. 53–62, 2007.

[4] C. Lanczos, "An iteration method for the solution of the eigenvalue problem of linear differential and integral operators," *Journal of Research of the National Bureau of Standards*, vol. 45, Oct. 1950.

[5] P. Nevai, ed., *Orthogonal Polynomials*. Springer Netherlands, 1990.

[6] R. Haydock, "The recursive solution of the schrodinger equation," vol. 35 of *Solid State Physics*, pp. 215 – 294, Academic Press, 1980.

[7] M. Abramowitz, *Handbook of Mathematical Functions, With Formulas, Graphs, and Mathematical Tables,*. USA: Dover Publications, Inc., 1974.

[8] T. François, "Diffusion quantique et conductivité dans les systèmes apériodiques," *Thèse*, 2002.

Chapter 3

Tight-binding modelization

Contents

3.1 Introduction

In this section we introduce the key elements of atomic physics, necessary to build our system. A common way to approach this problem is via the density functional theory (DFT), and DFT has already been used extensively on perovskite. It suffers limitations, which make it less interesting in our study. It is quite computationally intensive, often limiting system sizes to a few hundred atoms, and their application to disordered and non-symmetrical systems is not

straightforward. Another well developed starting point for this study would be the tight binding method, originally proposed by Bloch [1] and further developed by Slater and Koster [2], and has already been extensively used in the study of semi-conductors and quasicristals [3] for example. This approach allows the consideration of disordered systems with a few millions orbitals, which appears to be essential to consider perovskites, due to the long range nature of the disorder we introduce.

We start by introducing the perovskite structure and some reminder of how the orbitals of each atoms are described. We continue by a description of how these orbitals are coupled to each other, via the Slater-Koster relations [2] and the spin orbit coupling, which has a great importance in MAPI.

This gives us the Hamiltonian in the perfect MAPI structure. As we focus on study of perovskite for solar cells however, we need to account for the effect the temperature T has on the lattice. We introduce three separated types of disorder which appear at $T = 300K$, namely, off diagonal disorder due to thermal displacement of the atoms, and diagonal disorder generated by the displacement of the atomic charges, or by rotation of the MA molecule.

These disorders have interesting properties on their own, and non trivial effects on MAPI's electronic structure, and we characterize them at the end of this chapter.

3.2 Atomic orbitals and cubic harmonics

The name perovskite historically refers to the mineral of chemical formula $CaTiO_3$, but has derived to describe any material with the same crystal structure. The original perovskite for solar cell applications is methylammonium lead triiodide ($CH_3NH_3PbI_3$) or MAPI, and the most efficient solar cell to dates are variations of MAPI with inclusion of different concentration of an other halide, usually brome or chlorine, or an other ion, usually caesium or formamidinium. As such we focused our effort on the description of the high temperature cubic phase of MAPI (3.1). In this configuration, every lead atom has six neighbouring iodine atoms, giving rise to the octahedron typical of the perovskite structure. The methylammonium molecule serves as an electron donor, ensuring charge neutrality

in the unit cell, but has energy levels too high from those of lead and iodine to participate directly in charge transport.

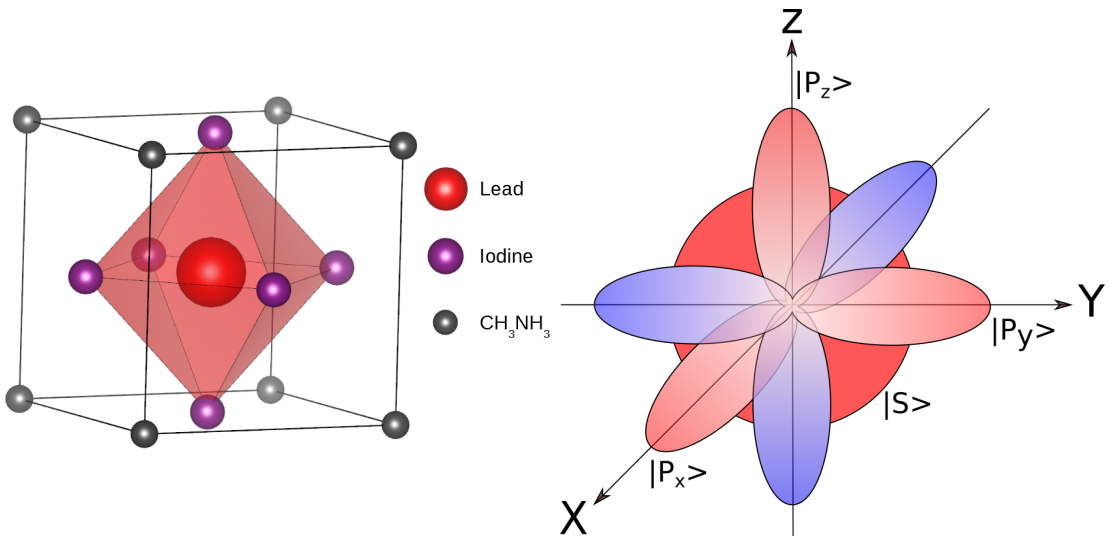

Figure 3.1: Left: Crystalline structure of MAPI in the cubic phase. Note the octahedron created by the iodine atoms around lead, characteristic of the perovskite structure. Right: Orbital representation an iodine or lead atom in the cubic orbital basis. Positive phases of the orbitals are represented in red while the negative phases part are in blue. Every atom is considered to be superposition of these orbitals

The states we need to consider for every atom are their outmost orbitals, also called valence orbitals, as they are the ones prone to hybridization. In the spherical harmonics basis, every orbital is described using four quantum numbers:

Principal quantum number n: Describes the shell on which the orbital is located, the bigger n is, the more distant the orbital is from the nucleus. This is the number which will identify the interacting orbitals.

Orbital quantum number ℓ: identifies the subshell considered, and the type and symmetry of the orbitals within, can vary between 0,..., n-1. It is related to the magnitude of the electrons' angular momentum within the orbital via the relation:

$$\hat{L}^2 \left|\ell, m\right\rangle = \hbar^2 \ell(\ell+1) \left|\ell, m_\ell\right\rangle , \tag{3.1}$$

where $\hat{L}$ is the total angular momentum operator, and $\hbar^2\ell(\ell+1)$ are the eigenvalues of the operator $\hat{L}^2$.

The magnetic quantum number $\mathbf{m}_\ell$ points to a specific orbital within that subshell, and distinguishes orbitals according to the projection of their angular momentum on an arbitrary axis (usually the z axis). As such $\hbar m_l$ are the eigenvalues of $\hat{L}_z$ and can vary between $-\ell$ and ℓ with integer steps.

The spin projection quantum number $\mathbf{m_s}$ representing the projection of the spin angular momentum, S, of the electron. S is an intrinsic properties of the electron and is always 1/2, and m_s can be either -1/2 or 1/2.

Lead and iodine configurations are as follow:

$$\text{I: [Kr]}5s^2 4d^{10} 5p^5, \tag{3.2}$$

$$\text{Pb: [Xe] } 6s^2 4f^{14} 5d^{10} 6p^2, \tag{3.3}$$

,where $[Kr]$ and $[Xe]$ refer to the core electronic structure of krypton and xenon, and the system is an hybridization of the $5s^2$ and $5p^5$ orbitals of iodine with the $6s^2$ and $6p^2$ of lead.
For isolated atoms, around which the potential has a spherical symmetry, one can factorize the wave function in a radial and angular part,which defines the spherical orbitals, of expression:

$$\phi_{n,\ell,m}(r,\theta,\psi) = f_{n,\ell}(r) Y_l^m(\theta,\psi), \tag{3.4}$$

where $f_{n,\ell}(r)$ is the radial part of the wave function and $Y_l^m(\theta,\psi)$ are the spherical harmonics. However, considering the cubic symmetry of MAPI, it is much more useful for us to project these orbitals from the spherical harmonic basis to the cubic harmonic one. The expression of the Hamiltonian is also greatly simplified in this basis. In this new basis the orbitals are redefined as linear combinations of spherical orbitals as follow:

$$|s\rangle = |\ell = 0, m = 0\rangle \tag{3.5a}$$

$$|p_z\rangle = |\ell = 1, m = 0\rangle \tag{3.5b}$$

$$|p_x\rangle = \frac{1}{\sqrt{2}}(|\ell = 1, m = -1\rangle - |\ell = 1, m = 1\rangle) \tag{3.5c}$$

$$|p_y\rangle = \frac{i}{\sqrt{2}}(|\ell = 1, m = -1\rangle + |\ell = 1, m = 1\rangle) \tag{3.5d}$$

This defines our new set of orbitals, the s orbital, still with spherical symmetry, and 3 directional p orbitals: p_x, p_y, p_z. We define the S orbital as having positive phase, and all P orbitals positive phase lobe pointing in the same direction as the x, y and z axis.

3.3 Tight binding Hamiltonian

Throughout all of this report we use a tight binding model approximation to describe our materials. In this model, one first considers the potential of isolated atoms, which gives orbitals as the eigenstates of this system. Then, when atoms are brought closer, as in a crystal, electrons from one atom start to feel the potential of their neighbours. A coupling arises between them, which induces the possibility for electrons to hop via quantum tunnelling from one atom to the other, and atomic levels can also be shifted by crystal field. The approximation behind tight binding is to suppose that the basis of orbitals of the isolated atoms remains a good basis for the global system. There is a decomposition between the on-site energies, which are the eigenenergies of the isolated atoms that can be shifted due to crystalline field effects, and the couplings with the neighbouring orbitals. We also neglect electron-electron interaction, with the exception of Pauli's exclusion principle, as charge carrier density is low in solar cells under sunlight exposition.

Such Hamiltonian is expressed as:

$$\begin{aligned}\hat{H} = &\sum_{i\mu\sigma} |i\mu\sigma\rangle\, \epsilon_{i\mu}\, \langle i\mu\sigma| + \sum_{i\mu,j\mu',\sigma} |i\mu\sigma\rangle\, t_{i\mu,j\mu'}\, \langle j\mu'\sigma| \\ &+ \sum_{i\mu\sigma,\mu'\sigma'} |i\mu\sigma\rangle\, \lambda_{i\mu\sigma,\mu'\sigma'}\, \langle i\mu'\sigma'|\,,\end{aligned} \tag{3.6}$$

where $\epsilon_{i\mu}$ is the onsite energy, of orbital μ on atom i, $t_{i\mu,,j\mu'}$ is the hopping integral between orbitals μ' on atom j and orbital μ on a neighbouring atom i, and $\lambda_{i\mu\sigma,\mu'\sigma'}$ is the spin orbit coupling between orbitals of the same atom, but of different spin σ and σ'. This type of Hamiltonian is very well suited for numerical studies as it generates a fixed spatial discretization of the material.

$$
\begin{array}{c}
 \\
\langle 0,S| \\
\langle 0,P_x| \\
\langle 0,P_y| \\
\langle 0,P_z| \\
\langle 1x,S| \\
\langle 1x,P_x| \\
\langle 1x,P_y| \\
\langle 1x,P_z| \\
\langle 1y,S| \\
\langle 1y,P_x| \\
\langle 1y,P_y| \\
\langle 1y,P_z| \\
\langle 1z,S| \\
\langle 1z,P_x| \\
\langle 1z,P_y| \\
\langle 1z,P_z|
\end{array}
\begin{array}{c}
\begin{array}{cccccccccccccccc}
|0,S\rangle & |0,P_x\rangle & |0,P_y\rangle & |0,P_z\rangle & |1x,S\rangle & |1x,P_x\rangle & |1x,P_y\rangle & |1x,P_z\rangle & |1y,S\rangle & |1y,P_x\rangle & |1y,P_y\rangle & |1y,P_z\rangle & |1z,S\rangle & |1z,P_x\rangle & |1z,P_y\rangle & |1z,P_z\rangle
\end{array} \\
\left(\begin{array}{cccccccccccccccc}
\epsilon_{S0} & 0 & 0 & 0 & t_{S0S1} & t_{S0P1} & 0 & 0 & t_{S0S1} & 0 & t_{S0P1} & 0 & t_{S0S1} & 0 & 0 & t_{S0P1} \\
 & \epsilon_{P0} & 0 & 0 & t_{P0S1} & t_{PP\sigma} & 0 & 0 & 0 & t_{PP\pi} & 0 & 0 & 0 & t_{PP\pi} & 0 & 0 \\
 & & \epsilon_{P0} & 0 & 0 & 0 & t_{PP\pi} & 0 & t_{P0S1} & 0 & t_{PP\sigma} & 0 & 0 & 0 & t_{PP\pi} & 0 \\
 & & & \epsilon_{P0} & 0 & 0 & 0 & t_{PP\pi} & 0 & 0 & 0 & t_{PP\pi} & t_{P0S1} & 0 & 0 & t_{PP\sigma} \\
 & & & & \epsilon_{S1} & 0 & 0 & 0 & 0 & 0 & 0 & 0 & 0 & 0 & 0 & 0 \\
 & & & & & \epsilon_{P1} & 0 & 0 & 0 & 0 & 0 & 0 & 0 & 0 & 0 & 0 \\
 & & & & & & \epsilon_{P1} & 0 & 0 & 0 & 0 & 0 & 0 & 0 & 0 & 0 \\
 & & & & & & & \epsilon_{P1} & 0 & 0 & 0 & 0 & 0 & 0 & 0 & 0 \\
 & & & & & & & & \epsilon_{S1} & 0 & 0 & 0 & 0 & 0 & 0 & 0 \\
 & & & & & & & & & \epsilon_{P1} & 0 & 0 & 0 & 0 & 0 & 0 \\
 & & & & & & & & & & \epsilon_{P1} & 0 & 0 & 0 & 0 & 0 \\
 & & & C.C & & & & & & & & \epsilon_{P1} & 0 & 0 & 0 & 0 \\
 & & & & & & & & & & & & \epsilon_{S1} & 0 & 0 & 0 \\
 & & & & & & & & & & & & & \epsilon_{P1} & 0 & 0 \\
 & & & & & & & & & & & & & & \epsilon_{P1} & 0 \\
 & & & & & & & & & & & & & & & \epsilon_{P1}
\end{array}\right)
\end{array}
\tag{3.7}
$$

3.4 Orbital couplings

As defined in section 3.3 the matrix elements of the Hamiltonian are:

$$t_{i\mu,j\mu'} = \langle i\mu\sigma | \hat{H} | j\mu'\sigma \rangle . \tag{3.8}$$

For two orbitals to have a non-zero coupling to each other, they need to overlap and their respective projection of angular momentum along the bond axis need to be identical. This leaves only a few cases to study, which are given by the Slater-Koster parameters [2]. All orbital couplings of interest are shown in figure 3.2, note that we restrict the couplings to first nearest neighbours. We label lead atoms and their respective orbital as 0, and we differentiate the three iodine atoms of the unit cell using their direction from the central lead. So the state $|1y, P_x\rangle$ refers to the P_x orbital of the iodine in the direction of y from lead. Iterating over

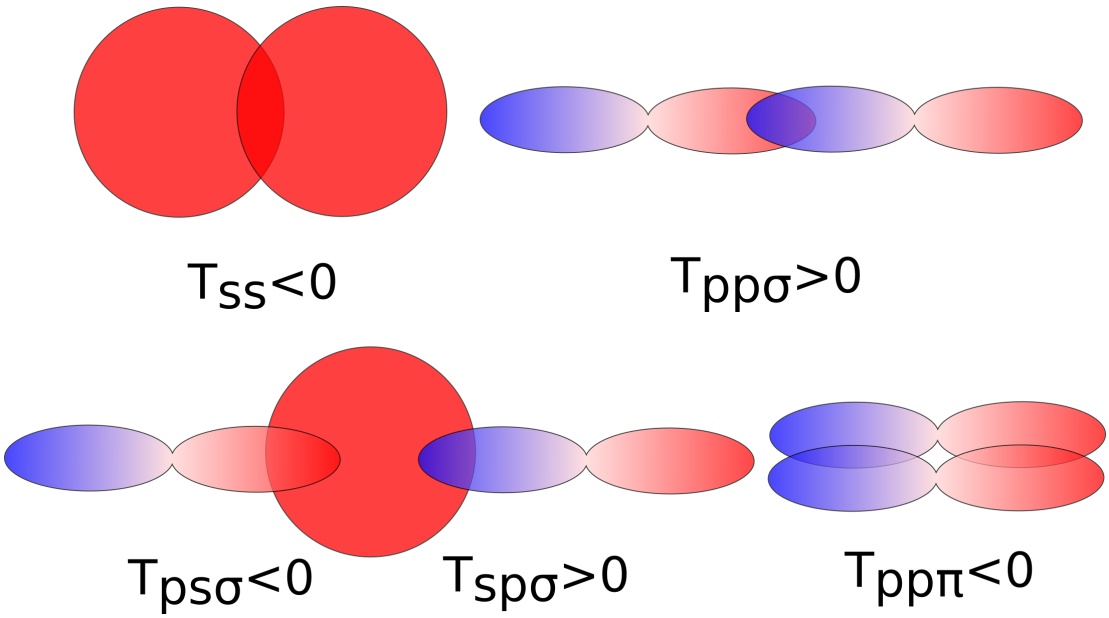

Figure 3.2: All existing couplings for our system. Red color indicates a positive phase and blue a negative one. The sign of the coupling is determined by the phases of the overlapping orbitals. The sign is negative if the overlap is done in region of same phase sign, and positive otherwise. Note that in the case of $t_{sp\sigma}$, the sign changes if we set the P orbital on the left of the S one and that $t_{ps\sigma} = -t_{sp\sigma}$.

all orbitals gives all the couplings. Note that where subscripts i or j are used they can take the values of x,y or z.

$\epsilon_{S0} = \langle 0, S| \hat{H} |0, S\rangle$, onsite energy of lead S orbital.

$\epsilon_{P0} = \langle 0, P_i| \hat{H} |0, P_i\rangle$, onsite energy of lead P orbitals.

$\epsilon_{S1} = \langle 1i, S| \hat{H} |1i, S\rangle$, onsite energy of iodine S orbital.

$\epsilon_{P1} = \langle 1i, P_j| \hat{H} |1i, P_j\rangle$, onsite energy of iodine P orbital.

$t_{S0S1} = \langle 0, S| \hat{H} |1i, S\rangle$, coupling between S of lead and S of iodine.

$t_{S0P1} = \langle 0, S| \hat{H} |1i, P_i\rangle$, coupling between S of lead and P of iodine.

$t_{P0S1} = \langle 0, P_i| \hat{H} |1i, S\rangle$, coupling between P of lead and S of iodine

$t_{PP\sigma} = \langle 0, P_i| \hat{H} |1i, P_i\rangle$, coupling between two P orbitals pointing to each other.

$t_{PP\pi} = \langle 0, P_i| \hat{H} |1j, P_i\rangle$, whith $j \neq i$, coupling between two P orbitals facing each other. The 16 by 16 Hamiltonian without spin-orbit coupling for one unit cell is shown in matrix 3.7.

3.5 Spin-orbit coupling

There exists an interaction between the electron spin in its own referential coupled to its orbital motion, and the electrostatic field of the nucleus, perceived as revolving around it. It is expressed as

$$\hat{H}_{soc} = \lambda \hat{L}.\hat{S}, \tag{3.9}$$

Where S is the spin angular momentum vector of the particle, L its angular momentum, and λ is the intensity of the coupling, which the depends on the nature of the atom.

By defining the total angular momentum $\hat{J}$:

$$\hat{J} = \hat{L} + \hat{S}, \tag{3.10}$$

we can derive that

$$\hat{J}^2 = (\hat{L} + \hat{S})^2 = \hat{L}^2 + \hat{S}^2 + 2\hat{L}.\hat{S} \tag{3.11}$$

$$\implies \hat{L}.\hat{S}\,|j,m_j\rangle = \frac{1}{2}(\hat{J}^2-\hat{L}^2-\hat{S}^2)\,|j,m_j\rangle = \frac{\hbar^2}{2}(j(j+1)-l(l+1)-s(s+1))\,|j,m_j\rangle\,, \tag{3.12}$$

where j, l, s are the quantum numbers corresponding to the quantities defined before. It is straightforward to show that for S orbitals ($l = 0$), $\hat{J} = \hat{S}$ and thus the intensity of the spin orbit coupling is null. For P orbital, $l = 1$, $s = \frac{1}{2}$, and $\frac{1}{2} \leq J \leq \frac{3}{2}$. This gives rise to a splitting in energy levels, the $J = \frac{3}{2}$ states are raised by $\hbar\lambda/2$ and the $J = \frac{1}{2}$ are lowered by $\hbar\lambda$.

We thus have the spin orbit Hamiltonian in the J basis, H_J, which we need to express in the cubic orbitals basis. This can be done using the Clebsch-Gordan coefficients, which are linking states in the J basis to the spherical orbital basis, and using the projection of the cubic orbitals, as defined before (reference). The Clebsch-Gordan matrix is, with J states writen as $|J, m_j\rangle$ and spherical orbitals as $\langle m_\ell, m_s|$ (short notation for $\langle \ell = 1, m_\ell, S = 1/2, m_s|$), written as

$$\begin{array}{c} \\ \langle\ 1,\ +1/2\,| \\ \langle\ 1,\ -1/2\,| \\ \langle\ 0,\ +1/2\,| \\ \langle\ 0,\ -1/2\,| \\ \langle -1, +1/2| \\ \langle -1, -1/2| \end{array} \begin{array}{c} \begin{array}{cccccc} |\frac{3}{2},\frac{3}{2}\rangle & |\frac{3}{2},\frac{1}{2}\rangle & |\frac{1}{2},\frac{1}{2}\rangle & |\frac{3}{2},-\frac{1}{2}\rangle & |\frac{1}{2},-\frac{1}{2}\rangle & |\frac{3}{2},-\frac{3}{2}\rangle \end{array} \\ \begin{pmatrix} 1 & 0 & 0 & 0 & 0 & 0 \\ 0 & 1/\sqrt{3} & \sqrt{2/3} & 0 & 0 & 0 \\ 0 & \sqrt{2/3} & -1/\sqrt{3} & 0 & 0 & 0 \\ 0 & 0 & 0 & \sqrt{2/3} & 1/\sqrt{3} & 0 \\ 0 & 0 & 0 & 1/\sqrt{3} & -\sqrt{2/3} & 0 \\ 0 & 0 & 0 & 0 & 0 & 1 \end{pmatrix} \end{array}. \tag{3.13}$$

Thus we can compute every element of the Hamiltonian in the cubic orbitals basis via

$$H_{soc,a,b} = \sum_{J,m_j} \langle P_a|J,m_j\rangle \langle J,m_j|\,H_J\,|J,m_j\rangle \langle J,m_j|P_b\rangle\,, \tag{3.14}$$

giving rise to the following Hamiltonian

$$H_{soc} = \frac{\hbar\lambda}{2}. \begin{array}{c} \\ \langle P_x\uparrow| \\ \langle P_y\uparrow| \\ \langle P_z\uparrow| \\ \langle P_x\downarrow| \\ \langle P_y\downarrow| \\ \langle P_z\downarrow| \end{array} \begin{array}{c} \begin{array}{cccccc} |P_x\uparrow\rangle & |P_y\uparrow\rangle & |P_z\uparrow\rangle & |P_x\downarrow\rangle & |P_y\downarrow\rangle & |P_z\downarrow\rangle \end{array} \\ \begin{pmatrix} 0 & -i & 0 & 0 & 0 & 1 \\ i & 0 & 0 & 0 & 0 & -i \\ 0 & 0 & 0 & -1 & i & 0 \\ 0 & 0 & -1 & 0 & i & 0 \\ 0 & 0 & -i & -i & 0 & 0 \\ 1 & i & 0 & 0 & 0 & 0 \end{pmatrix} \end{array}. \quad (3.15)$$

In the cubic orbitals basis the effect of the Hamiltonian is no longer seen as a splitting in term of energy levels, but as a complex coupling between different orbitals of the same atoms. In order to save space this Hamiltonian is stored separately from the rest of the Hamiltonian, as the couplings are complex. The spin orbit parameters for lead and iodine are as follows.

$\hbar\lambda(Pb)$	$\hbar\lambda(I)$
0.86	0.6

Table 3.1: Intensity of spin coupling in eV for lead and iodine [4]

3.6 Band structure

Because the lattice is periodical, Bloch's theorem states that the energy eigenstates of the system can be written a series of Bloch waves as

$$|\mu_{\vec{k}}\rangle = \frac{1}{\sqrt{N}} \sum_{\vec{R}} e^{i\vec{k}\vec{R}} |\mu_{\vec{R}}\rangle \,, \quad (3.16)$$

where $|\mu_{\vec{R}}\rangle$ represents an orbital in the basis of cubic harmonics at position $\vec{R}$, N is the number of unit cells and $\vec{k}$ is a vector of the first Brillouin zone. We remind that the Brilloin zone is the primitive cell in reciprocal space, and the primitive vectors of the reciprocal lattice are defined as:

$$
\begin{aligned}
b_1 &= 2\pi \frac{a_2 \wedge a_3}{a_1.(a_2 \wedge a_3)}, \\
b_2 &= 2\pi \frac{a_3 \wedge a_1}{a_1.(a_3 \wedge a_1)}, \\
b_3 &= 2\pi \frac{a_1 \wedge a_2}{a_1.(a_1 \wedge a_2)},
\end{aligned}
\tag{3.17}
$$

where a_1, a_2, a_3 are the vector of the real space lattice. In the case of our cubic lattice, the reciprocal space is also a cubic lattice, of lattice constant $2\pi/a$, with $a = 6.29\mathring{A}$. Because the Hamiltonian does not couple states of different $\vec{k}$, we have

$$
\langle \mu_{\vec{k}} | \hat{H} | \nu_{\vec{k}} \rangle = \hat{H}_{\mu\nu}(\vec{k}) = \sum_{\vec{R}} e^{i\vec{k}\vec{R}} \langle \vec{0}\mu | \hat{H} | \vec{R}\nu \rangle , \tag{3.18}
$$

where $\langle \vec{0}\mu|$ is an orbital of the starting cell at the origin, and $|\vec{R}\nu\rangle$ is an orbital of the cell at position $\vec{R}$. The sum has to be taken as long as $\langle \vec{0}\mu| \hat{H} |\vec{R}\nu\rangle$ does not vanish, *i.e.* up to first neighbours in our case. Because the onsite energies and spin orbit couplings are between orbitals at the same position, they are k-independent and only the hopping parameters are modified.

Diagonalization of the Hamiltonian gives 16 eigenenergies, or 32 with spin orbit coupling, for each $\vec{k}$ considered, which is the band structure of MAPI. It is common to show the dispersion relation $E(\vec{k})$ along a path through several high symmetry point which are Γ in $(0,0,0)$, R in $(1,1,1)$, X in $(0,1,0)$, and M in $(1,1,0)$.

All these parameters, including spin-orbit coupling, need to be fitted to recover the band structure of MAPI obtained from *ab-initio* computations [5]. This reference presents an ab initio calculation by the self-consistent GW method, which reproduces the gaps well unlike the Local Density Approximation (LDA) which usually underestimates them by a factor of two. This calculation also provided effective masses in good agreement with the experimental ones. The first set of parameters we used are based on a study by Boyer-Richard *et al.* [4], which correctly reproduced bandgap but, as we realized latter, gave effective masses 2 to 3 times lower than expected. Results using these parameters can still be found in annex, and may still be relevant for systems with lower effective masses.

Therefore, we developed our own set of parameters to correct this problem

based on their original study. In figure 3.3, we compare the band structure of three set of parameters to the *ab-initio* data, around the R point where the bandgap lies. The parameters are those of Boyer-Richard *et al.* (fig 3.3c), our own, which are closer to Harrison's parameters [6], with effective masses for electron and hole of $m^*_{e,h} \simeq 0.15me$ (fig 3.3a), and another with $m^*_{e,h} \simeq 0.2me$ (fig 3.3b). We find the fit to be better with $m^*_{e,h} \simeq 0.15me$, which is a bit lower than what is expected from exciton effective mass measurement. We believe the difference is explained by the existence at low temperature of polaronic effect which tend to increase the mass by 30%. These parameter, expressed in our basis, can be found in tables 3.2 and 3.3.

The band structure of MAPI is shown in figure 3.4. We can see from this band structure that the bandgap in MAPI is located at the R point and is strongly affected by the spin orbit coupling. We can also see that the bands lying at $-14eV$, associated to the iodine S states which are very low in energy, are almost flat and thus weakly coupled to the rest of the system.

ϵ_{S0}	ϵ_{P0}	ϵ_{S1}	ϵ_{P1}
-9.01	2.34	-13.01	-1.96

Table 3.2: Onsite energies (eV) of the s and p orbitals of iodine and lead [4]

t_{S0S1}	t_{S0P1}	t_{P0S1}	$t_{PP\sigma}$	$t_{PP\pi}$
-1.1	1.19	-0.7	1.9	-0.7

Table 3.3: Slater-Koster parameters in MAPI

3.7 Disorder model

First of all, let's emphasize that the disorder breaks the translational invariance symmetry. As a result, Bloch's theorem no longer applies and the reciprocal space loses its relevance. This is the reason why we are developing a direct space technique in the next chapter. A proper model of disorder is essential to describe

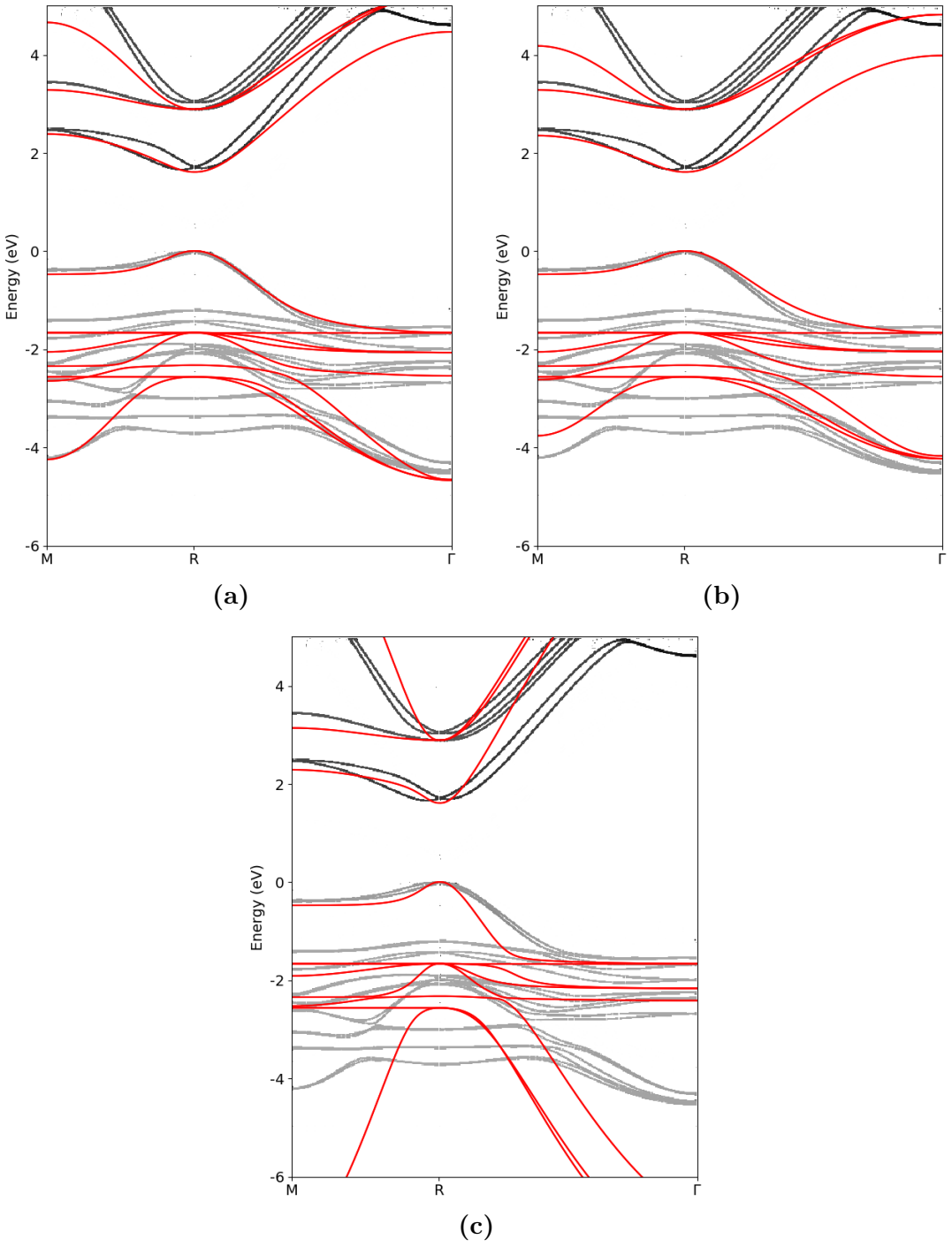

Figure 3.3: Computed band strucutre for different parameter set (red) over *ab initio* band structure (grey). **(a)** Band structure with $m_h^* = 0.16m_e$ and $m_e^* = 0.17m_e$, **(b)** Band structure with $m_h^* = 0.20m_e$ and $m_e^* = 0.21m_e$, and **(c)** Boyer-Richard *et al.* band structure

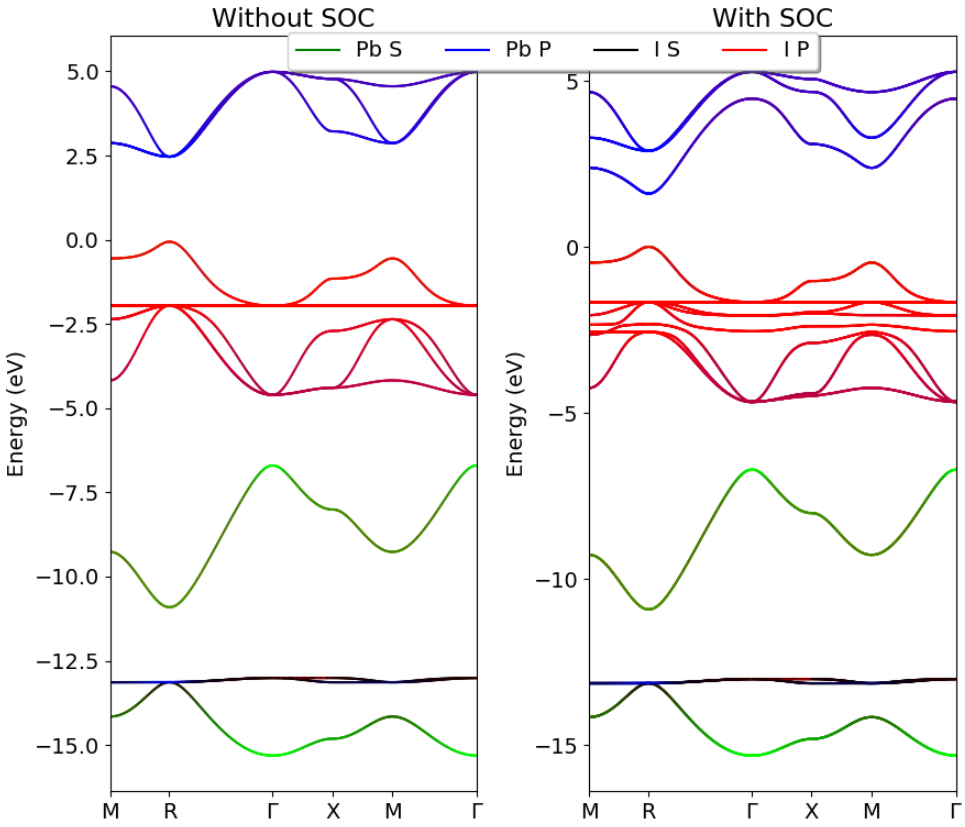

Figure 3.4: Band structure of MAPI, without spin orbit coupling (SOC) **(left)** and with spin orbit coupling **(right)**. The bandgap is situated at the R point and is strongly affected by spin-orbit coupling, diminishing from $2.0eV$ to $1.6eV$. The rest of the band structure is weakly affected, except for the fact that the number of band is doubled.

transport properties in MAPI. The onsite energies of atoms are sensitive to the electrical potential inside the material and the hopping parameters are related to the distance between orbitals, closer orbitals being more strongly coupled. We focus our study on the inherent thermal disorder inside the bulk material since effects of ion migration and grain boundaries are dependant on processing methods, ageing and other parameters. In the thermally perfect system, the disorder is necessarily linked to the dynamic of the components of the material, namely, lead, iodine and methyl-ammonium. We are left with three phenomenon causing

disorder in the system: variation of hopping integrals due to thermal motion of the atoms, variation of electrostatic potential due to displacement of the charges carried by the atoms (Pb and I), and rotation of the dipole moment of the MA molecule. Disorder on hopping parameters is called off-diagonal disorder, while dipole moments and MA molecule modify onsite energies, and are called diagonal disorders, in reference to the Hamiltonian matrix depicted in formula 3.7. We develop an approximation which gives a snapshot of the tight binding Hamiltonian. We discuss at the end of this chapter how we treat the dynamical effect.

Off diagonal disorder: We model the dynamics of atoms as Einstein oscillators, where all atomic displacements are statistically independent, with harmonic and isotropic potentials. This model gives good phonon population at room temperature, but brings the approximation that the motion of every atom is independent from its neighbour's, and that there is no an-harmonic contribution. For such a model the elementary probability dP to find an atom at position between position x and $x + dx$ is

$$\frac{dP(x, x+dx)}{dx} = \sqrt{\frac{k\beta}{2\pi}} e^{-\beta k x^2/2} \tag{3.19}$$

Thus the distribution of atoms around their equilibrium position is a gaussian of standard deviation $\sigma = 1/\sqrt{k\beta}$. We use the single particle potential computed by Tyson et al. [7] to determine the constant factor k of lead and iodine, which are all considered isotropic, even for iodine. In terms of energies the values of $\hbar\omega = \hbar\sqrt{k/m}$ are $\hbar\omega_{Pb} \simeq 6.4meV$ for lead and $\hbar\omega_I \simeq 5.3meV$ for iodine. The typical displacement values associated are defined by:

$$\sqrt{m_{Pb,I}} x_{Pb,I} = \frac{\sqrt{k_B T}}{\omega_{Pb,I}}, \tag{3.20}$$

with $m_{Pb} = 207.2amu$, $x_{Pb} = 0.12\mathring{A}$ for lead, and $m_I = 126.9amu$, $x_I = 0.18\mathring{A}$ for iodine. These values imply displacement of around 10% of the interatomic distance. We then displace every atom according to the probabilty given in equation 3.19. The change in distance and angle between atoms has an effect on hopping

parameters. The Slater-Koster's relations [2] give the projection of orbitals on one another according to the angle. This couples orbitals that, for symmetry reasons in the perfect cubic lattice, were not coupled before and increases drastically the computation cost. We also renormalise the hopping parameters with distance via a factor $(d_0/d)^2$, which implies modification of the hopping parameters of the order of 20% on average.

Diagonal disorder: Because the atoms are charged, we need to consider the modification of the electrical potential they create when they are displaced. From the point of view of the Hamiltonian, the displacement of an atomic charge is equivalent to adding one charge on the modified position and one opposite charge on the original site. This effectively creates dipole moments on every displaced site. The dipole moment is defined as:

$$\vec{p} = q\vec{d}, \tag{3.21}$$

where q is the displaced charge and $\vec{d}$ is the distance between the poles. The potential created by a dipole at position 0 on a given $\vec{R}$ point is:

$$V(\vec{R}) = \frac{1}{4\pi\epsilon_r\epsilon_0}\frac{\vec{p}.\vec{R}}{R^3}, \tag{3.22}$$

with ϵ_0 the vacuum permittivity and ϵ_r the relative permittivity of the material. Acoustic phonons actually generate little electrical potential in the material and electrical disorder is mostly caused by optical phonons, with atoms moving out of phase toward each other, and especially longitudinal optical (LO) phonon mode, that create modulations of the charge density.

The potential created by all displaced atoms has contribution from all modes, but only some LO modes are important. Thus we can consider a fictitious dynamical matrix such that all phonon eigen-modes are unchanged but their frequency ω is put equal to ω_{LO}. With this approximation, the population of modes with $\omega < \omega_{LO}$ is underestimated while the population of those with $\omega > \omega_{LO}$ is overestimated. Yet, the important LO modes have their correct population. This fictitious dynamical matrix is diagonal, corresponding to independent local atomic oscillators, with the same ω_{LO}, whatever the direction of oscillation. This is again an Einstein model. The LO phonon energy bands of MAPI lies in the 8 to 14meV

range [8], and we shall make ω_{LO} vary in this range, although 12 to 14 meV seems the most realistic. ω_{LO} becomes one of our major parameter in the rest of the study, due to the strong impact of diagonal disorder on electronic structure and transport properties.

The potential created by the dipoles on one point $\vec{r}$ is thus the sum over all the charges displacements:

$$V(\vec{r}) = \frac{1}{4\pi\epsilon_r\epsilon_0}\sum_i \frac{q_i\vec{d_i}.\vec{R_i}}{R_i^3}, \tag{3.23}$$

with $\vec{R_i} = \vec{r} - \vec{r_i}$, where $\vec{r_i}$ is the position of dipole i. Using that the probability distribution of $\vec{d_i}$ is Gaussian we can write that $\vec{d_i} = \sigma_i\vec{d_{0i}}$, where $\vec{d_{0i}}$ correspond to the distribution according to a Gaussian of standard deviation equal to 1, and in our case $\sigma_i = 1/\sqrt{k_i\beta} = 1/\sqrt{m_i\omega_{LO}^2\beta}$. The equation becomes:

$$V(\vec{r}) = \sum_i \frac{1}{4\pi\epsilon_0\epsilon_r\omega_{LO}\sqrt{\beta}}\frac{q_i\vec{d_{0i}}.\vec{R_i}}{\sqrt{m_i}R^3} = \sum_i \frac{1}{4\pi\epsilon_0\sqrt{W}}\frac{q_i\vec{d_{0i}}.\vec{R_i}}{\sqrt{m_i}R^3}, \tag{3.24}$$

where

$$\frac{1}{\sqrt{W}} = \frac{\sqrt{k_BT}}{\epsilon_{r,\infty}\omega_{LO}} = \frac{\sqrt{m_\alpha}x_{\alpha,LO}}{\epsilon_{r,\infty}}, \tag{3.25}$$

where $\alpha = Pb$ or I, and becomes our only variable parameter regarding the intensity of this disorder, once the charges q_i are known. $\epsilon_{r,\infty}$ denotes the high frequency limit of the relative dielectric permittivity. Here $x_{\alpha,LO}$ is the typical displacement associated to the LO modes, for either lead or iodine. For the charges of the atoms, we use the Born charges computed by Pérez-Osorio et al.[9]. Born charges are defined as the variation of the polarisation in a direction i for the displacement of an ion in direction j as

$$Z_{ij}^* = \frac{1}{e}\frac{\delta P_i}{\delta d_j}, \tag{3.26}$$

Where e is the electron charge, and P and d are the polarization and displacement. These charges are often different from the formal ionic charge because of covalent and ionic effect. Indeed, because atoms are bound to each other via elec-

tron sharing, when they are displaced they will also tend to displace the charges of neighbouring atoms. In MAPI the formal charges are +2 for lead and -1 for iodine, but the Born charges are +4.42 for lead, and -4.15 for iodine if the displacement is in direction of the lead atom, and -0.7 otherwise. These high values, which lead to important effect of the diagonal disorder, may appear surprising, but are also observed in ABO_3 perovskite materials, where Born charges are often two to three times bigger than the formal charges [10]. The value of -0.7 for iodine can also be found through integration of the projected density of states up to the Fermi level, which shows that this value is the charge displaced without effects of covalence. The charge is isotropic for lead because its environment has a cubic symmetry, while it is anisotropic for iodine as it is only bound in the direction of lead.

MA molecules: While not participating in charge transport, the molecules also carry a dipole moment of $2.1D$. The energy of interaction between neighbour methylammonium ions has been found to be, at least in the cubic phase, weaker than the thermal energy [11] [12], to the point where correlation in their orientation will be neglected. The MA molecules are thus taken as randomly oriented and we compute the potential associated using equation 3.23, with the exception that our only variable is ϵ_r here.

Concerning MAPI's relative dielectric constant ϵ_r, studies show that its value varies between 6 to 25 [5] in the frequency range of interest to us. Optical phonons have the smallest time constant, of all the phenomena in the material, a few tenth of picoseconds. This implies that they are less screened than the MA molecules, which have a much larger characteristic time of evolution, of the order of a few picoseconds. We expect to have $\epsilon_r \simeq 6$ for LO phonons and $\epsilon_r \simeq 25$ for MA molecules.

The order of magnitude of the changes on hopping integrals and onsite energy can be found in figure 3.5. We can already see that, whatever the dielectric constant we choose for the MA molecules, their disorder is weaker than the one of the LO phonons. The effect of atomic displacement on inter-orbital coupling is found to be of the order of 20% of the original integral, which also appears as very strong disorder. Interestingly, because the hopping integral depends on $1/r^2$, disorder tends to increase the average values of the hopping integrals, which could tend to increase the bandgap with increasing temperature.

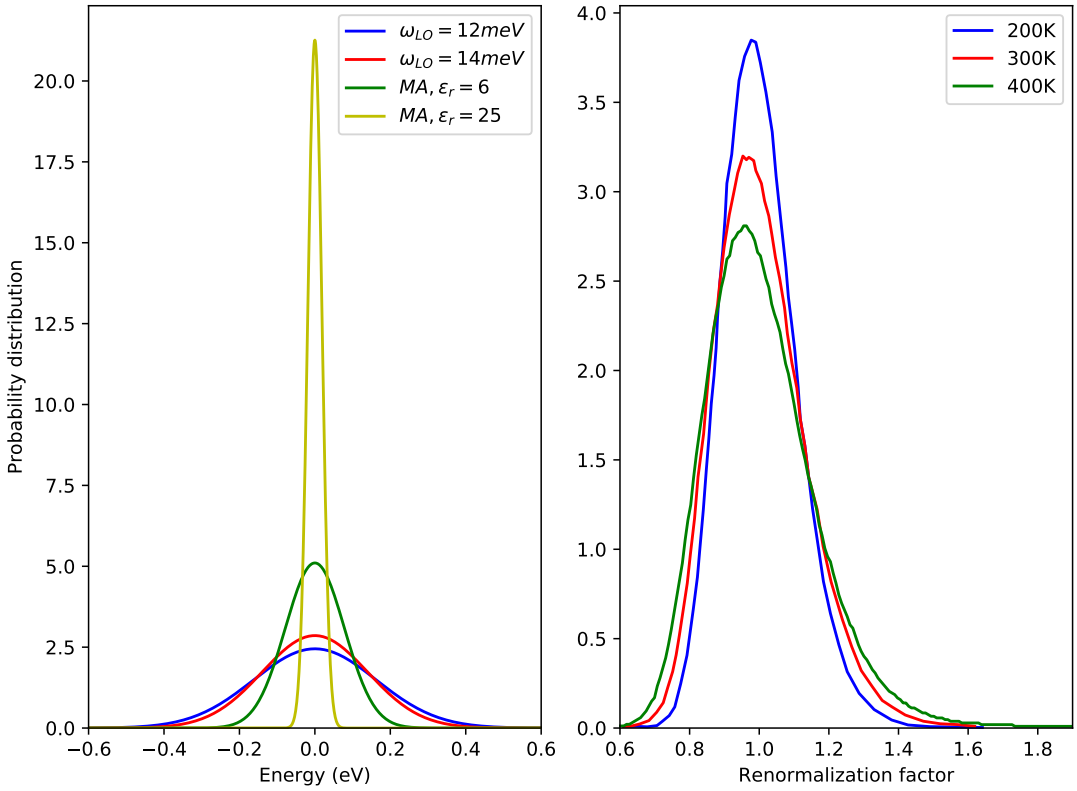

Figure 3.5: left: Distribution of orbitals onsite energy variations for different LO phonon energies and MA dielectric constants. Right: Distribution of renormalization of the hopping parameters for different temperatures.

We note that, because the LO modes account for only a small fraction of all the modes, the atomic position we use to compute the hopping integrals and the position of the charges are not correlated. As such, no correlations between off-diagonal and diagonal disorder will be considered in our calculations.

3.8 The electrostatic potential

In this section we discuss the convergence, amplitude and spatial coherence of the electrostatic potential. The potential created by a dipole is long ranged, decreasing with distance as $1/r^2$, however, the number of dipole moment around

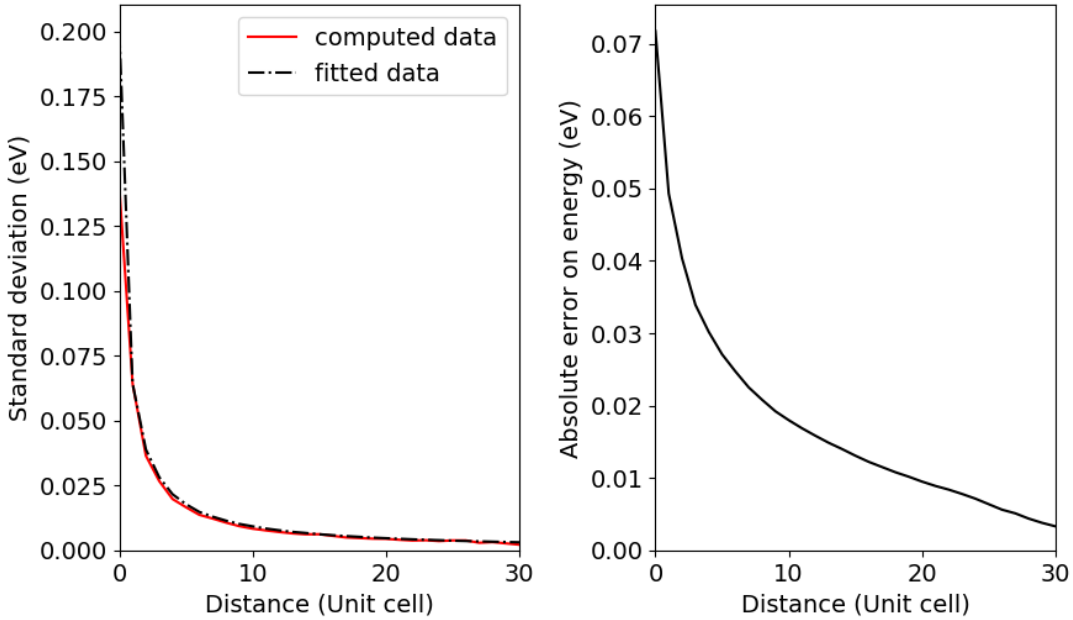

Figure 3.6: Left: Standard deviation of the potential created by each cubic dipole shell as a function of distance. The total potential on an atom is the sum of the potentials created by all these shells around it. The computed data are fitted by a law in $1/\sqrt{n}$ where n is the number of dipole in the shell. It shows that dipoles in shells far away from the site tend to compensate each other and thus participate less on the potential. Right: Averaged absolute error on on-site energies as a function of maximum integration distance. For integration up to 25 unit cells, the potential are converged to $\pm 5meV$ on average, which is smaller than our energy resolution.

any atom also increase proportionately to r^2. For this reason the potential is expected to converge slowly, and only because the dipole moment are randomly oriented, and as such dipoles on sufficiently large shells around an atom should statistically cancel each other. This can be understood through the central limit theorem which states that the sum of randomly distributed variables tends, for large enough samples, towards a Gaussian distribution. This distribution is centred around the expectation value and its variance varies proportionally to $1/\sqrt{n}$. If we are interested in the sample average of the distribution

$$\hat{X}_n = \sum_{i=1}^{n} \frac{X_i}{n} \tag{3.27}$$

then we have that for large n:

$$\mu_{\hat{X}_n} = \mu, \tag{3.28}$$

and

$$\sigma_{\hat{X}_n} = \frac{\sigma}{\sqrt{n}}, \tag{3.29}$$

where μ and σ are the expectation value and the standard deviation of the sample. Let us consider cubic shells around an atom, so that the shell number n is made of all the unit cells that are n cells away from the atom's cell. Then each shell contains more and more dipoles as distance increases, and the potential it causes is proportional to μ and $\sigma_{\hat{X}_n}$, which tends to zero. This is verified in Fig. 3.6, where computed data are fitted with this law, and from which we deduce the distance to which dipole interaction is important. Dipole up to at least 25 cells away need to be considered for the potential to be converged, and this enforces the system size to be at least a cube of $50 \times 50 \times 50$ unit cells. Note that by using periodic boundary conditions, we have no surface effects.

The electrical disorder caused by LO phonon is found to be important at room temperature, $T = 300K$, for $\omega_{LO} < 12.5meV$, and $\epsilon_r = 6$, of the order of $0.2eV$ on average. The potential caused by the MA molecules is much smaller in comparison, no matter the value of ϵ_r selected. Indeed the MA molecules cause similar disorder to LO phonon with an energy of $\omega_{MA} = 25meV$, if we consider $\epsilon_r = 6$, and $\omega_{MA} = 100meV$, with $\epsilon_r = 25$. Furthermore, because both disorders are independent but of the same nature, it is easier for us to consider that the MA molecules act simply as renormalization of the LO phonon energy, and have otherwise a nearly negligible effect. This is supported by findings of their effect on charge carrier mobilities, described in chapter 4.

Another interesting feature of the electrical disorder is its spatial coherence. The electrical potential varies on length scales of a few unit cells (see Fig. 3.7), leading to the apparition of positively and negatively charged region in the crys-

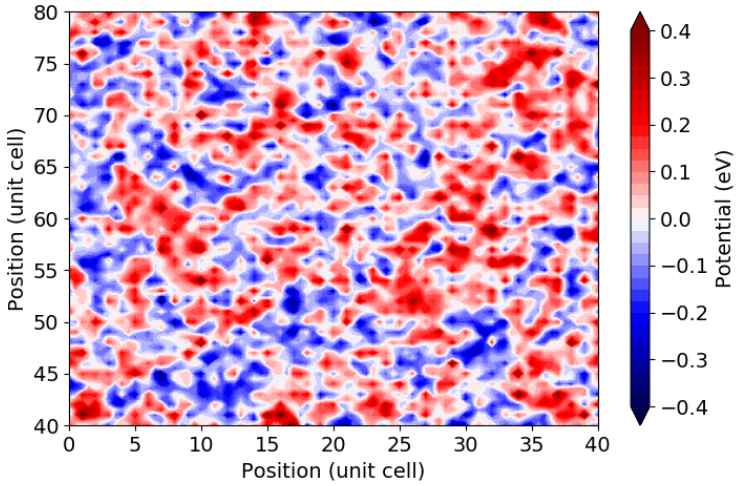

Figure 3.7: Intensity of the electrical disorder caused by LO phonons as function position for a planar cut inside a MAPI sample. The parameter for the disorder is $W \propto k_B T/m\epsilon_r^2\omega_{LO}^2$, with $\epsilon_r = 6$, $T = 300K$ and $\omega_{LO} = 12meV$.

tal. Note that the size of the positive and negative clusters does not vary with disorder $1/W = k_B T/\epsilon_r^2\omega_{LO}^2$, which only changes the scale of the variation, but not the spatial coherence. This phenomenon is reminiscent of what happens at a p-n junction in traditional semi-conductors, and might explain unusually low recombination rate and long carrier lifetimes in MAPI. Furthermore, the impact this coherence has on bandgap and transport properties cannot be replicated with simple Anderson random disorder.

3.9 Conclusion

We shortly summarize the model we have built before going in more detailed results. We have built a tight binding Hamiltonian, around the lead-iodine matrix, the MA molecules having energy levels too high to participate in transport. It is made of the valence orbitals of both atoms, which are of s and p type. The onsite energies, hopping parameters and spin-orbit couplings have been fitted to reproduce MAPI's band structure as computed *ab-inito*, and we bring an important correction to the tight binding parameter pp_σ proposed by Boyer-Richard *et.al* [4].

When taking into account the thermal disorder, this Hamiltonian can have

disorder on its diagonal and off diagonal parameters. We have developed a model that gives a snapshot of the Hamiltonian, without anharmonic effects. The spin orbit coupling is considered independent of disorder. We have three sources of disorder. Thermal excitation of the atoms has effect on both diagonal and off-diagonal parameters, but through different mean. We model these effects using two separate Einstein models, meant to represent the two contributions. The first one represents modification of the hopping parameters due to atomic displacements and its intensity is proportional to the typical displacement of the atoms

$$\sqrt{m_{Pb,I}}x_{Pb,I} = \frac{\sqrt{k_B T}}{\omega_{Pb,I}}, \tag{3.30}$$

where $\omega_{Pb,I}$ is the pulsation of either lead or iodine, and $x_{Pb,I}$ is the typical atomic displacement at room temperature. We have $\omega_{Pb} \simeq 6.4meV$ and $\omega_I \simeq 5.3meV$, which corresponds to displacements of $x_{Pb} = 0.12\mathring{A}$ and $x_I = 0.18\mathring{A}$. The variance of these independent displacements add up for the variance of the total distance, and we find a variance on atomic distance of $0.37\mathring{A}$. These values induce a variation of around 20% of the hopping integrals.

The second Einstein model is meant to represent the effect of charge density fluctuation due to LO phonon modes. It's intensity depends only on the variable

$$\frac{1}{\sqrt{W}} = \frac{\sqrt{k_B T}}{\epsilon_{r,\infty}\omega_{LO}} = \frac{\sqrt{m_\alpha}x_{\alpha,LO}}{\epsilon_{r,\infty}}, \tag{3.31}$$

$\epsilon_{r,\infty} = 6$ for LO phonons, and ω_{LO} is the pulsation of the LO phonon bands, $x_{Pb,I,LO}$ is the typical displacement caused by LO phonons.

This phenomenon can thus be compared to the off diagonal disorder through the value of x_{LO}, and to the MA molecule through the dipole moment P_{LO}. The typical values with $\omega_{LO} = 12meV$ are $x_{Pb,LO} = 0.06\mathring{A}$ and $x_{I,LO} = 0.077\mathring{A}$. We can see that the displacements due to LO phonon are about half that of the one used for off diagonal disorder.

The LO phonon are the strongest source of electrical disorder in the material, due to their high Born charges, which are typical or perovskites materials such as the ABO_3 family. The Born charge of lead is isotropic and is $4.42e$, while the charge of iodine depends on the direction. For a displacement in the lead-iodine

direction it is $-4.15e$, while it is $-0.72e$ in the perpendicular direction. This creates dipole moments with typical values of $P_{Pb,LO} = 1.28D$ for lead, $P_{I,LO} = 1.20D$ for displacements of iodine in the lead-iodine direction, and $P_{I,LO} = 0.20D$ perpendicular to it.

Finally MA molecules also create diagonal disorder. Their orientation can be considered random, provided that we are close to room temperature, and their disorder is not temperature dependent. It is proportional to

$$E_c = \frac{P}{V\epsilon_{r,0}\epsilon_0}, \tag{3.32}$$

where $P = 2.1D$ is the dipole moment of the MA molecule, and $\epsilon_{r,0} = 25$ is the low frequency value of the dielectric constant, V is the volume of the unit cell, and E_c is a characteristic electrical field. While the dipole moment of the MA molecule is twice bigger than the characteristic dipole moment of the LO phonon, their dynamic is much slower and they are 4 times more screened by the environment.

Because all the dipole are independent, their effect on potential disorder add up, proportionally to the square of their dipole moment. If we do this sum, we have one MA dipole of $2.1D$, 3 lead dipole of $1.28D$, one for each direction, 3 iodine dipole of $1.2D$, for displacement in the lead direction, and 6 iodine dipole of $0.2D$ in the other directions. We directly see that the iodine movement that are not in the lead direction generate negligible amount of electric potential, less than 2% of the total potential. For the MA molecule, with $\epsilon_r = 6$, they represent around 30% of the total potential, while with the more realistic $\epsilon_r = 25$, they represent around 2% of the total potential. As such the disorder of the MA molecules is smaller than that of the LO phonon, and effectively acts as a renormalization of ω_{LO} as it is of the same nature, statistically independent and much smaller than it.

We point to the fact that all 3 disorder are statistically independent. With all these, we make a static snapshot of the Hamiltonian. We can see that for all disorders we have ω_{LO}, ω_{Pb}, and $\omega_I << k_B T$ around room temperature. For this reason, we consider that the emission or absorption of phonons does not modify the Boltzmann distribution, but essentially acts like a dephasing effect. This implies that this dephasing effects occur only after a time $\tau_{in} \simeq 1/\omega_{LO}$ since LO phonon

are the main source of disorder. Beyond this time, the potential will have changed, and we need to consider the loss of coherence in the system and inelastic effects (see chapter 4).

Bibliography

[1] F. Bloch, "Über die quantenmechanik der elektronen in kristallgittern," *Zeitschrift für Physik*, vol. 52, pp. 555–600, Jul 1929.

[2] J. C. Slater and G. F. Koster, "Simplified LCAO method for the periodic potential problem," *Phys. Rev.*, vol. 94, pp. 1498–1524, Jun 1954.

[3] F. Triozon, J. Vidal, R. Mosseri, and D. Mayou, "Quantum dynamics in two- and three-dimensional quasiperiodic tilings," *Phys. Rev. B*, vol. 65, p. 220202, Jun 2002.

[4] S. Boyer-Richard, C. Katan, B. Traoré, R. Scholz, J.-M. Jancu, and J. Even, "Symmetry-based tight binding modeling of halide perovskite semiconductors," *The Journal of Physical Chemistry Letters*, vol. 7, no. 19, pp. 3833–3840, 2016. PMID: 27623678.

[5] F. Brivio, K. T. Butler, A. Walsh, and M. van Schilfgaarde, "Relativistic quasiparticle self-consistent electronic structure of hybrid halide perovskite photovoltaic absorbers," *Phys. Rev. B*, vol. 89, p. 155204, Apr 2014.

[6] W. A. Harrison, "Solid state theory," *McGraw Hill Book Company*, 1970.

[7] T. A. Tyson, W. Gao, Y.-S. Chen, S. Ghose, and Y. Yan, "Large thermal motion in halide perovskites," *Scientific Reports*, vol. 7, no. 1, p. 9401, 2017.

[8] A. D. Wright, C. Verdi, R. L. Milot, G. E. Eperon, M. A. Pérez-Osorio, H. J. Snaith, F. Giustino, M. B. Johnston, and L. M. Herz, "Electron-phonon coupling in hybrid lead halide perovskites," *Nature Communications*, vol. 7, p. 11755 EP, May 2016. Article.

[9] M. A. Pérez-Osorio, R. L. Milot, M. R. Filip, J. B. Patel, L. M. Herz, M. B. Johnston, and F. Giustino, "Vibrational properties of the organic–inorganic halide perovskite $CH_3NH_3PbI_3$ from theory and experiment: Factor group analysis, first-principles calculations, and low-temperature infrared spectra," *The Journal of Physical Chemistry C*, vol. 119, no. 46, pp. 25703–25718, 2015.

[10] P. Ghosez, J.-P. Michenaud, and X. Gonze, "Dynamical atomic charges: The case of ABO_3 compounds," *Phys. Rev. B*, vol. 58, pp. 6224–6240, Sep 1998.

[11] S. Govinda, B. P. Kore, M. Bokdam, P. Mahale, A. Kumar, S. Pal, B. Bhattacharyya, J. Lahnsteiner, G. Kresse, C. Franchini, A. Pandey, and D. D. Sarma, "Behavior of methylammonium dipoles in $MAPbX_3$ (X = Br and I)," *The Journal of Physical Chemistry Letters*, vol. 8, no. 17, pp. 4113–4121, 2017. PMID: 28812901.

[12] N. P. Gallop, O. Selig, G. Giubertoni, H. J. Bakker, Y. L. A. Rezus, J. M. Frost, T. L. C. Jansen, R. Lovrincic, and A. A. Bakulin, "Rotational cation dynamics in metal halide perovskites: Effect on phonons and material properties," *The Journal of Physical Chemistry Letters*, vol. 9, no. 20, pp. 5987–5997, 2018.

Chapter 4

The Drude -Anderson model for quantum transport

Contents

4.1 Introduction

Before presenting results in the next chapter, we build the Drude-Anderson model of transport, which is an essential tool for studying the raw data that we obtained on quantum diffusion. We use this model to extract physical parameters and analyse the mobility and terahertz conductivity of MAPI.

We first start by a reminder of Drude semi-classical theory of transport, on which a lot of studies on perovskites are based. From this we derive expressions for a few quantities of interest.

However this model does not allow to describe localization interference effects that are expected from the Ioffe-Regel criterion (see below). Therefore we introduce the Anderson model of localization, and explain in which situation localization is expected to happen, and how it does.

We then present a purely quantum approach of transport via the Kubo formalism in section 4.4. This formalism relates conductivity in the material to the mean quadratic spread of charge carriers through the lattice. It perfectly takes into account localization effects, and introduces the concepts of diffusion and velocity correlation on which we build the Drude-Anderson model

Finally we present the Drude-Anderson model in itself. It is a phenomenological extension of the Drude model, based on the fully quantum velocity correlation function. This model fits our numerical data very well, and we show some results of diffusion alongside the fitted curve. The concordance between the model and the results allows the extraction of the physical parameters behind transport in MAPI, such as diffusion length or scattering time.

4.2 The Drude model

Transport is the phenomenon of electrical current flowing as a response to an applied electric field. The goal here is to compute the coefficients linking the current to the applied field. The Drude model of transport [1, 2] is based on a semi-classical description of electrons. We present its first principles here as it defines some quantities of interest to us. Note that k, r, E, v are three dimensional vectors, respectively the wave vector, the position, the electric field and the velocity, but for simplification we do not show them with arrows in the equations. Electrons are assimilated as a series of Bloch wave functions [3] defined as

$$\phi(r) = e^{ikr}u(r), \tag{4.1}$$

where $u(r)$ is periodic with the same periodicity as the lattice. In the perfect crystal, the dynamics of wave packets build out of such waves are described by the following equation:

$$\frac{dr}{dt} = v_n(k) = \frac{1}{\hbar}\frac{\partial \epsilon_n(k)}{\partial k}, \tag{4.2}$$

and

$$\frac{dk}{dt} = -\frac{e}{\hbar}E(r,t), \tag{4.3}$$

where $v_n(k)$ is the group velocity of the electron, $\epsilon_n(k)$ is it's relation dispersion inside the band n and $E(r,t)$ is the applied electric field. These formulas are only valid for weak fields, where there is no inter band transition, and for which the variation of the electric potential on the wave function size is small compared to other typical energies. The fact that electrons are moving is not enough to have an electrical current. Indeed, with no external field, electrons and hole move in all directions in the material and the resulting current is zero. However when a field is applied, they are all accelerated according to the field and a drift velocity appears. We define the drift velocity v_d from this group velocity, which is the average over all k and band n of the group velocity multiplied by occupation of the states, $f_n(k)$

$$v_d = \frac{1}{n_e}\sum_n \int \frac{d^3k}{(2\pi)^3} f_n(k) v_n(k) \tag{4.4}$$

where n_e is the number of electrons. It is directly related to the current density as

$$J = -e n_e v_d, \tag{4.5}$$

with $-e$ the electron charge. In the semi classical approximation, we consider that electrons in between collision act as free particles with a renormalized mass m^*, which gives a form for the dispersion relation:

$$\epsilon_n(k) = \frac{\hbar^2 k^2}{2m^*}, \tag{4.6}$$

and

$$v_n(k) = \frac{\hbar k}{m^*}. \tag{4.7}$$

If we do not take into consideration collisions with defects or phonons, the

charge carriers are accelerated to infinite momentum by the field. The way these collision are treated is through the relaxation time approximation. We assume that the effect of the collisions is to relax the electrons to their equilibrium distribution where $v_d = 0$ over a characteristic time τ. τ is of the order of a few $10^{-15}s$ to a few $10^{-13}s$ for most material. In the simplest case, the collision can be treated as a friction force, giving the formula

$$\frac{dv_d}{dt} = -\frac{eE}{m^*} - \frac{v_d}{\tau}, \tag{4.8}$$

and at long time the solution becomes

$$v_d = -\frac{eE\tau}{m^*} = -\mu E, \tag{4.9}$$

where μ is the mobility of the carriers, an experimentally significant quantity. We deduce that we have

$$\mu = \frac{e\tau}{m^*}, \tag{4.10}$$

and that the conductivity of the material is

$$\sigma = \frac{J}{E} = en\mu = \frac{ne^2\tau}{m^*}. \tag{4.11}$$

In the simplest theories, τ is computed from quantum description, using the Fermi golden rule. A quantity often used to determine the nature of transport in a material is it's optical conductivity. This value is the conductive response of the crystal as a function of the pulsation ω of the exciting field. From equation 4.8,it is expressed as

$$\sigma(\omega) = \frac{ne^2\tau}{m^*}\frac{1}{1 - i\omega\tau}. \tag{4.12}$$

The real part of the conductivity, which is related to the energy dissipation in the material, is written:

$$\mathrm{Re}\,\sigma(\omega) = \frac{ne^2\tau}{m^*}\frac{1}{1 + (\omega\tau)^2}. \tag{4.13}$$

There is a peak when $\omega \to 0$ which is considered as a signature of semi-classical

transport and is known as the Drude peak. This model however suffers from some limitations. Indeed no optical transition of high energy, on each side of the bandgap for example, can be considered in this model. Furthermore, in the case of highly disordered system the periodicity of the lattice is lost, and the concept of Bloch waves disappears. Since the wave nature of the electron is not considered here, no localization effects, due to interferences, can be taken into account.

4.3 The Anderson localization

Anderson showed in 1958 [4] that, given a strong enough disordered potential, electrons can become localized, which means that their spatial extension is limited. This leads to the theory of localization in disordered systems, which gave an explanation for multiple phenomenons, including metal-insulator transition in some doped semi-conductors. We give here a very brief introduction to the theory of localization, much more explanations can be found in the review articles [5, 6].

Anderson model is defined as a mono-orbital Hamiltonian:

$$\hat{H} = \sum_i \epsilon_i \left|i\right\rangle \left\langle i\right| \sum_{i,j} t \left|j\right\rangle \left\langle i\right|, \tag{4.14}$$

where ϵ_i is the onsite energy, and t is the hopping integral, which couples first neighbours only. The orbitals being all of the same nature, all onsite energies and hopping parameters are the same, in the absence of disorder. This model can be defined in all dimensions. In the simplest cases, in 1D it is a chain, in 2D, the atoms are on a square lattice, and in 3D they are on a cubic lattice. The disorder introduced by Anderson is a disorder of onsite energies, that varies randomly from site to site.

The Anderson model is in many ways different from the model we have built in section 3. The major difference with our Hamiltonian is double. First we have a more complex situation, with multiple atoms, each having multiple orbitals, that are on a non-cubic lattice. Secondly our disorder includes both off-diagonal disorder and onsite energy, and is not random, as we have showed it is spatially coherent. Despite these differences, Anderson model which has been generalized to more complex systems is a good starting point to understand how, where and

when localization happens.

In a perfect crystal, Bloch theorem shows that electronics states are extended, meaning they can diffuse through the whole material, and diffuse in a ballistic way. With small additional disorder, and in a 3D case, the states are still extended, but their propagation becomes diffusive, as we have shown in section 4.2. However this is not true in presence of strong enough disorder, and Anderson has shown that with sufficient disorder, electronic states could become localized. These states are localized in a region, which has a characteristic length ξ, called localization length. The smaller ξ is, the more the state is localized. These states can be seen as electrons trapped in potential wells they can't escape from. Three important parameters define if a state is extended or localized: the dimension of the system, the intensity of the disorder, and the energy of the state. Generally speaking, the bigger the disorder, the more the states are localized, and the closer they are to the band edges, the faster they localize too.

In 1D, states are always localized, no matter the intensity of the disorder. The same holds true for 2D materials, but, at equal disorder, the states are less localized than in 1D.

For 3D materials, two scenarios are possible. Above a certain intensity of disorder, all states are localized, but below this value, extended and localized states can coexist, see figure 4.1. These two types of states are separated by a so-called mobility edge. Indeed the states near the band edges tend to be localized, while those in the center are extended. As such the localization length decrease when approaching the band edges, and increases and diverges when approaching the mobility edge.

This notion of mobility edge was introduced by Mott and explained the metal-insulator transition observed in some semi-conductors, where one could, through doping the material, change the Fermi level from one side or the other of the mobility edge. We point out that the extended states show band like conduction behaviour, while the conduction for the localized states happens through thermally activated hopping. In chapter 5 we propose a scenario for MAPI, close to the Thouless regime, which adds an intermediate regime between the localized states and the extended states. In this regime, electron localize quickly, but the dynamic of the lattice breaks the confinement and allows carriers to diffuse. We call this

regime the adiabatic quantum localization scenario.

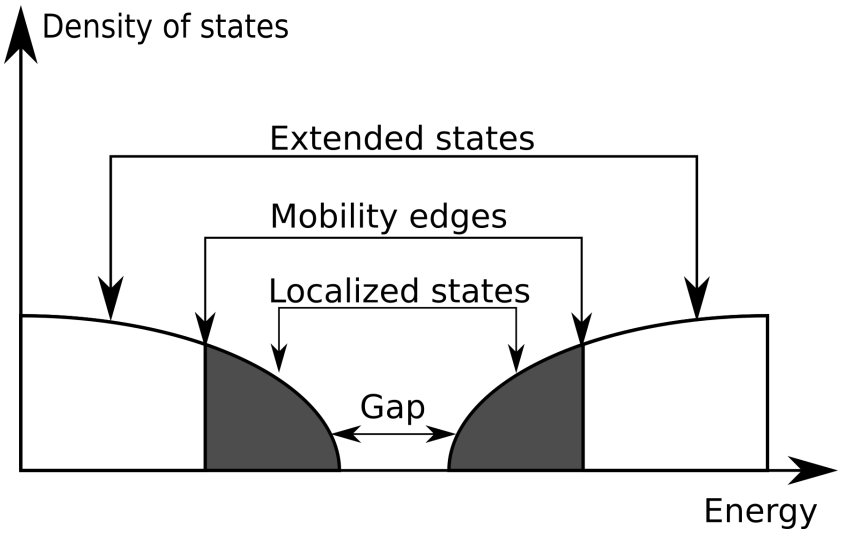

Figure 4.1: Schematic view of the position of the localized states, extended states, bandgap and mobility edges, in a disordered 3D semiconductor.

The Ioffe-Regel criterion is a way of assessing the effect of interferences in a system at a given energy. Considering the wave-vector $k = 2\pi/\lambda$, with λ the wave length, and l the mean free path, the Ioffe-Regel criterion states that interference effects are strong and lead to Anderson localization if $kl < 1$. We can express this relation in terms of energy, relating the energy of a state, counted from the band edge, and the energy broadening due to scattering. This criterion becomes $E_c\tau/\hbar < 1$, where E_c is the energy of the state and τ is the scattering time.

In the case of MAPI, if we consider the typical mobilities and effective masses of $\mu = 100cm^2/(V.s)$ and $m^* = 0.15m_e$, as well as the formula:

$$\mu = \frac{e\tau}{m^*}, \tag{4.15}$$

then we find typical scattering energies $E = \hbar/\tau \simeq 80meV$. This energy is much bigger than the thermal energy $k_BT \simeq 25meV$ and the polaron formation energy $E_{polaron} = 30meV$ [7, 8]. According to the Ioffe-Regel criterion this indicates the possibility of quantum interferences that cannot be neglected, and even some possible complete localization. This suggests also that for such disorder the polaron is not stable. This is why we present results obtained by neglecting polaronic effect

and taking fully into account localization effects.

4.4 Kubo formulas for conductivity

The Kubo formalism[9, 10] provides an expression of the conductivity of a system as a linear response to a external electric field. Here we build the Kubo formulas for conductivity in three steps. First we look at the absorption of energy in a material when a small electric field is applied. This is done through Fermi golden rule. From this we derive the the Kubo-Greenwood formula of conductivity in itself. Finally we relate this formula to the mean squared displacement operator and the velocity correlation function, which are the quantities we actually are computing.

First, we approach the problem using perturbation theory and linear response. Doing so we study the response of the system to a small perturbation, by using it's properties without perturbation. So, let's assume we apply a time dependent external electrical field on our material, of expression:

$$E(t) = E_0 cos(\omega t)\vec{u_x}, \tag{4.16}$$

where E_0 is the amplitude of the field, ω it's pulsation and $\vec{u_x}$ it's direction. This electrical field is linked to the vector potential, A, such as, using Coulomb gauge, $\nabla.A = 0$, we have $E = -\partial A/\partial t$ and

$$A(t) = -\frac{E_0}{2i\omega}(e^{i\omega t} - e^{-i\omega t})\vec{u_x}. \tag{4.17}$$

Now, the Hamiltonian of a charged particle in a vector potential is

$$\hat{H}(t) = \frac{1}{2m}(\hat{P} - qA(x,t))^2 + qV(x,t) = \hat{H}_0(t) + \delta\hat{H}(t), \tag{4.18}$$

where $\hat{P}$ is the momentum operator, $V(x,t)$ is the scalar potential, and q is the electron's charge. We develop this expression as the sum of the unperturbed Hamiltonian $\hat{H}_0(t)$, and a small perturbation due to A, of which we keep only first order terms, so that

$$\delta\hat{H}(t) = \frac{2q\hat{P}.A(t)}{2m} = q\hat{V}_x.A(t), \tag{4.19}$$

with V_x the velocity operator, which is given by

$$V_x = \frac{1}{i\hbar}[X, H]. \tag{4.20}$$

The eigenstates of the undisturbed system are by definition not coupled, but $\delta\hat{H}(t)$ induces coupling between these states. Fermi golden rule states that the probability of transition between an eigenstates $|n\rangle$ and $|m\rangle$ over time t is:

$$p_{nm}(t) = \frac{1}{\hbar^2}\left|\int_0^t dt' e^{it'(E_m - E_n)/\hbar} \langle m|\, \delta\hat{H}(t")\, |n\rangle\right|^2, \tag{4.21}$$

For long time, *i.e.* $t \to \infty$, and using the expression of the Dirac delta function in term of exponentials,

$$\delta(x-a) = \frac{1}{2\pi}\int_{-\infty}^{\infty} e^{ip(x-a)}dp, \tag{4.22}$$

we can develop the transition probability into:

$$\frac{p_{nm}(t)}{t} = \frac{\pi e^2 E_0^2}{2\hbar\omega^2} \langle m|\, \hat{V}_x\, |n\rangle^2 (\delta(E_m - E_n + \hbar\omega) + \delta(E_m - E_n - \hbar\omega)). \tag{4.23}$$

This equation implies that transition is only possible between eigenstates separated by $\hbar\omega$. A transition to a higher energy states implies that the material system absorbed energy, while the opposite means the system released energy. Furthermore, there can be no transition between an empty states into another, i.e. the occupation of the density of states $f(E_n) = 0$, or if the arriving state is full, i.e. $f(E_m) = 1$. Electron are fermions and follow the Fermi-Dirac distribution,

$$f(E) = \frac{1}{e^{(E-\mu)/k_b T} + 1}. \tag{4.24}$$

Adding a factor 2 for spin orbit coupling, we can determine the power absorbed in the system, as the sum over all possible states transitions, ascending and descending:

$$P = \frac{\pi e^2 E_0^2}{\hbar\omega 2}[-\hbar\omega \sum_{n,m} f(E_n)(1-f(E_m)) \left\langle m\right| \hat{V_x} \left|n\right\rangle^2 (\delta(E_m - E_n + \hbar\omega) \\ +\hbar\omega \sum_{n,m} f(E_n)(1-f(E_m)) \left\langle m\right| \hat{V_x} \left|n\right\rangle^2 + \delta(E_m - E_n - \hbar\omega)]. \tag{4.25}$$

The first term correspond to transition to a states E_m with lower energy than E_n, while the second correspond to the case where $E_n < E_m$. After changing the summation order in the first sum, and because the Dirac function and $\left\langle m\right| \hat{V_x} \left|n\right\rangle$ are symmetrical, we get

$$P = \pi e^2 E_0^2 \hbar \sum_{n,m} \frac{f(E_n) - f(E_m)}{\hbar\omega} |\left\langle m\right| \hat{V_x} \left|n\right\rangle|^2 \delta(E_m - E_n - \hbar\omega). \tag{4.26}$$

Once we have the power absorbed by the material we can find the real part $\sigma(\omega)$ of the conductivity via Ohm's law, dividing by the material's volumes V and the average electric field $E_0^2/2$:

$$\sigma(\omega) = \frac{2\pi e^2 \hbar}{V} \sum_{n,m} \frac{f(E_n) - f(E_m)}{\hbar\omega} |\left\langle m\right| \hat{V_x} \left|n\right\rangle|^2 \delta(E_m - E_n - \hbar\omega), \tag{4.27}$$

which we can express a a continuous integral and a trace operator, a form that we prefer:

$$\sigma(\omega) = \frac{2\pi e^2 \hbar}{V} \int_{-\infty}^{\infty} \frac{f(E) - f(+\hbar\omega)}{\hbar\omega} Tr[\hat{V_x} \delta(E - \hat{H}) \hat{V_x} \delta(E + \hbar\omega - \hat{H})] dE. \tag{4.28}$$

This expression is the Kubo-Greenwood formula in itself. We can now relate $\sigma(\omega)$ to the mean squared displacement $X^2(t)$. As such we need to develop the expression further, and we reuse equation 4.22 to replace

$$\delta(E + \hbar\omega - \hat{H}) = \frac{1}{2\pi\hbar} \int_{-\infty}^{\infty} e^{-i(\hat{H}t - Et)/\hbar} dt, \tag{4.29}$$

in the trace, and the definition of the density of states per unit of volume $n(E)$:

$$n(E) = \frac{Tr[\delta(E - \hat{H})]}{V}. \tag{4.30}$$

to make the time evolution operator appear, and we write:

$$\sigma(\omega) = e^2 \int_{-\infty}^{\infty} e^{i\omega t} dt \int_{-\infty}^{\infty} \frac{f(E) - f(E + \hbar\omega)}{\hbar\omega} n(E) < \hat{V}_x(0)\hat{V}_x(t) >_E dE, \tag{4.31}$$

The value $< \hat{V}_x(0)\hat{V}_x(t) >$ correlates velocity at time t to the original velocity.

The quantities we actually want to look at are the thermodynamically averaged quantities, to account for the repartition of holes and electrons in MAPI at room temperature. We can replace the Fermi-Dirac distribution by the Boltzmann distribution, as we always have $(E - \mu) >> k_B T$. Then these values are computed as, using the mean squared displacement as an example

$$X^2(t) = \frac{\int X^2(E,t) n(E) e^{-\beta E} dE}{\int n(E) e^{-\beta E} dE}, \tag{4.32}$$

but this relation holds true for all the operators we consider. The integral technically goes up to a reference energy E_0 for holes, and starts from it for electrons. However, because E_0 lies in the bandgap, far away from the band edges, its exact value does not matter. All the quantities we present below are thermodynamically averaged in this way.

We define the velocity self correlation function, which is

$$C(t) = \frac{1}{2} \langle \hat{V}_x(t)\hat{V}_x(0) + \hat{V}_x(0)\hat{V}_x(t) \rangle . \tag{4.33}$$

It is linked to the mean square displacements of charge carriers as

$$\frac{dX^2(t)}{2dt} = \int_0^t C(t')dt'). \tag{4.34}$$

After more simplifications we now have two formula for the optical conductivity:

$$\sigma(\omega) = ne^2 \frac{tanh(\beta\hbar\omega/2)}{\hbar\omega/2} Re \int_0^{\infty} e^{i\omega t} C(t) dt = ne\mu(\omega), \tag{4.35}$$

or

$$\sigma(\omega) = -ne^2\omega^2 \frac{tanh(\beta\hbar\omega/2)}{\hbar\omega} Re \int_0^\infty e^{i\omega t} X^2(t) dt. \tag{4.36}$$

Finally we note that for perfectly localized charged carriers, the mean squared displacement is constant at long time, which means that

$$\frac{dX^2(t)}{2dt} = 0 \implies \int_0^\infty C(t')dt') = 0. \tag{4.37}$$

We know that $C(t=0) =< \hat{V}_x^2 >> 0$ and it follows that at short time the velocity correlation function is positive $C(t) > 0$. So, carriers can only be localized if C becomes negative at some point, meaning that the electron comes back towards it's original location, with $C(t \to \infty) < 0$. It is this backscattering possibility that we build into the Drude-Anderson model in the next section.

4.5 The Drude-Anderson model

In order to get the most out of our quantum diffusion calculations in chapter 5, it is a necessity to have a model describing the physical process at hand. We do this by building upon the traditional Drude model of electrical conduction. We have shown in section 4.2 that the probability for an electron to undergo a collision over a short period of time dt is inversely proportional to the average time between collisions, τ, so that $dP = dt/\tau$.

After such event the electron is scattered in a random direction. This implies a loss of correlation between the original velocity and the velocity at time t as t increases. The function relating this quantity is the velocity self-correlation function, $C(t)$, which is defined via the velocity operator $\hat{V}_x$, which was previously introduced in 4.33, as

$$C(t) = \frac{1}{2} \left\langle \hat{V}_x(t)\hat{V}_x(0) + \hat{V}_x(0)\hat{V}_x(t) \right\rangle. \tag{4.38}$$

In Drude's model this quantity varies according to the probability of collision as

$$C(t) = Ce^{-t/\tau}. \tag{4.39}$$

Here we add the possibility of electron backscattering in the system [11]. Indeed, the fact that, in some cases, charge carriers can be localized indicates that collisions tend to return to the vicinity of their original position, as shown in equation 4.37. This creates a negative correlation with the original velocity, as the carrier effectively travels back to where it came from. We write

$$C(t) = C_C e^{-t/\tau_C} - C_B e^{-t/\tau_B}, \tag{4.40}$$

where C_C and τ_C are related to the classical diffusion behaviour, and where C_B and τ_B relate to the backscattering events. Because backscattering happens after multiple collision events, we always have $\tau_B > \tau_C$, and typically $\tau_B \simeq 2\tau_C$ to $4\tau_C$ as found in our study.

Finally, in the non-polaronic case that we consider, the lattice dynamics tends to break localization and backscattering effects. We introduce τ_ϕ which is the de-phasing time for the electron wave function due to interaction with the dynamical lattice, and which tends to soften the backscattering effects. The final form of $C(t)$ becomes

$$C(t) = C_C e^{-t/\tau_C} - C_B e^{-t/\tau_B} e^{-t/\tau_\phi}. \tag{4.41}$$

The model we use here varies slightly from the model presented in [11]. In this article, the model is used on 2D material and de-phasing is taken to affect the whole correlation function, *i.e.* $C(t) = C_0(t)e^{-t/\tau_\phi}$, while in our model we consider that de-phasing effects only affect the backscattering part of the equation. We recall that the inclusion of this inelastic de-phasing process allows us to extrapolate the results from our static Hamiltonian to the actual dynamic structure.

Using equation 4.34, which is the link between mean square displacement and the velocity time correlation function, with a static lattice (in the limit where $\tau_\phi \to \infty$), we derive the static formula of $X_s^2(t)$:

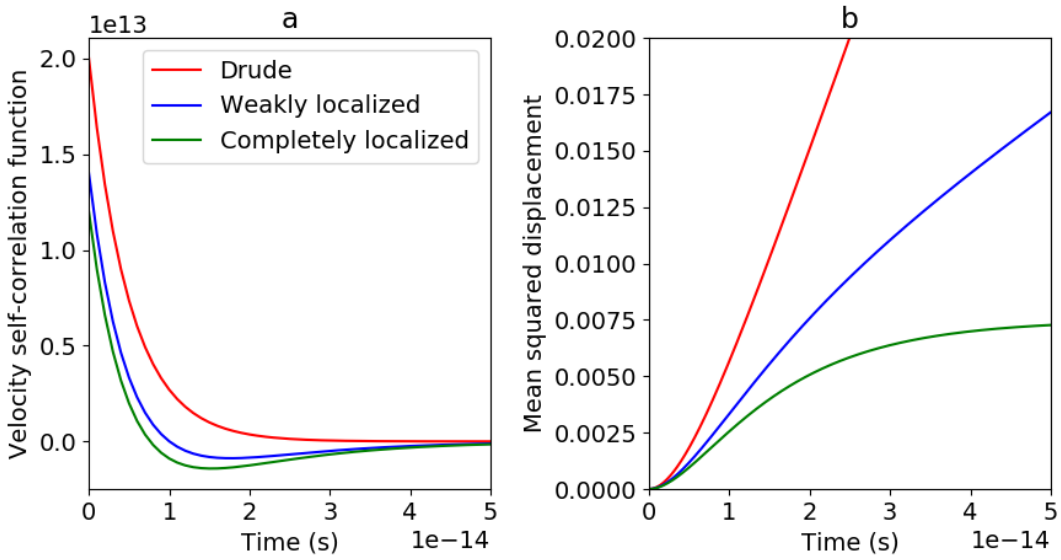

Figure 4.2: **(a)** Velocity self-correlation function as a function of time for different regimes. **(b)** Corresponding mean squared displacement as function of time.

$$\frac{X_s^2(t)}{2} = C_C\tau_C^2(e^{-t/\tau_C} - 1) - C_B\tau_B^2(e^{-t/\tau_B} - 1) + t(C_C\tau_C - C_B\tau_B). \tag{4.42}$$

This gives a formula for the mean free path of the charge carriers, which is

$$L_{mfp} = \sqrt{X^2(\tau_C)} \simeq \frac{C_C\tau_C^2}{e}, \text{ in the limit where } \frac{\tau_B}{\tau_C} >> 1. \tag{4.43}$$

Furthermore, the diffusion coefficient of the charge carriers is related to $X_s^2(t)$ as

$$D = \lim_{t\to\infty} \frac{X_s^2(t)}{2t} = C_C\tau_C - C_B\tau_B \tag{4.44}$$

and to the mobility, which is

$$\mu_s = \frac{eD}{k_bT} = \frac{e}{k_BT}(C_C\tau_C - C_B\tau_B). \tag{4.45}$$

In the case of fully localized charge carriers, $C_C\tau_C - C_B\tau_B = 0$, and we can derive the localization length of the charge carriers from equation 4.42:

$$L_{LOC}^2 = X^2(t \to \infty) = 2C_C\tau_C^2(\frac{\tau_B}{\tau_C} - 1). \tag{4.46}$$

From the formulas of the mean free path and the localization length, we can see that we always have $L_{LOC} \simeq 3$ to $4L_{mfp}$. Note however that, while we always can compute L_{LOC}, it is well defined only in the case of perfectly localized carriers.

In the case of non localized electrons, $C_B = 0$, and in the case of electrons completely localized at long times, we have $C_C\tau_C = C_B\tau_B$. We introduce the factor R as a tool to estimate the importance of the localization effects, which we define as

$$R = \frac{\mu_s}{\mu_C} = \frac{C_C\tau_C - C_B\tau_B}{C_C\tau_C}. \tag{4.47}$$

This ratio expresses the remaining static mobility μ_s as a percentage of the mobility without backscattering effects. As such $R = 1$ if there is no backscattering, and $R = 0$ if charge carriers are fully localized.

Furthermore, if we now consider the lattice dynamic, with a finite τ_Φ, and using l'Hôpital's rule we show that the equations remain the same, τ_C is unchanged, while τ_B is rescaled as $1/\tilde{\tau}_B = 1/\tau_B + 1/\tau_\phi$.

Reusing the static mobility definition, we find that the total mobility is the sum of a static contribution, and one added by the lattice dynamic:

$$\mu = \mu_S + \mu_{LD}, \tag{4.48}$$

with

$$\mu_{LD} = \frac{e}{k_bT}\frac{L^2(\tau_\Phi)}{2\tau_\Phi}, \quad L^2(\tau_\Phi) = \frac{2C_B\tau_B^2}{1 + \tau_B/\tau_\Phi}, \tag{4.49}$$

where $L^2(\tau_\Phi)$ is the spread of the carriers when the lattice begins scattering them. Notice the proximity between the formulas for $L^2(\tau_\Phi)$ and L_{LOC}^2. In our study, we find that we always have $L^2(\tau_\Phi) \simeq L_{LOC}^2$ for realistic scenarios. When μ_{LD} dominates, the physical picture is that the wave spreads and then saturate at $L^2(\phi)$, and then starts a new coherent propagation beyond τ_ϕ.

We also get the expression for the conductivity $\sigma_s(\omega)$, which is, in the limit $\tau_\phi \to \infty$:

$$\sigma_s(\omega) = ne^2 \frac{tanh(\beta\hbar\omega/2)}{\hbar\omega/2}\left(\frac{C_C\tau_C}{\omega^2\tau_C^2+1} - \frac{C_B\tau_B}{\omega^2\tau_B^2+1}\right). \tag{4.50}$$

Also note that we always have $C_C\tau_C \geq C_B\tau_B$ and $\tau_C \leq \tau_B$, as such the conductivity is always positive. Again, using a finite τ_ϕ, the equations remain the same, only τ_B is rescaled.

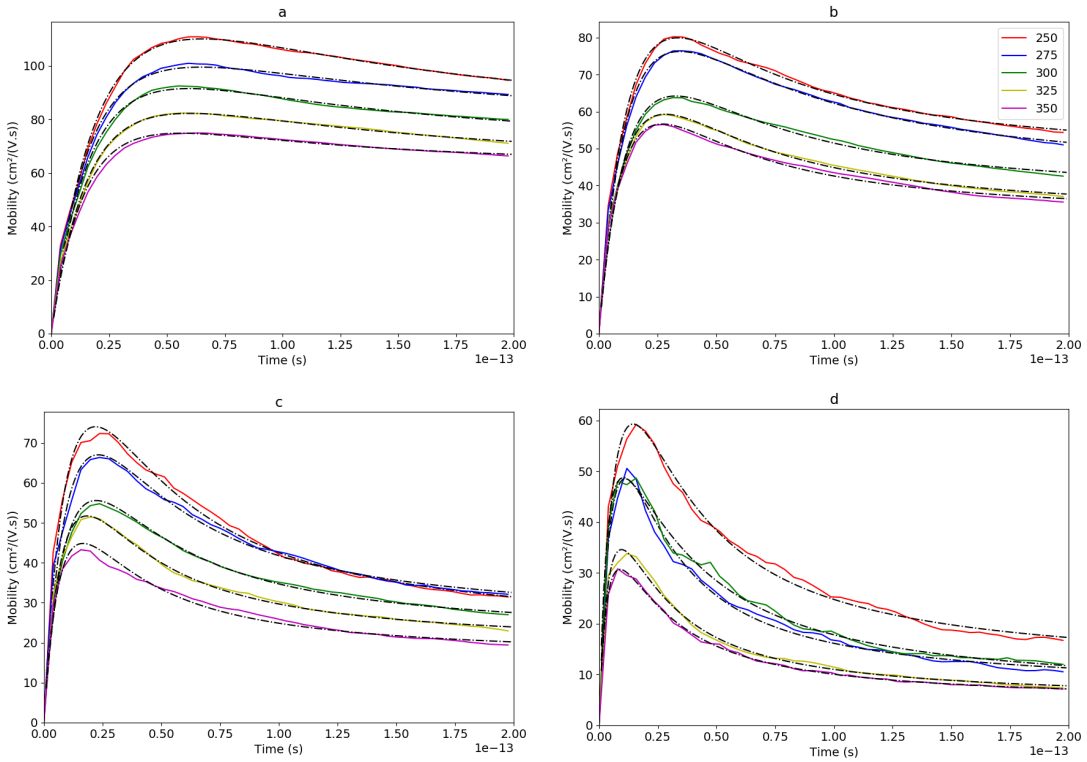

Figure 4.3: Average time dependent mobilities for different values of ω_{LO} and different temperature *(colored line)*, with the associated Drude-Anderson fits *(black dashed line)*. The parameters for ω_{LO} are **(a)** : $\omega_{LO} = 14meV$, **(b)** : $\omega_{LO} = 12meV$, **(c)** : $\omega_{LO} = 10meV$, **(d)** : $\omega_{LO} = 8meV$. We find that the fitted data are very close to the computed data, and allow us to extract the physical parameters of transport.

Even though the experimentally measurable mobility is not time dependent, we present results of mean squared displacement and conductivity in units of μ, and we define

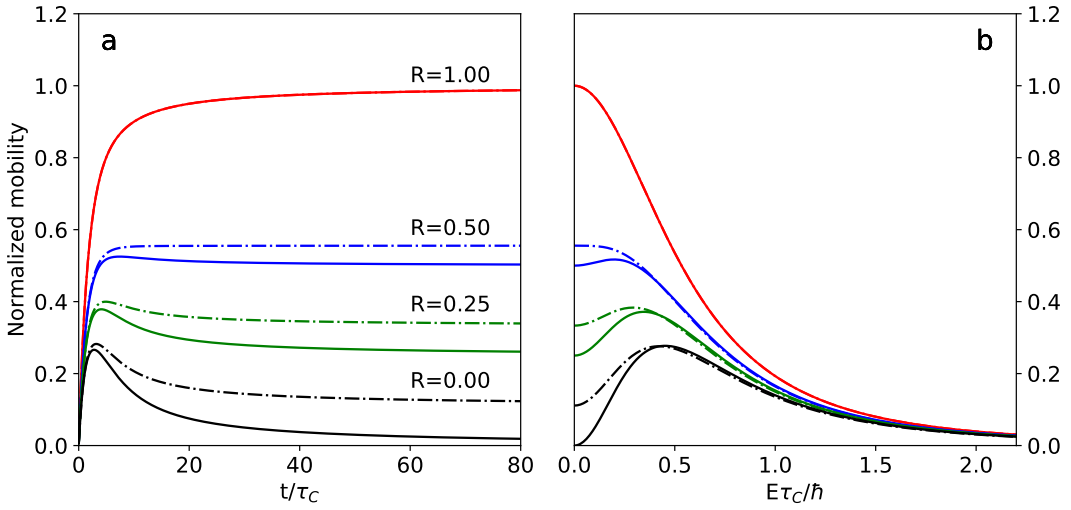

Figure 4.4: **(a)** Normalized time dependent mobility $\tilde{\mu}(t)/\mu_C$ and **(b)** normalized frequency dependent mobility $\tilde{\mu}(\omega)/\mu_C$ for different localization ratio $R = \mu_S/\mu_C$, with *(dashed line)* or without *(full line)* de-phasing process. Here $\tau_B = 2.5\tau_C$ and $\tau_\phi = 8\tau_B$.

$$\tilde{\mu}(t) = \frac{eX^2(t)}{2tk_bT}. \tag{4.51}$$

$\tilde{\mu}(t)$ is directly related to the computed $X^2(t)$, which is the quantity that we compute. We thus can fit our numerical data with this model and extract the physical parameters by comparison with equation 4.42. Results of diffusion for different intensity of disorder are shown in figure 4.3, which shows that this models fits the computed data accurately over the whole range of disorder and mobilities. We define also:

$$\tilde{\mu}(\omega) = \frac{\sigma(\omega)}{ne}. \tag{4.52}$$

These two mobilities and the static one μ are equal in the limits:

$$\mu = \lim_{t\to\infty} \tilde{\mu}(t) = \lim_{\omega\to 0} \tilde{\mu}(\omega). \tag{4.53}$$

Results of typical diffusion behaviour with different localization ratio R can be found in figure 4.4. This figure shows the link between the three mobilities

from equations 4.51, 4.52, and 4.53. It also shows that localization is not obvious when simply looking at the curves. Indeed the $R = 1$ and $R = 0.5$ curves look similar, and one needs access to the physical parameters of transport to analyse them properly. We see also that the Drude peak disappears when we reach low values of R. Such a behaviour occurs in some of our MAPI results in the case of strong disorder (see chapter 5).

We note here also that a standard model for studying localization effects, in the terahertz range, is the Drude-Smith model [12]. This model is a phenomenological model that is built upon the backscattering concepts, and is based on a formula for the terahertz conductivity, which is

$$\sigma(\omega) = \frac{ne^2\tau_{DS}}{m^*(1 - i\omega\tau_{DS})}\left[1 + \frac{c}{1 - i\omega\tau_{DS}}\right], \tag{4.54}$$

Where τ_{DS} is the Drude-Smith scattering time and c is the localization parameter. In the case where $c = 0$, this formula is the same as the originial Drude formula. The link between this model and the quantities we compute, the mean squared displacement and the velocity self correlation function, is however not immediate. For this reason we prefer the Drude-Anderson model.

4.6 Conclusion

To conclude we built the Drude-Anderson model, which is a phenomenological improvement of the semi-classical Drude model. It is based on a modelling of the quantum velocity correlation function, in which we take into account backscattering and dephasing effects.

Let us emphasize that this model has been essential for us in order to extract significant parameters from our calculations of time dependent quantum diffusion. It simplified computation of the conductivity, by giving to it an analytical form , and allowed us to understand in detail the physics of the model.

Bibliography

[1] P. Drude, "Zur elektronentheorie der metalle," *Annalen der Physik*, vol. 306, no. 3, pp. 566–613, 1900.

[2] P. Drude, "Zur elektronentheorie der metalle; ii. teil. galvanomagnetische und thermomagnetische effecte," *Annalen der Physik*, vol. 308, no. 11, pp. 369–402, 1900.

[3] F. Bloch, "Über die quantenmechanik der elektronen in kristallgittern," *Zeitschrift für Physik*, vol. 52, pp. 555–600, Jul 1929.

[4] P. W. Anderson, "Absence of diffusion in certain random lattices," *Phys. Rev.*, vol. 109, pp. 1492–1505, Mar 1958.

[5] P. A. Lee and T. V. Ramakrishnan, "Disordered electronic systems," *Rev. Mod. Phys.*, vol. 57, pp. 287–337, Apr 1985.

[6] B. Kramer and A. MacKinnon, "Localization: theory and experiment," *Reports on Progress in Physics*, vol. 56, pp. 1469–1564, dec 1993.

[7] J. M. Frost, L. D. Whalley, and A. Walsh, "Slow cooling of hot polarons in halide perovskite solar cells," *ACS Energy Letters*, vol. 2, no. 12, pp. 2647–2652, 2017. PMID: 29250603.

[8] C. Wolf, H. Cho, Y.-H. Kim, and T.-W. Lee, "Polaronic charge carrier–lattice interactions in lead halide perovskites," *ChemSusChem*, vol. 10, no. 19, pp. 3705–3711, 2017.

[9] R. Kubo, "Statistical-mechanical theory of irreversible processes. i. general theory and simple applications to magnetic and conduction problems," *Journal of the Physical Society of Japan*, vol. 12, no. 6, pp. 570–586, 1957.

[10] D. A. Greenwood, "The boltzmann equation in the theory of electrical conduction in metals," *Proceedings of the Physical Society*, vol. 71, pp. 585–596, apr 1958.

[11] S. Fratini, S. Ciuchi, and D. Mayou, "Phenomenological model for charge dynamics and optical response of disordered systems: Application to organic semiconductors," *Physical Review B*, vol. 89, 02 2014.

[12] N. V. Smith, "Classical generalization of the drude formula for the optical conductivity," *Phys. Rev. B*, vol. 64, p. 155106, Sep 2001.

Chapter 5

Electronic properties of $MAPbI_3$ above the Debye temperature

Contents

5.1 Introduction

In this chapter we analyze the electronic spectrum, the photoluminescence, the mobility and the terahertz conductivity of $MAPbI_3$. Our model from chapter 3 is expected to apply only above the Debye temperature, which is around 175K [1], and we restrict our study to the interval $250K \leq T \leq 350K$. We apply the tools presented in chapter 2 to the Hamiltonian build from chapter 3, and analyse the results for transport using the Drude-Anderson model from chapter 4. The

goal is to understand what phenomenon are important for electronic structure and quantum transport, as well as the optimal mobilities achievable above the Debye temperature, more specifically around room temperature.

We first present the effects of disorder on MAPI's electronic structure. We highlight the contribution of both diagonal and off-diagonal disorder on MAPI. We are able to compute photo-luminescence spectra as a function of temperature and to observe the evolution of the bandgap. We find that our model compares well with experimental data.

Then we show transport results for the three types of disorder, LO phonon, MA molecule, and off diagonal disorder, alone, and we show that LO phonon are by far the dominant disorder limiting the mobilities. We also show that the mobilities decrease with temperature in concordance with the phenomenological law $\mu(T) \propto T^{-3/2}$. It appears that at room temperature, transport should be looked at from a quantum point of view, as Boltzmann's theory of transport is unable to include quantum corrections linked to incipient localization.

From these results we also discuss the possibility of polaron formation in MAPI above the Debye temperature. Considering that the energy scattering of the LO phonon modes is larger than the polaron formation energy, it appears unlikely that such quasi-particle could be stable at room temperature. We then propose an alternative mode of transport, based on the delocalization of electron by lattice dynamics, which we call adiabatic quantum localization regime.

We end this chapter by a discussion of the fluctuating electrical potential (FEP) generated by the LO phonons. We analyse the characteristics of this FEP and its consequences on electrical properties.

5.2 Electronic spectrum and photo-luminescence

The density of states of the system is the first quantity that we analyse. When looking at the difference between the density of states without and with disorder, it appears that the disordered DOS is smoother than the perfect one. Notably the spikes at -2eV, corresponding to weakly interacting p orbitals of iodine, are greatly broadened by disorder. This implies a mixing and widening of all the eigenstates of the perfect system. Despite this, the band edges appear to be at the

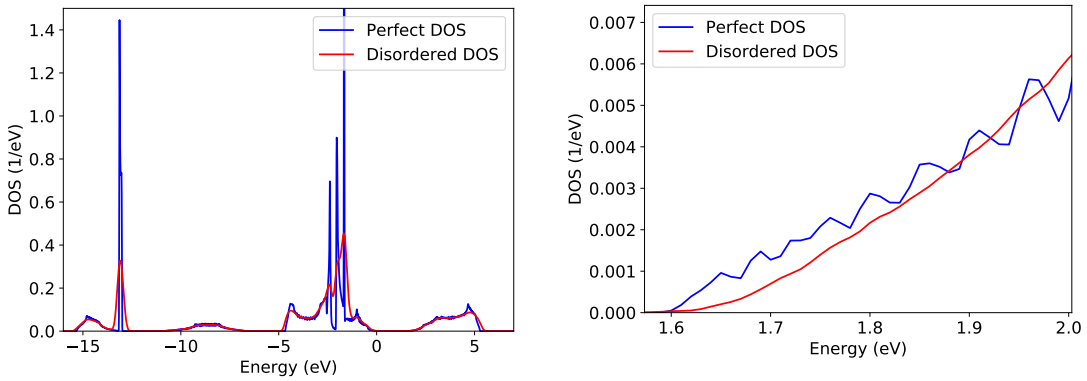

Figure 5.1: Left: Density of states as a function of energy, without disorder *(blue)* and with disorder *(red)*. Right: Density of states as a function of energy near the conduction band edge, with and without disorder. The difference in behaviour near the band edges indicates that the disordered DOS does not follow the standard behaviour of free electrons.

same energies, and the bandgap appears weakly modified. Yet, we can see that the behaviour of the DOS near the band-edges is not the same, indicating that the dispersion relation which is generally assumed of:

$$E(\vec{k}) = \frac{\hbar^2 k^2}{2m^*}, \tag{5.1}$$

where m^* is the renormalized electronic mass, is no longer valid for the disordered system. As such the renormalized mass appears ill-defined in our case when disorder is present.

In our disordered sample the determination of the bandgap from the electronic spectrum is also not as simple as it might seem. Because of the potential fluctuations, some states form the calence band and the conduction band are pushed into the bandgap. Yet because of the spatial coherence of the potential, theses states are unlikely to be in the same crystalline region.

As such the bandgap one would observe simply by looking at the eigenstates of the system, is not the same as one would observe experimentally, via absorption or photo-luminescence for example.

We need to look at thermodynamic averages over the density of states for results comparable to experiments. This is the case in particular for the measures

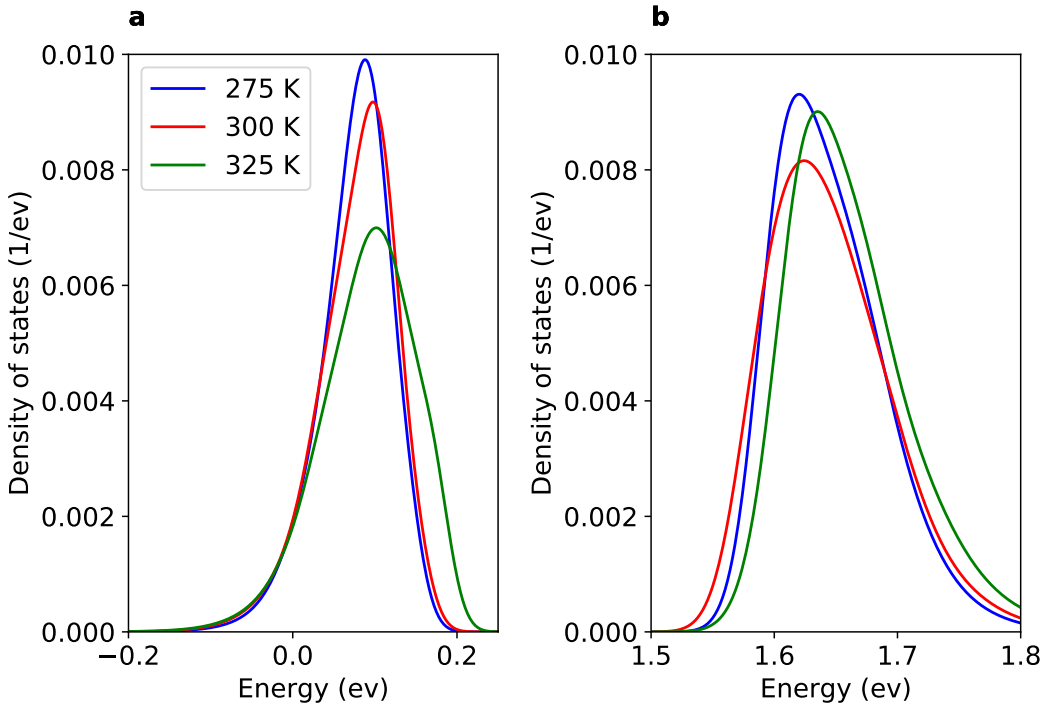

Figure 5.2: Occupation of the density of states as a function of energy for holes **(a)** and electrons **(b)** at different temperatures, for $\omega_{LO} = 12meV$.

of photoluminescence, mobility and terahertz conductivity that are analysed in this chapter. The thermodynamic density of states is defined as

$$n_{h,th}(E) = \frac{n(E)e^{\beta(E)}}{\int_{-\infty}^{E_0} n(E)e^{\beta(E)}dE}, \tag{5.2}$$

for holes in the valence band, and

$$n_{el,th}(E) = \frac{n(E)e^{-\beta(E)}}{\int_{E_0}^{\infty} n(E)e^{-\beta(E)}dE}, \tag{5.3}$$

for electrons in the conduction band. Here $\beta = 1/k_bT$ and E_0 is a reference energy, which lies in the bandgap. The exact value of E_0 is not important to us, provided that it is far from the band edges. This is due to the fact that it lies in a region where $n(E) = 0$, and has no impact on the normalized occupation. It can be seen on figure 5.2 that the occupied states are over a range of $\simeq 0.3eV$, and

that the occupied density of states is not maximal directly at the band edges.

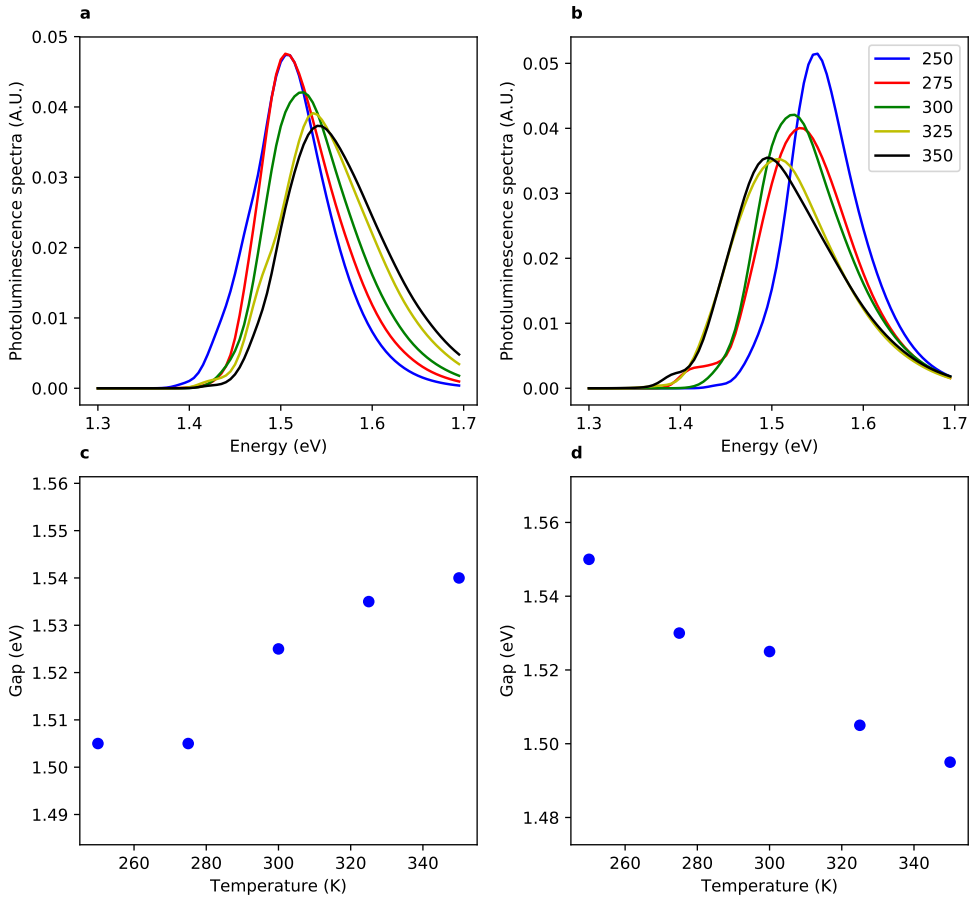

Figure 5.3: Variation of the photo-luminescence spectra with fixed diagonal disorder and increasing off-diagonal disorder **(a)** and fixed off-diagonal disorder and increasing diagonal disorder **(b)** as a function of energy. The maximum of intensities, corresponding to the bandgaps, are plotted as a function of temperature for both scenarios **(c)** and **(d)**. These results are for $\omega_{LO} = 12meV$.

Photo-luminescence is the photon spectrum emitted by a material when excited carriers recombine. To compute this spectra, which will serve as measurement for the bandgap, we need to compute the probability for a state to transfer to another, depending on the energy of the emitted photon. This is done using Fermi's golden rule, which gives us that the flux of energy resulting from the recombination of states at energy E to states at energy $E - \hbar\omega$ is:

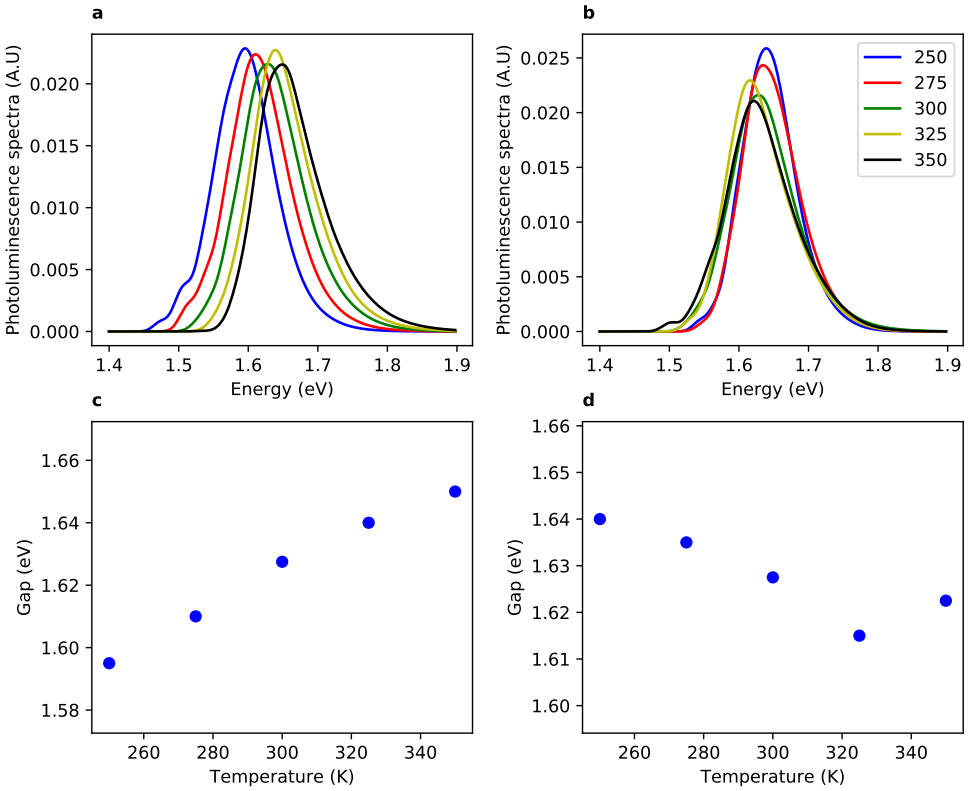

Figure 5.4: Variation of the photo-luminescence spectra with fixed diagonal disorder and increasing off-diagonal disorder **(a)** and fixed off-diagonal disorder and increasing diagonal disorder **(b)** as a function of energy. The maximum of intensities, corresponding to the bandgaps, are plotted as a function of temperature for both scenarios **(c)** and **(d)**. These results are for $\omega_{LO} = 14meV$.

$$\Phi(E, \omega) = A n_{e,occ}(E) n_{h,occ}(E - \hbar\omega) p(\omega), \tag{5.4}$$

where A is a constant independent of E and ω, $n_{e,occ}$ is the density of states occupied by electrons in the conduction band and $n_{h,occ}$ is the density of states of holes in the valence band, and $p(\omega)$ is the transition probability, which is

$$p(\omega) \propto \left|\langle \psi(E)|V_x|\psi(E - \hbar\omega)\rangle\right|^2 n(\omega). \tag{5.5}$$

In principle, the density of electromagnetic modes $n(\omega)$ comes into account, but is constant over our energy range. We define

$$\Phi(E,\omega) = BF(E, E-\hbar\omega)e^{-\beta\hbar\omega}, \tag{5.6}$$

where

$$F(E,E') = Tr[V_x\delta(E-H)V_x\delta(E'-H)], \tag{5.7}$$

where $F(E,E')$ is the probability of transition, according to the density of states, between states at energy E and E', and with V_x is the velocity operator. We take E to be energies in the valence band, while $E' = E+\hbar\omega$ is an energy in the conduction band. Then the normalized thermal photo-luminescence spectra is simply

$$\alpha(\hbar\omega) = \frac{e^{-\beta\hbar\omega}F(E,E+\hbar\omega)}{\int_0^\infty e^{-\beta\hbar\omega}F(E,E+\hbar\omega)dE}. \tag{5.8}$$

To obtain a filtered state of energy E from a random phase state spanning over the whole spectrum, we first compute the tridiagonal Hamiltonian using the recursion method over the random phase state, and diagonalize it (see chapter 2). Here, inelastic scattering induces a widening of the eigenstates of 10 to 15 meV, which we are able to consider using Gaussian widening of the eigenstates.

This gives us a series of eigenvalues E_n and eigenvectors v_n of the tridiagonal Hamiltonian. Because the eigenstates have non zero width, a few thousand recursion steps are required in order for them to have widths smaller than $10mev$. This means our energy resolution if of the order of 5 to 10 meV.

Results of photo-luminescence and bandgap variations are shown in figures 5.3, 5.4 and 5.5. In these figures we show the variations of photo-luminescence spectra by varying off-diagonal and diagonal disorders separately, and for different values of ω_{LO} (12 and $14meV$). The disorder of reference is that for $T = 300K$. When we set the diagonal or off-diagonal disorder as constant, we give it its value at $300K$. Then we look at this bandgap variation when both disorders are combined.

One of MAPI's interesting properties is it's surprising resistance to defects and processing method. This resilience to disorder seems also to appear in our results. Indeed, despite potential variations of a few tenth of eV in the crystal and high variation in inter atomic coupling, MAPI's bandgap remains mostly unchanged.

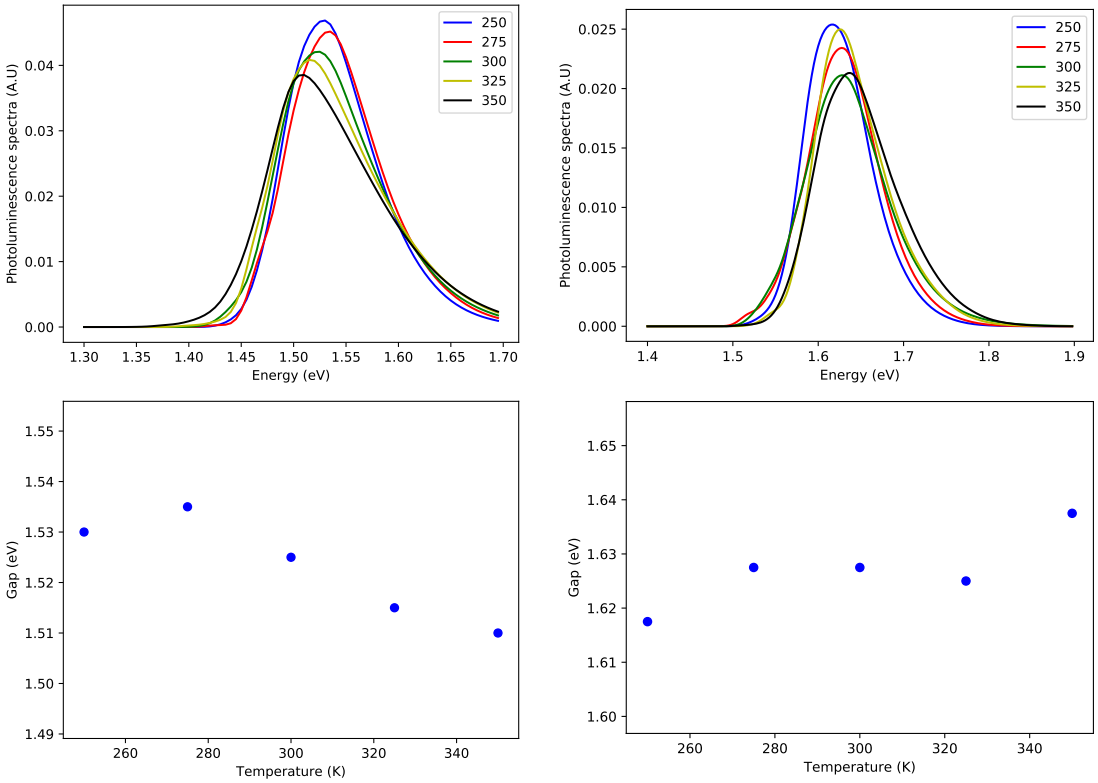

Figure 5.5: Top panels : Variation of the photo-luminescence spectra for different temperature as a function of energy. Bottom panels : maximum of intensities, corresponding to the bandgaps, plotted as a function of temperature. The results on the left are for $\omega_{LO} = 12meV$ while those on the right are for $\omega_{LO} = 14meV$.

The diagonal disorder has for effect to reduce the bandgap, by having states leak inside the forbidden zone, as is expected for such disorder. The off-diagonal disorder on the other hand has a less obvious effect, as it tend to increase the bandgap. This is due to the anti-bonding nature of the P orbitals of iodine and lead, between which lies the gap. This properties means that the stronger the coupling between these orbitals, the more their energy levels are repelled, and the more the bandgap increases. A similar phenomenon has been observed with tilting of the perovskite octahedrons [2], which has a the same effect on the electronic structure, and we believe the underlying causes to be the same.

At room temperature and for ω_{LO} between 12 and $14meV$, the two disorders actually compensate each other and the bandgap remains around the perfect value

of 1.6eV.

The experimental behaviour observed for MAPI is an increase of the bandgap with the temperature [3, 4]. This increase is of approximately $40meV/100K$. Half of it is caused by the thermal expansion of the lattice, and the other half is caused by the thermal disorder on the atomic position. As we do not account for thermal expansion, we only expect to see half of this variation, *i.e.* around $20meV/100K$.

What we observe is indeed a tendency for off-diagonal disorder to increase the bandgap of around $40 - 50meV/100K$, independently of the value of ω_{LO}, while the diagonal disorder decreases it of around $50meV/100K$ for $\omega_{LO} = 12meV$, or by $20meV/100K$ for $\omega_{LO} = 14meV$. When both disorders are allowed to vary together, their effects tend to compensate each other, and the variations are much lower. However, we are still able observe to observe a small decrease of $20meV/100K$ for $\omega_{LO} = 12meV$, and an increase of $20meV/100K$ for $\omega_{LO} = 14meV$. For these parameters, at $300K$, the bangap is between 1.52 and 1.63eV. These values are coherent with experimental results and comfort us in our idea that the most realistic parameter for ω_{LO} lies in the 12 to 14 meV range.

5.3 Dominant scattering by the LO phonons

We first show results of diffusion with no LO phonons. Indeed, it has been speculated that either the MA molecules or the lowest frequency (acoustic) phonons could be the limiting factors for diffusion in MAPI. We present results for these two disorders in figure 5.6. When looking at LO phonons and MA molecules, one need to consider the characteristic times of these phenomenon. The LO phonon motion happens on time constants of $0.5ps$, while the MA molecules have much bigger time constant, of around $10ps$. As such the MA molecules are screened by the phonons, and the dielectric permittivity associated is expected to be much bigger than 6, up to 25.

For the MA molecules, we present results with the scenario $\epsilon_r = 6$. We find that, in this limit, MA molecule limit mobilities to around $200cm^2/(V.s)$. The off-diagonal disorder seems to barely have any effect, and the scattering time appears to be very high ($\tau > 4.10^{-13}s$).

Therefore we conclude that the scattering by MA molecule or off diagonal dis-

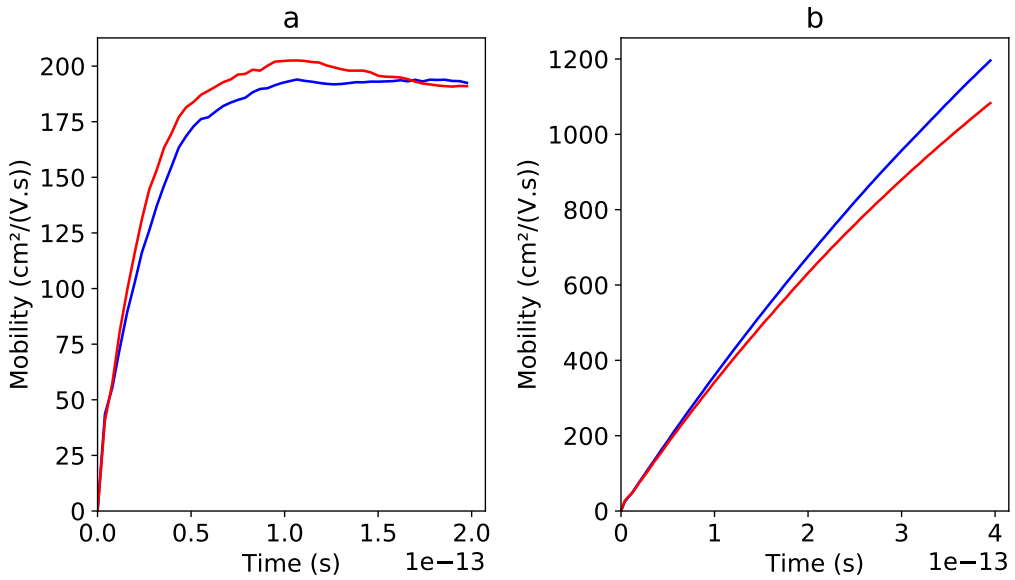

Figure 5.6: **(a)** Thermodynamically averaged mobilities as function time for samples containing only MA disorder, with $\epsilon_r = 6$, for holes *(red)* and electrons *(blue)*. **(b)** Thermodynamically averaged mobilities as function time for samples containing only off diagonal disorder, for holes *(red)* and electrons *(blue)*.

order alone lead to high mobilities compared to experimentally measured values. These values are much higher than what we find with LO phonons. Furthermore, the value $\epsilon_r = 6$ for the MA molecules is probably unrealistic, and the actual scattering is expected to be much lower. As such, MA disorder appears negligible for charge transport and we neglect it in the rest of the study. While off-diagonal disorder also has a very small effect on mobilities, its impact on the electronic structure is significant, and needs to be included (see previous results on photoluminescence).

Here we present results of diffusion in figure 5.7, in which we do not consider the disorder added by the MA molecules, and set the temperature of off-diagonal disorder to $300K$. We show 4 different values of LO phonon energy ω_{LO}. Let us recall that we expect the most realistic value of ω_{LO} is between 12 and $14meV$. The values of $\omega_{LO} < 12meV$ are not realistic values for intrinsic disorder, but we use them to simulate an increase of disorder due to extrinsic disorder, such as defects or chemical alloying. As a reminder, we have only one parameter for the

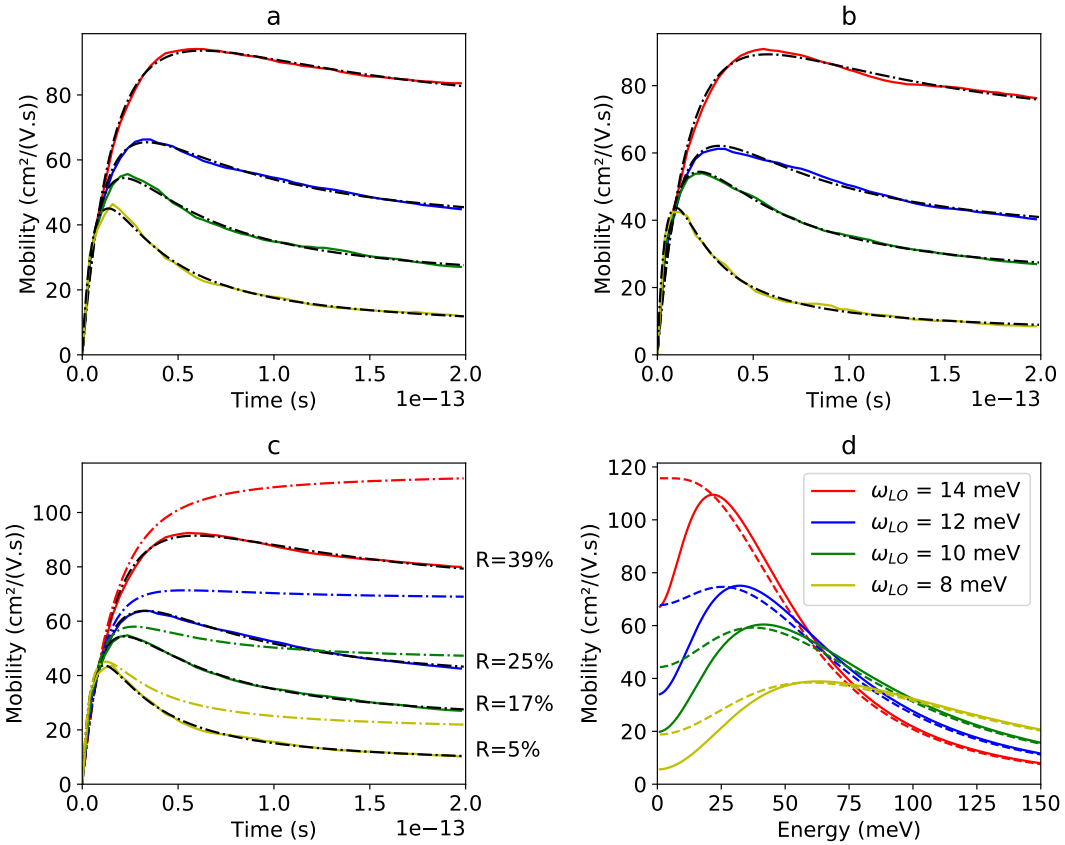

Figure 5.7: Thermodynamically averaged mobilities (at $T = 300K$) as a function time for different values of ω_{LO}, for holes **(a)**, electrons **(b)**, and averaged over both types of carrier **(c)**. The data *(coloured full line)* are fitted using the Drude-Anderson model *(black dashed line)*. We derive from the fitted parameter the localisation ratio R and the mobilities with a de-phasing time $\tau_\phi = 1/\omega_{LO}$ *(coloured dotted line)*. We also compute from the parameters the static and dynamic mobility as a function energy **(d)**.

intensity of disorder caused by the LO phonon, which is

$$W = \frac{\sqrt{k_b T}}{\epsilon_r \omega_{LO}}, \tag{5.9}$$

with $\epsilon_r = 6$. We find that the Drude-Anderson model fits the numerical data very accurately, and this gives a deeper understanding of the phenomenon behind transport in MAPI. This allows us to derive parameters, such as the different

ω_{LO} (meV)	C_c $(10^{11}m^2/s^2)$	τ_c (fs)	C_B $(10^{11}m^2/s^2)$	τ_B (fs)	Mean free path (Å)	R (%)	τ_ϕ (fs)
14	0.81	10.85	0.13	42.34	16.84	39.18	47
12	0.95	7.23	0.18	28.59	11.82	25.47	55
10	1.18	5.20	0.23	22.01	9.37	16.73	66
8	1.77	3.01	0.39	12.92	6.54	5.41	83

Table 5.1: Drude-Anderson parameters obtained for the different values of ω_{LO} studied, at $T = 300K$. The mean free path, which are defined from equation 4.43, are of the order of 1 to 2 nm.

scattering times, and to extrapolate the effects of dephasing at long time. The LO phonon modes seem to limit mobilities in MAPI to values of $100cm^2/(V.s)$, which is consistent with previous studies that found these phonon to be the main source of charge carrier scattering [5].

However, we find strong quantum localization effects that cannot be neglected, with a localization factor R ranging from 39 to 25%, even for the best samples. These localization effects are out of reach of the standard Drude theory of transport. The case $\omega_{LO} = 8meV$, which corresponds to a 100% increase in potential disorder compared to $\omega_{LO} = 12meV$, shows that the mobility is divided by 4. The residual mobility is very small, and a very large portion of the charge carriers are localized on very short time-scales, compared to the phonon period (see Table 5.1).

As such we want to insist on the fact that backscattering effects and localization phenomena are at the heart of transport in MAPI, and are not accessible to semi-classical theories of transport. We also want to point out that, while the LO phonon seem to limit the mobilities in MAPI to values of around $100cm^2/V.s$, a small amount of additional disorder is able to quickly bring these values down to practically perfect localization.

Still, we can see that when we account for the dephasing effect caused by the lattice dynamic, mobilities increase. This is an important effect even for the less disordered samples ($12meV < \omega_{LO} < 14meV$), where the mobilities are increased by a factor of 1.5 to 2. This effect becomes even more important as disorder increases. Indeed for highly disordered systems ($\omega_{LO} < 12meV$), the increase of mobility due to dephasing is the main contribution to the total mobility. This is very important as even seemingly insulating samples exhibit residual conductivity

thanks to this dephasing. This prompts us to propose a model of diffusion, where electrons localize rapidly in the lattice, but are then delocalized by the lattice dynamics, which allows conduction. This model is detailed more in section 5.5.

Finally we point to the fact that the optical conductivity is a very interesting experimentally measurable marker of time dependent charge carrier transport. We find that for large $\omega_{LO} \geq 12meV$ the Drude peak is weakly modified by localization effects, if inelastic scattering is taken into account. Yet for smaller ω_{LO} values, ad dip appears that could be observed experimentally.

$$\boldsymbol{\omega_{LO} = 14meV}, \boldsymbol{\tau_\phi = 47fs}$$

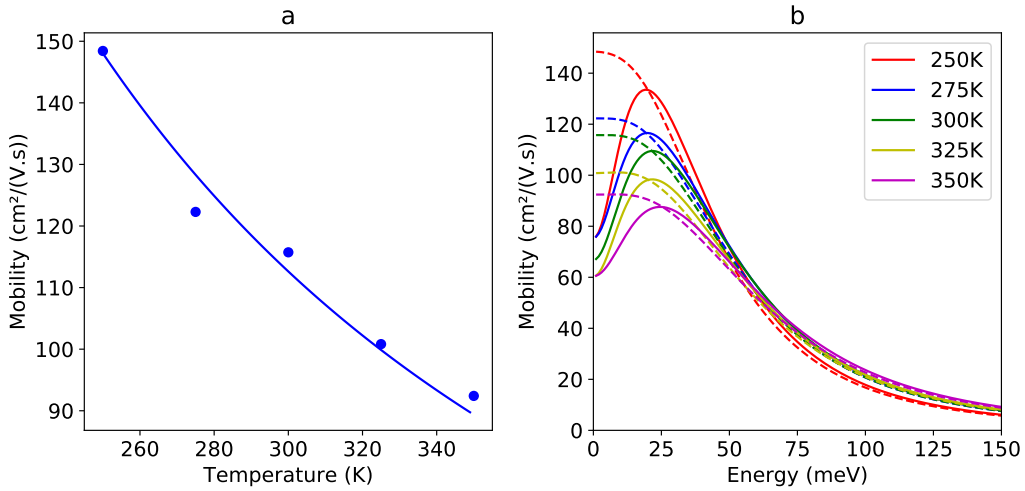

c

T (K)	C_c $(10^{11}m^2/s^2)$	τ_c (fs)	C_B $(10^{11}m^2/s^2)$	τ_B (fs)	Mean free path (Å)	R (%)
250	0.73	13.15	0.14	46.53	18.90	33.81
275	0.76	10.44	0.09	48.53	16.13	44.93
300	0.81	10.85	0.13	42.34	16.84	39.18
325	0.79	10.12	0.10	45.99	15.80	42.29
350	0.87	9.48	0.14	34.10	15.25	44.17

Figure 5.8: Results for $\omega_{LO} = 14meV$ and $\epsilon_r = 6$. **(a)** : Thermodynamically averaged mobilities as function of temperature. The data *(blue dots)* are shown with a de-phasing time $\tau_\phi = 1/\omega_{LO}$, and fitted via a power law in $T^{-3/2}$. We derive from the parameters the static and dynamic mobility as function energy **(b)**, with and without dephasing. The fitted parameters are shown in **(c)**.

$$\omega_{LO} = 12meV, \tau_\phi = 55fs$$

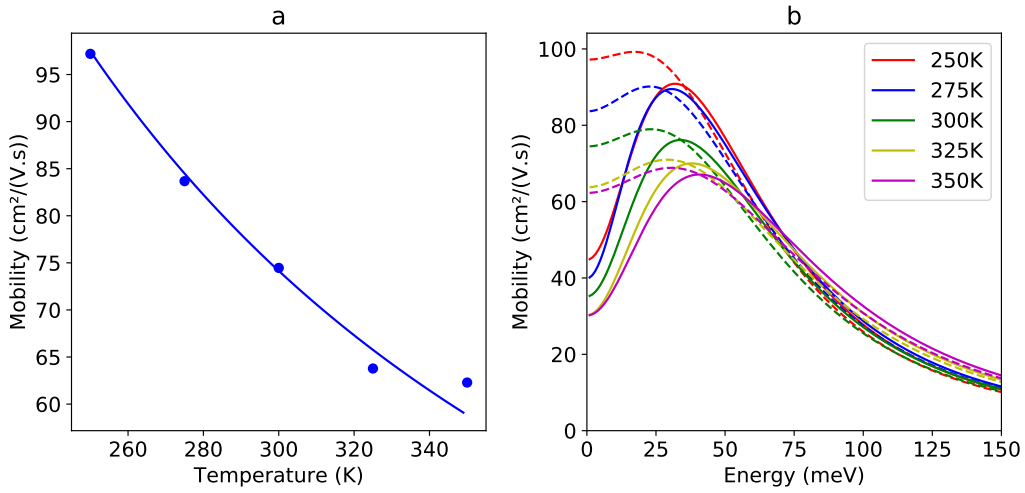

c

T (K)	C_c $(10^{11}m^2/s^2)$	τ_c (fs)	C_B $(10^{11}m^2/s^2)$	τ_B (fs)	Mean free path (Å)	R (%)
250	1.09	8.94	0.35	22.32	14.08	19.73
275	1.00	7.94	0.21	28.83	13.09	23.85
300	1.04	8.37	0.30	23.19	13.24	20.94
325	1.17	7.21	0.31	21.44	12.25	20.15
350	1.32	7.17	0.41	18.82	12.53	19.28

Figure 5.9: Results for $\omega_{LO} = 12meV$ and $\epsilon_r = 6$. **(a)** : Thermodynamically averaged mobilities as function of temperature. The data *(blue dots)* are shown with a de-phasing time $\tau_\phi = 1/\omega_{LO}$, and fitted via a power law in $T^{-3/2}$. We derive from the parameters the static and dynamic mobility as function energy **(b)**, with and without dephasing. The fitted parameters are shown in **(c)**.

5.4 Effect of temperature on transport properties

We now discuss results of mobility as a function temperature, presented in figure 5.8, figure 5.9, figure 5.10, and figure 5.11. We fix ω_{LO} at different values and vary the temperature.

Doing so implies a variation of both diagonal and off-diagonal disorder simultaneously. We have seen in section 5.2 that both phenomenon have inverse effect

$$\omega_{LO} = 10meV,\ \tau_\phi = 66fs$$

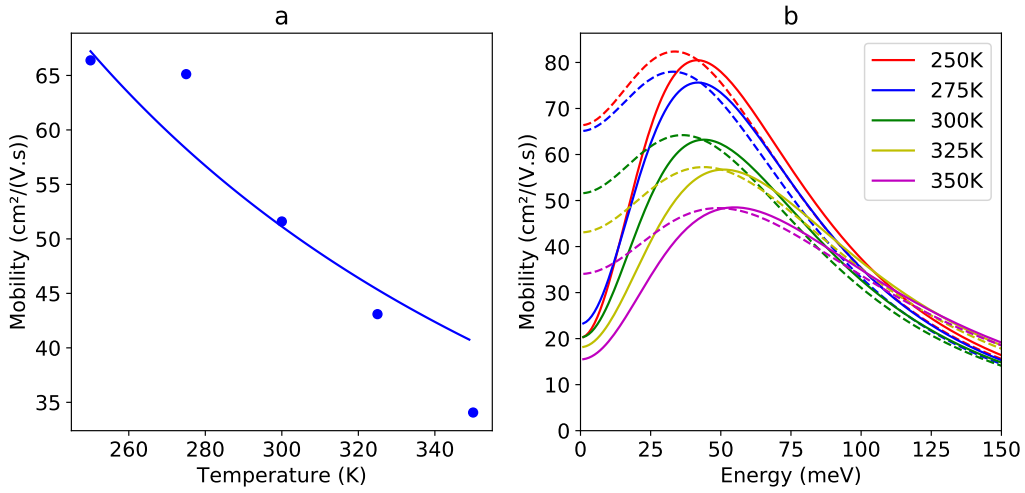

c

T (K)	C_c $(10^{11}m^2/s^2)$	τ_c (fs)	C_B $(10^{11}m^2/s^2)$	τ_B (fs)	Mean free path (Å)	R (%)
250	1.49	6.86	0.53	17.83	12.22	8.50
275	1.47	7.25	0.55	17.35	12.57	10.31
300	1.34	6.67	0.46	17.05	11.36	11.70
325	1.60	5.47	0.53	14.55	10.30	11.58
350	1.57	4.62	0.44	14.30	8.99	12.90

Figure 5.10: Results for $\omega_{LO} = 10meV$ and $\epsilon_r = 6$. **(a)** : Thermodynamically averaged mobilities as function of temperature. The data *(blue dots)* are shown with a de-phasing time $\tau_\phi = 1/\omega_{LO}$, and fitted via a power law in $T^{-3/2}$. We derive from the parameters the static and dynamic mobility as function energy **(b)**, with and without dephasing. The fitted parameters are shown in **(c)**.

on the bandgap, and tend to compensate at room temperature, depending on the value of ω_{LO}. However this doesn't hold for impact on mobilities, where off diagonal disorder seems to have very little effect compared to diagonal disorder. The most often cited law for variation of mobility as a function of temperature predicts

$$\mu \propto T^{-3/2}. \tag{5.10}$$

This law appears to be well obeyed in our study for $\omega_{LO} \geq 12meV$, but be-

$$\omega_{LO} = 8meV,\ \tau_\phi = 83fs$$

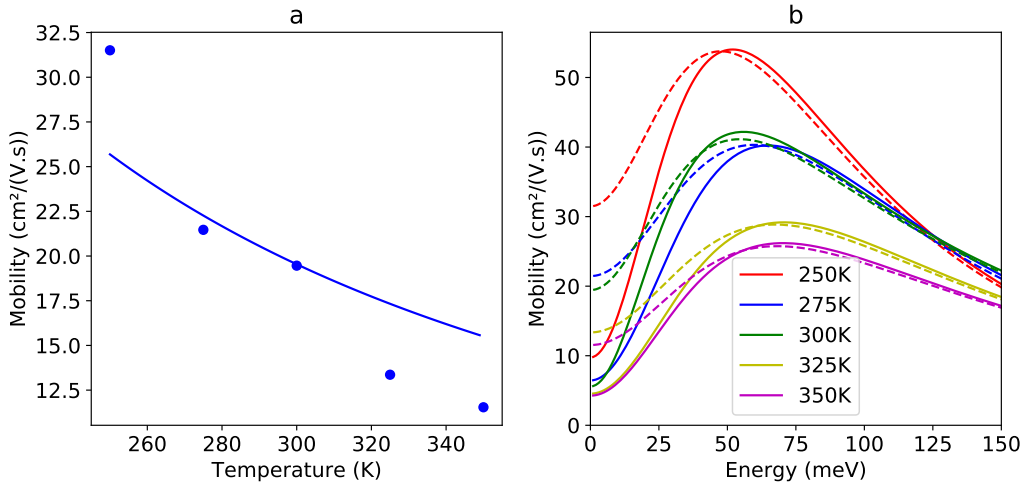

c

T (K)	C_c $(10^{11}m^2/s^2)$	τ_c (fs)	C_B $(10^{11}m^2/s^2)$	τ_B (fs)	Mean free path (Å)	R (%)
250	1.61	4.07	0.41	14.94	8.18	6.42
275	1.92	3.29	0.54	11.10	7.06	4.83
300	2.17	1.99	0.22	17.93	5.23	6.70
325	1.78	2.40	0.35	11.57	5.33	5.95
350	1.81	1.95	0.26	12.80	4.55	7.27

Figure 5.11: Results for $\omega_{LO} = 8meV$ and $\epsilon_r = 6$. **(a)** : Thermodynamically averaged mobilities as function of temperature. The data *(blue dots)* are shown with a de-phasing time $\tau_\phi = 1/\omega_{LO}$, and fitted via a power law in $T^{-3/2}$. We derive from the parameters the static and dynamic mobility as function energy **(b)**, with and without dephasing. The fitted parameters are shown in **(c)**.

comes gradually worse as ω_{LO} decreases. The observed decrease of mobility with temperature means that transport in MAPI is not thermally activated, in contrast with organic semiconductors, where thermal agitation allows electron hopping. Here we find that the $T^{-3/2}$ law is compatible with our model in the cases where localization effects are not too strong $R > 20\%$. This result is consistent with experimental measurements, and is often taken as an indication of standard band like transports. We however show that one can observe this behaviour in the presence of localization effects, that are not described by semi-classical theories.

In accordance with the smooth variation of the $T^{-3/2}$ law, the parameters of diffusion, τ_C, τ_B and the mean free path vary weakly with the temperature. In the present study, the variation of ω_{LO} has a larger effect. This is consistent with the parameter we have derived for the intensity of diagonal disorder, which is proportional to $\sqrt[k_BT]{}/\omega_{LO}$. Here the temperature varies of around 20% while ω_{LO} varies by almost a factor of two.

We also want to add that the value of the scattering time expected from a Drude model with $m^* = 0.15m_e$ and $\mu = 100cm^2/(V.s)$, is $\tau_C = 8fs$. Note that for cases where $\tau_C = 8fs$, we have static mobility of $40cm^2/(V.s)$ due to strong localisation effects. Yet, when the dephasing effect is taken into account, it kills the localisation and we have computed mobilities of $80cm^2/(V.s)$, which is comparable with the Drude result. Quite generally, for moderate localization ratio $R > 20\%$ ($\omega_{LO} > 12meV$), we find that the dephasing effect tends to kill most of the effect of backscattering, and we recover results close to the simple Drude model. On the contrary, when R is smaller, even in the presence of dephasing effects, the values are very different from those of the Drude model.

5.5 The adiabatic quantum localization regime

In this section we discuss in more details the mechanism for diffusion at low R values. We recall first why we neglect the polaronic effect and discuss the adiabatic quantum localization regime for small $R < 20\%$.

A polaron is a quasiparticle where the atoms are displaced from their equilibrium positions by the charged electron. As the electron moves, the lattice deforms around it accordingly, and the polaron can be seen as an electron surrounded by a phonon cloud. This effect lowers the electron mobility and increases it's effective mass. The formation energy of such polaron is given by

$$E_{pol} \simeq \alpha\hbar\omega_{LO} \simeq 30meV, \tag{5.11}$$

with the coupling constant $\alpha \simeq 2 - 3$ [6, 7]. However our results indicate that the large polaron is not stable at room temperature. Indeed above the Debye temperature (175K in MAPI), the phonon modes are thermally excited, which

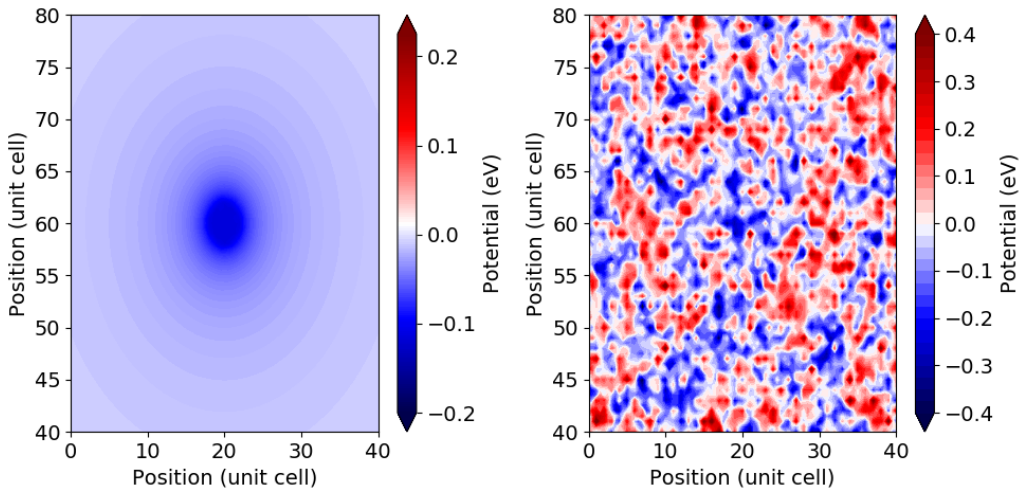

Figure 5.12: Intensity of the electrical disorder caused by LO phonons as function position for a planar cut inside a MAPI sample, with an electron in the center. The parameter for the disorder is with $\epsilon_r = 6$, $T = 0K$ *(left)* or $T = 300K$ *(right)* and $\omega_{LO} = 12meV$. The electron cloud is taken to have a radius of $\simeq 2$ unit cells, which is approximately the mean free path.

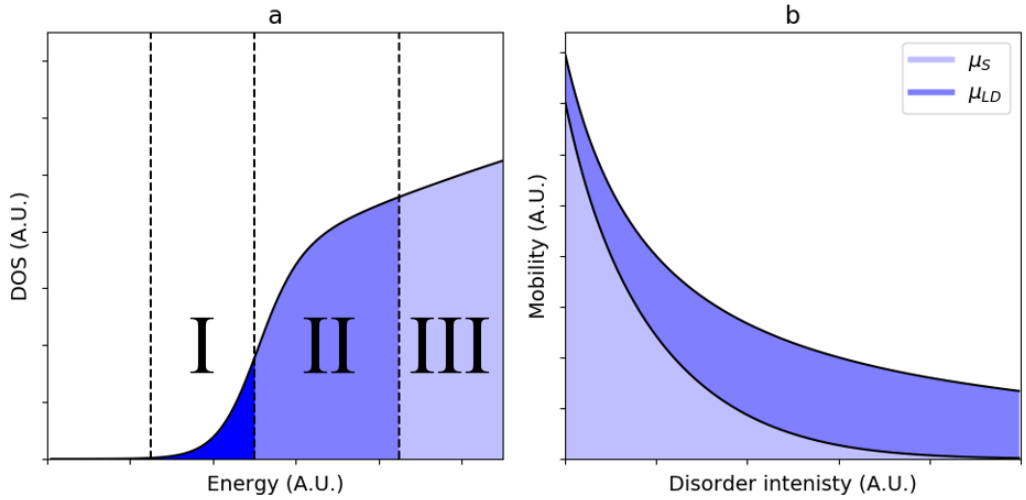

Figure 5.13: **(a)** Energy ranges where different transport mechanisms dominate. **I** : diffusion dominated by thermally activated hopping. **II** : diffusion is through the dephasing processes induced by the lattice dynamics. **III** : band-like diffusion. **(b)** Schematic representation of the evolution of the mobility $\mu = \mu_S + \mu_{LD}$ as a function of disorder. Static contribution μ_S *(light blue)* and lattice driven mobility μ_{LD} *(dark blue)* are shown.

induces a scattering of the electrons and a tendency to break the polaronic state. The scattering by thermal vibrations creates an energy broadening

$$\Delta E \simeq \frac{\hbar}{\tau}, \tag{5.12}$$

where τ is the electron lifetime. In our case, we have $\tau \leq \tau_C$. As such, even for the lowest disorder system where $\mu \simeq 100 cm^2/(V.s)$ with $\tau_C \simeq 10 fs$, we have $\Delta E \geq 70 meV$. Therefore the energy broadening due to thermal disorder is larger than the polaron energy. In addition, the large polaron theory assumes that the electron moves ballistically inside the large polaron radius, which is not what we find. Indeed the computed radius of such large polaron would be of 40-50 Å, which is twice larger than the mean free path that we predict, which is less than 20Å.

Therefore the results of our model indicate a situation in which the large polaron is not stable. Several experiments in the litterature have been interpreted as the evidence for large polaron existence [8, 9], and there is a strong belief in the community that large polaron exists even at room temperature. We believe that experiments pointing to evidence of large polaron could be interpreted by localization effects shown here.

There is of course an effect of the electron on the lattice, but this is not taken into account here. We show the comparison between the potential created by an electron and the total potential created by the lattice in figure 5.12. This shows that the potential of the electron is rapidly smaller than the internal field due to thermal disorder.

We discuss now the adiabatic quantum localization scenario, in which the lattice dynamics, and the disordered potential, have a central role for the charge diffusion. In this scenario, the electron is essentially localized if the lattice is static, but can diffuse thanks to dephasing effect. This corresponds to the contibution μ_{LD} to the total mobility (see equation 4.49). This dephasing process corresponds to the so-called Thouless regime [10, 11, 12, 13, 14] that is theorized to occur near metal-insulator transition, and is also related to the concept of transient localization that has been proposed for crystalline organic semi-conductors, like rubrene [15, 16, 17, 18]. Because we always have $\tau_B < \tau_\phi$, the diffusion can be seen as a nearly adiabatic process where electrons localize before the atoms move

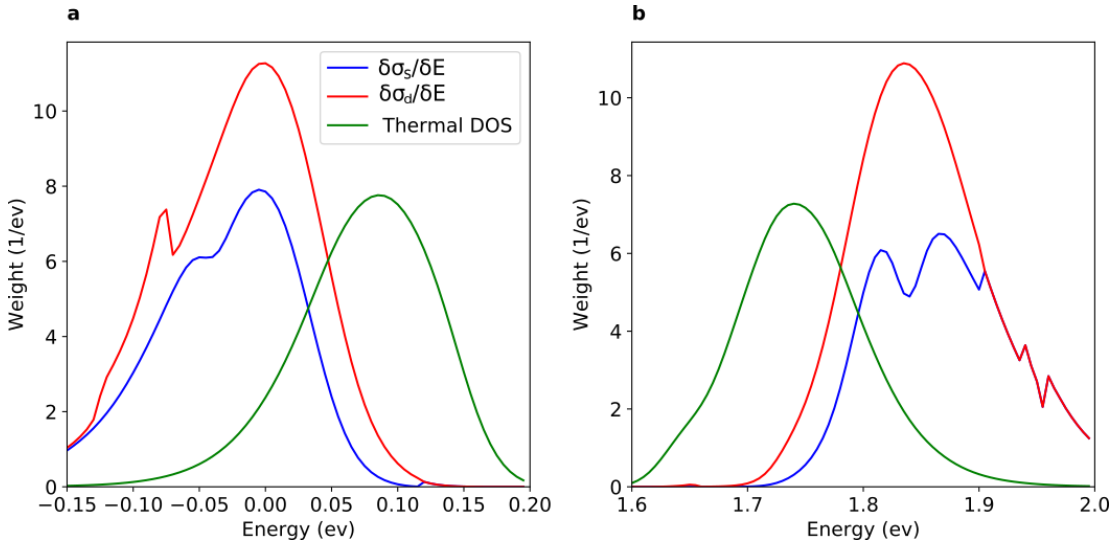

Figure 5.14: Thermal occupation of the density of states, differential static and dynamic conductivities, $\delta\sigma_s/\delta E$ and $\delta\sigma_d/\delta E$, as a function of energy, for hole **(a)** and electrons **(b)**, for $\omega_{LO} = 12meV$. The data is normalized to 1 over the energy spectrum.

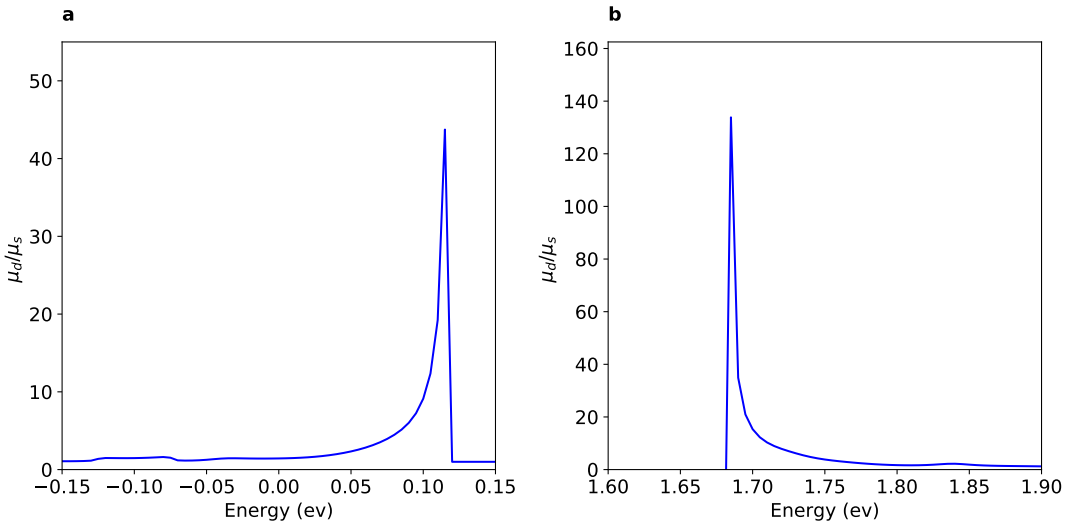

Figure 5.15: Ratio between the static, μ_s, and dynamic, μ_d, mobilities as a function of energy for holes **(a)** and electrons **(b)**, for $\omega_{LO} = 12meV$.

and change appreciably the electrostatic potential. Then the atoms move slowly, and the charge constantly adapts its wave function accordingly. This implies that the charges have a diffusion which is driven by the lattice dynamics, so that the diffusion coefficient is proportional to the LO phonon frequency.

As we have shown in section 5.3 lattice dynamics has a strong effect on the more disordered MAPI samples, and a weaker one in the less disordered cases. But, if we look at the differential conductivity, resolved in energy, as shown in figures 5.14 and 5.15, we see that the lattice dynamics affects the charge carriers near the band edges strongly even with $\omega_{LO} = 12meV$.

As such, it is also expected to happen in good MAPI samples, over a smaller energy range, near the band edges. The general view is that there always exists an energy region between the thermally activated regime, and the band like regime, which corresponds to this scenario. With increasing disorder, the size of this region increases and can even contain a large fraction of the carriers. Furthermore the contribution of lattice dynamics to the total mobility becomes higher as disorder increases. This is shown in figure 5.13.

To conclude, we believe this regime of diffusion, which we call adiabatic quantum localisation, to be more important in the most disordered MAPI samples, but is always present near the band edges. In fact for samples with mobilities below $30cm^2/(V.s)$, we find that this is the main way of diffusion.

5.6 The fluctuating electrical potential

In this section we discuss the characteristics of the strong inner potential that exists in MAPI. In the following we call it the fluctuating electrical potential (FEP). We summarize also its effects on the electronic properties as a function of temperature, and discuss briefly its possible effect for other electrical properties.

The three main characteristics of the FEP are:

- Its temporal fluctuations. They occur on a timescale which is the period of the LO phonons.
- Its spatial fluctuations. Since there is no length scale in the Coulomb interaction, the only length scale here is the lattice period. Indeed we observe

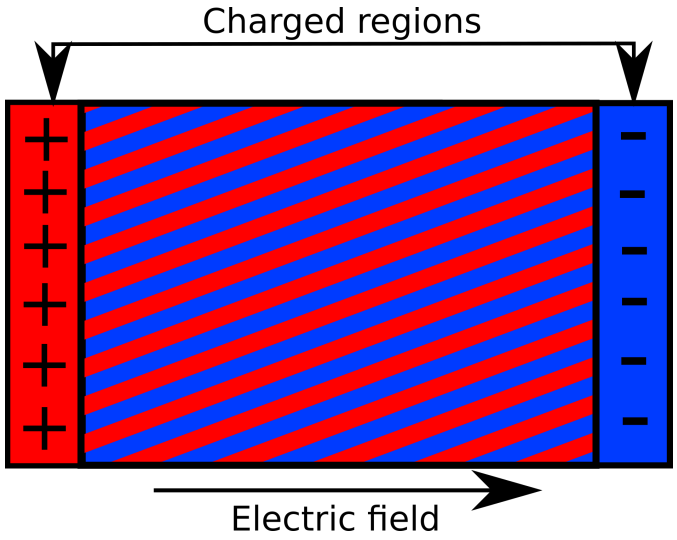

Figure 5.16: Schematic representation of a longitudinal plasmon. The positive charges are considered fixed, while the negative charges are mobile. The electric field is created between the charged region, as for a capacitor, and acts as a restoring force.

numerically that the FEP varies typically on distances of the order of few unit cells.

- It's amplitude. In our calculation, the maximum variation of the potential is of the order of $\pm 0.4eV$ per unit cell at room temperature.

In the present model the typical amplitude depends on the three types of parameters, which are the Born charges, the atomic masses, and the adaptable parameter ω_{LO}.

We discuss now the typical value of this amplitude, starting from a thermodynamic argument. It shows that this amplitude is in fact rather general and depends essentially on the temperature and the density of LO phonon modes. The argument is based on a simplified continuum model. In particular we do not discuss possible local field effects, and we consider that the electric field varies continuously from cell to cell. We present here preliminary results, which suggest that this approach can be fruitful.

We can illustrate it by considering charge oscillations in a simple capacitor. This represents the simplest example of a longitudinal charge oscillation (plasmon),

where all positive charges are fixed, and all negative charge are mobile, and move at the same velocity, as shown in figure 5.16.

In this model the energy is split only in kinetic energy and electrostatic energy. Therefore the total energy is

$$\frac{1}{2}Mv^2 + \frac{1}{2}\epsilon_0\epsilon_r E^2 V = cste, \tag{5.13}$$

where M is the total mass of the moving particles, E is the electric field, and V is the volume. Maxwell equations show that $E = -nqx/\epsilon_0\epsilon_r$, where n is the density of charge carriers, q is their charge, and x is their displacement. From this energetic approach the equation of motion can be derived and lead to the expression of the plasma frequency

$$\omega_p^2 = \frac{nq^2}{\epsilon_0\epsilon_r m}, \tag{5.14}$$

where m is the mass of the carriers. In MAPI, the Born charges are important only for motion along the Pb-I axis. Therefore if we neglect the motion of iodine perpendicular to the axis, we find that there is 1 LO mode per unit cell, with a typical frequency of about $10meV$. Here n is one per unit cell, q is the Born charge in the Pb-I direction $(4.42e)$, and m is the reduced mass of the lead iodine pair.

Starting from this energetic expression and using the equipartition theorem, we get that the average electrostatic potential energy per unit of volume is

$$\frac{1}{2}\epsilon_0\epsilon_r E^2 = \frac{N_m}{V}\frac{1}{2}k_B T f, \tag{5.15}$$

where $\frac{N_m}{V}$ is the number of modes per unit of volume, $\frac{1}{2}k_B T$ is the potential energy per mode, for $k_B T > \hbar\omega$, and f is the ratio between the potential electrostatic energy and the total potential energy. It is also the ratio between the restoring force of the electrostatic energy and the total restoring force. In order to have a large E^2, we need:

- $k_B T > \hbar\omega_{LO}$. If this is not the case, we expect exponentially small potential electrostatic energy, as the phonon modes are simply not excited. This is the case at room temperature for halide perovskite, but is not the case for many ionic semiconductors.

- We need also high values of Born charges to have a high f, that is a large contribution of the electrostatic restoring force, compared to the chemical force.

In general we expect that the acoustic and transverse optical modes will have a small f value, while, if the Born charges are high, the f value of the LO phonon could be close to one. In the end the electrostatic field depends only on the temperature and the density of optical modes per unit of volume. We compare now the expected value of this continuum model to our discrete model. Let us consider the typical potential variation of the potential V_c along one direction, across one unit cell. We have

$$V_c^2 = \frac{e^2 < E^2 > a^2}{3}, \tag{5.16}$$

where a is the size of the unit cell. We get from equation 5.15

$$V_c = \sqrt{k_B T 1Ry} \sqrt{\frac{4\pi}{3} \frac{N_u f 2 r_B}{\epsilon_r a}}, \tag{5.17}$$

where Ry is the Rydberg $13.6eV$, r_B is the Bohr radius ($\simeq 0.53$Å), and N_u is the number of modes per unit cell. If we take $\epsilon_r = 6$ and $T = 300K$, we get $|V_c| = 0.2eV\sqrt{N_u f}$. This prediction of the continuous model must be compared to the calculation done using the Einstein model, for which we get $|V_c| = 0.2eV.(11meV/\hbar\omega_{LO})$. Assuming that the stretching mode dominates ($N_u = 1$), the comparison implies that f is between 0.6 and 0.8, for ω_{LO} between 12 to 14 meV. Furthermore, since f is a ratio between the electrostatic restoring energy and the total restoring force, we get $f = (\omega_P/\omega_{LO})^2$, where ω_P is the plasmon frequency, and indeed, using equation 5.14, plasmon frequency is estimated to be around $10meV$. These results indicate that the continuous model provides us with a fruitful approach for discussing the FEP. We show in table 5.2 a short summary of MAPI's characteristics, depending on the temperature.

Finally we can expect that the FEP has other effects on electrical properties. We believe that it could play an important role in electron hole recombination. Indeed, because of the FEP electron and holes tend to explore different regions of space, which increase charge carriers lifetime and diffusion length. Furthermore

Below the Debye temperature	Above the Debye temperature
FEP $\simeq 0$	FEP $\simeq 0.4eV$
Good crystals	Disordered crystal
Large mobility [19]	Small mobility
Large polaronic state	Large polaronic state
stable	unstable
Well defined excitonic states	Strong localization effect

Table 5.2: Summary of some electronic characteristics of MAPI crystals depending on the temperature.

we suggest a connection of the FEP with the ferroelectricity observed in many ABO_3 materials. Indeed these materials have large Born charges, but their LO phonon energy are higher than the thermal energy. This could lead to ferroelectric domain but no fluctuating potential. On the other hand, other perovskites such as $MAPbBr_3$ have similar Born charges and LO phonon energies and we expect their FEP to be close to the one of MAPI. We also believe the FEP could influence the ionic diffusion.

5.7 Conclusion

In this section, we have first investigated the electronic properties of MAPI. We have highlighted two different behaviour, for diagonal and off diagonal disorder. From photo-luminescence simulations, we have been able to show that diagonal disorder tends to reduce the gap, while the off-diagonal disorder tends to increase it. For a LO phonon frequency ω_{lo} between 12 and 14meV, these phenomenon almost compensate each other, and the value of the bandgap is weakly modified. This shows the exceptional resistance of MAPI's band structure to disorder, and highlights the unusual phenomenon behind MAPI's increasing bandgap with temperature.

After this, we have shown the impact of the different disorders on charge carriers mobilities. We found that the MA molecules and the off-diagonal disorder had weak impact on them, and are not the limiting factors. Indeed, we found that the LO phonon are limiting the mobilities to around $100cm^2/V.s$, in reasonable agreement with experimental results. We were able to discuss the possibility of

large polaron formation in MAPI. From the diffusion results, and the parameters obtained thanks to the Drude-Anderson model, we are able to conclude that large polaron energy formation in MAPI is smaller than the LO phonon energy scattering. As such the polaronic states cannot exist at room temperature, and is not responsible for transport properties.

Furthermore we highlighted strong localization effects, which can not be interpreted semi-classically. These effects tend to reduces mobilities by 70% even in the less disordered cases, and can even completely localize electrons when extrinsic disorder is added. These effects can however be broken by the lattice dynamics, which modifies the potentials landscape and allows charge carrier to move with it. We propose a model of transport, close to the Thouless regime, where charge carriers are localized quickly in the material, and are then able to follow the lattice dynamics to diffuse. We call it the adiabatic quantum localization regime.

Finally we emphasize the role of the fluctuating electrical potential (FEP) in the material. Above the Debye temperature these fluctuations are strong ($\pm 0.4eV$). We suggest that this FEP is typical of halide perovskite and could play a role on other properties such as electron hole recombination and ionic diffusion. This model would indeed see electron and holes localized in different regions of space and potential, which would explain the long charge carriers lifetime observed.

To conclude, we recall that our analysis was developed for systems with only intrinsic disorder, and only in the context of harmonic model for atomic motion. We believe that anharmonic effects or extrinsic disorder, in the form of local defects or chemical alloying, can have an additional strong impact on MAPI's properties. Yet the results discussed in this thesis should serve as basis to go further and take these effects into account.

Bibliography

[1] J. Feng, "Mechanical properties of hybrid organic-inorganic ch3nh3bx3 (b = sn, pb; x = br, i) perovskites for solar cell absorbers," *APL Materials*, vol. 2, no. 8, p. 081801, 2014.

[2] R. Prasanna, A. Gold-Parker, T. Leijtens, B. Conings, A. Babayigit, H.-G. Boyen, M. F. Toney, and M. D. McGehee, "Band gap tuning via lattice contraction and octahedral tilting in perovskite materials for photovoltaics," *Journal of the American Chemical Society*, vol. 139, no. 32, pp. 11117–11124, 2017. PMID: 28704048.

[3] M. N. F. Hoque, N. Islam, Z. Li, G. Ren, K. Zhu, and Z. Fan, "Ionic and optical properties of methylammonium lead iodide perovskite across the tetragonal–cubic structural phase transition," *ChemSusChem*, vol. 9, no. 18, pp. 2692–2698, 2016.

[4] A. Francisco-López, B. Charles, O. J. Weber, M. I. Alonso, M. Garriga, M. Campoy-Quiles, M. T. Weller, and A. R. Goñi, "Equal footing of thermal expansion and electron–phonon interaction in the temperature dependence of lead halide perovskite band gaps," *The Journal of Physical Chemistry Letters*, vol. 10, no. 11, pp. 2971–2977, 2019. PMID: 31091105.

[5] A. D. Wright, C. Verdi, R. L. Milot, G. E. Eperon, M. A. Pérez-Osorio, H. J. Snaith, F. Giustino, M. B. Johnston, and L. M. Herz, "Electron-phonon coupling in hybrid lead halide perovskites," *Nature Communications*, vol. 7, p. 11755 EP, May 2016. Article.

[6] J. M. Frost, L. D. Whalley, and A. Walsh, "Slow cooling of hot polarons in halide perovskite solar cells," *ACS Energy Letters*, vol. 2, no. 12, pp. 2647–2652, 2017. PMID: 29250603.

[7] C. Wolf, H. Cho, Y.-H. Kim, and T.-W. Lee, "Polaronic charge carrier–lattice interactions in lead halide perovskites," *ChemSusChem*, vol. 10, no. 19, pp. 3705–3711, 2017.

[8] Y. Lan, B. J. Dringoli, D. A. Valverde-Chávez, C. S. Ponseca, M. Sutton, Y. He, M. G. Kanatzidis, and D. G. Cooke, "Ultrafast correlated charge and lattice motion in a hybrid metal halide perovskite," *Science Advances*, vol. 5, no. 5, 2019.

[9] K. T. Munson, E. R. Kennehan, G. S. Doucette, and J. B. Asbury, "Dynamic disorder dominates delocalization, transport, and recombination in halide perovskites," *Chem*, vol. 4, no. 12, pp. 2826 – 2843, 2018.

[10] Y. Imry, "Possible role of incipient anderson localization in the resistivities of highly disordered metals," *Phys. Rev. Lett.*, vol. 44, pp. 469–471, Feb 1980.

[11] J. Delahaye, C. Berger, and G. Fourcaudot, "Thouless and critical regimes in insulating icosahedral AlPdRe ribbons," *Journal of Physics: Condensed Matter*, vol. 15, pp. 8753–8766, dec 2003.

[12] Z. Ovadyahu, "Some finite temperature aspects of the anderson transition," *Journal of Physics C: Solid State Physics*, vol. 19, pp. 5187–5213, sep 1986.

[13] J. Delahaye and C. Berger, "The question of intrinsic origin of the metal-insulator transition in i-alpdre quasicrystal," *The European Physical Journal B*, vol. 88, p. 102, Apr 2015.

[14] G. Trambly de Laissardière, J.-P. Julien, and D. Mayou, "Quantum transport of slow charge carriers in quasicrystals and correlated systems," *Phys. Rev. Lett.*, vol. 97, p. 026601, Jul 2006.

[15] A. Troisi, "Charge transport in high mobility molecular semiconductors: classical models and new theories," *Chem. Soc. Rev.*, vol. 40, pp. 2347–2358, 2011.

[16] S. Ciuchi, S. Fratini, and D. Mayou, "Transient localization in crystalline organic semiconductors," *Phys. Rev. B*, vol. 83, p. 081202, Feb 2011.

[17] S. Fratini, D. Mayou, and S. Ciuchi, "The transient localization scenario for charge transport in crystalline organic materials," *Advanced Functional Materials*, vol. 26, p. 2292–2315, Jan 2016.

[18] A. Missaoui, J. Khabthani, G. Trambly de Laissardière, and D. Mayou, "Two-dimensional electronic transport in rubrene: the impact of inter-chain coupling," 02 2019.

[19] A. Biewald, N. Giesbrecht, T. Bein, P. Docampo, A. Hartschuh, and R. Ciesielski, "Temperature-dependent ambipolar charge carrier mobility in large-crystal hybrid halide perovskite thin films," *ACS Applied Materials & Interfaces*, vol. 11, no. 23, pp. 20838–20844, 2019. PMID: 31099235.

Chapter 6

General conclusion

The goal of this thesis was to study the unusual properties of hybrid perovskites, using MAPI as a case study. The perovskite materials have been the subject of intense research and exhibit very unusual properties, such as long charge carrier lifetimes, defect resistance, and overall photovoltaic and optoelectronic efficiencies. In this context we aimed to approach the problem from a fully quantum point of view. Indeed, a brief analysis of the material shows that if we consider the typical mobilities and effective masses of MAPI, $\mu = 100cm^2/(V.s)$ and $m^* = 0.15m_e$, as well as the formula:

$$\mu = \frac{e\tau}{m^*}, \tag{6.1}$$

then we find typical energies $E = \hbar/\tau \simeq 80meV$. This energy is much bigger than the thermal energy $k_BT \simeq 25meV$ and the polaron formation energy $E_{polaron} = 30meV$, that is often advanced as an hypothesis for transport in MAPI. This simple result shows that it is not obvious that transport can be treated in a semi-classical way, and brings us to study the subject from a quantum point of view.

Our starting points were methods that were already developed and used to study transport in graphene, carbon nanotubes and quasicrystals, in a way that is fully quantum. These methods, which are based on the recursion method and the polynomial expansion of functions and operators, are, to the best of our knowledge, the only ones that are able to treat non periodic systems of millions of orbitals.

These methods however, were never applied to such complex materials. Indeed all the materials that were studied so far where mono-atomic, with only one type of orbitals, and problems of spin-orbit were left untouched.

As such the first priority was to evolve the numerical programs to include the much more complex Hamiltonian of MAPI. This was done both from a physical point of view, where spin-orbit coupling, dipole moments and the likes were added to the programs, and from a optimisation point. Indeed the programs were almost completely rewritten to be as efficient as possible, and to include parallelization possibilities. This proved essential to this work as it allowed computations to be done in realistic times, over large enough system sizes. Indeed, computations that used to take weeks are often solved in a day now. We believe that we have build a powerful tool, that will prove useful in the future, and can be used on many materials. These numerical methods are presented in Chapter 2.

Then, in chapter 3, we focused on the actual modelling of MAPI, starting from the perfect structure, and adding the disorder. We developed our own set of tight-biding parameters when we realized that the parameters we used needed corrections. We built a model of disorder based on two types of Einstein oscillators. The first type of oscillators models the disorder on inter-atomic couplings due to the displacement of the atoms, while the second models the variations of the electrostatic potential due to the displacement of the charges of the atoms. The phonon modes responsible for these two phenomenon are very different, and no Einstein model with only one type of oscillator could be satisfactory. In a way this model is the simplest one could make, yet allows us to observe a lot of MAPI's characteristics features. We find that the inter-atomic couplings vary of the order of 20%, which has strong effects on the bandgap. We also find strong variations of the electrostatic potential, which creates high and low potential regions in the material. We expect such model to work well for multiple materials, including those of the perovskite family. We think that this double Einstein model approach could be an interesting alternative to the very costly molecular dynamics methods to study some specific problems like the role of local defects for example.

In chapter 4, we focused on building a model to analyse our numerical data. We call this model the Drude-Anderson model, which is built from the Drude model of transport, in which we add the possibility for electrons to backscatter. It

is based on the velocity self correlation function and gives analytical expressions for multiple variables. We also presented the elements required to arrive to this model, which are the Drude model, the phenomenon of Anderson localization, and the quantum Kubo formalism for conductivity.

Finally, in chapter 5, we simulated the electronic and transport properties of MAPI. From photo-luminescence computations, we were able to recover the experimentally observed evolution of the bandgap with the temperature. We highlighted two underlying phenomena, which have opposing effects. Indeed diagonal disorder has for effect to reduce the gap while the off-diagonal disorder widens it. These effects mostly cancel one another at room temperature, resulting in an impressive stability of MAPI's band structure to it's internal disorder. We get a good fit to experimental data of photoluminescence in the case where the energy of the LO phonon modes is chosen between 12 and $14meV$.

Then we looked at transport, as a function of disorder. The contribution brought by the MA molecule and the off-diagonal disorder are negligible for transport, and we quickly highlighted that the limiting effect for transport in room temperature MAPI are the LO phonon modes. These phonon limit the mobilities to around $100cm^2/V.s$.

In order to extract the most of our time resolved diffusion, we used the Drude-Anderson model of transport. This model fits the data very accurately. It gives us access to the fundamental properties of transport, such as mean free path, which we always find smaller than around 20Å, to the mean scattering time which is of the order of ten femtoseconds, and to the localization ratio R. From these results we were able to discuss the possibility of polaron formation, which we find unlikely at room temperature.

The localization ratio R helped us understanding how important the localization effect in MAPI actually are. It also allowed us to include the effect of dephasing by lattice dynamics in our model. This dephasing has for effect to break quantum localization, and increases mobilities by a factor of two in the less disordered cases, and even more as disorder increases. This results in almost non conducting samples becoming conductive. We propose a model for transport close to the Thouless regime, which we call adiabatic quantum localization. In this model, the charge carriers localize quickly, as they are localized by the potential

variations. But, as the atoms move, the potential evolves, and the carriers are able to follow the evolution and diffuse through the material. As such the diffusion happens at a rate proportional to the frequency of the modes. This model is an intermediate between metallic and standard hopping, in the sense that the diffusion is driven by the dynamics of the lattice. We conclude this chapter 5 by highlighting the importance of the inner fluctuating electrical potential on the transport properties of the material. We show that this potential is important above the Debye temperature and could play a role for other properties such as electron hole recombination, and ionic diffusion. We also believe it could exist in other materials with low LO phonon energy and high Born charges.

To conclude, the contribution of this thesis is threefold. First, improvements made in the numerical programs and methods, will be kept for further use. Then, from a theoretical point of view, we developed the two Einstein oscillators models, the Drude-Anderson model, and the adiabatic quantum localization scenario. We believe that the models we built during this journey proved powerful tools to understand the physics of the material. Finally, we emphasize the peculiarity of the disordered electric potential created in these systems by thermal disorder. The displacement around the equilibrium positions are large, at $\pm 10\%$ of the interatomic distance, which, coupled to large Born charges, leads to the creation of a fluctuating electric field in the material. We expect this behaviour to be a common feature of the hybrid perovskite family.

Appendix A

2D perovskites

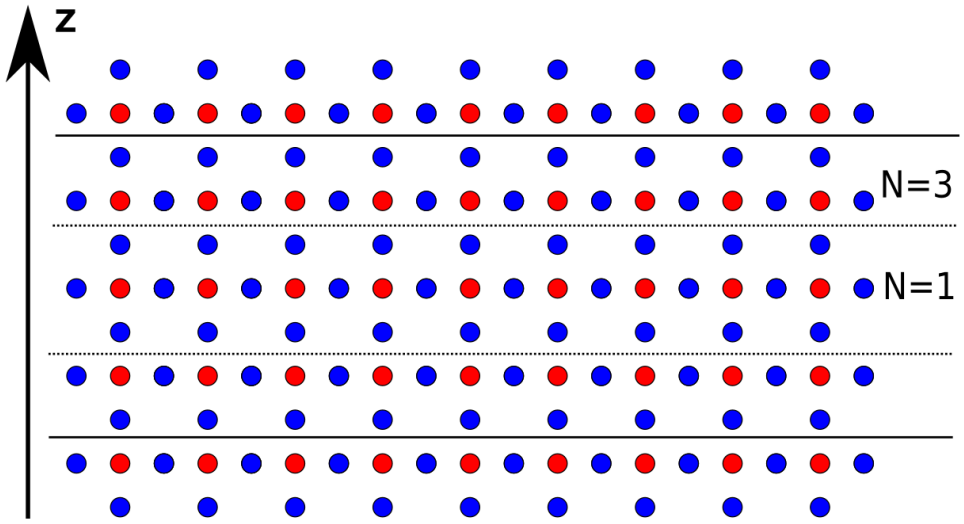

Figure A.1: Schematic of the cuts made in the material, for perovskite thickness of 1 and 3 unit cells. The medium is considered infinite in the X and Y directions.

Perovskite can be developed as 2D structure by the addition of organic non conductive layers in between plans. These perovskite can be made to be of various width, depending on the concentration of organic reagent during the growth process [1]. They offer greater stability compared to bulk perovskite due to the additional protection brought by the organic layers. They also have interesting optoelectronic properties, that appears when the dimension of the layers reduce.

These properties include a large exciton binding energy, increased and tunable band gap, and high photo-luminescence yield.

Disorder in these layers is non trivial to assess using the tools we developed for bulk MAPI. Due to the insulating non polar nature of the organic inter layers, the number of dipole moment is diminished, but they also provide no screening of the potential, and it has been showed that the dielectric constant varied in the perovskite layer according to distance from the insulating region, dropping to $\epsilon_r \simeq 1$ at the contact.

As such we focus mainly on the effect that pure quantum confinement has in these material. To do so, we consider a sample of bulk MAPI, with the disorder associated, from which we will cut slices of perovskite. Doing so, the disorder is unchanged and only the thickness of the system changes, such a slice can be seen in figure A.1. We do not consider the physics of exciton separation in these material, while they are useful in optoelectronics, solar application requires the separation of the charges for current to appear, and we only consider transport assuming they can split.

Quantum confinement shows that MAPI's bandgap can be tuned by changing the layer thickness as shown in figure A.2, which is useful in optoelectronic components, but might prove detrimental to solar cell applications if it deviates too much from the Shockley optimum. However the Shockley optimum only gives information about the maximum efficiency of a solar cell, while the most interesting characteristic of a solar cell is the energy generated over it's lifetime

$$E = P_{sun}\mu\tau, \tag{A.1}$$

where P_{sun} is the average solar energy reaching the panel, $\mu*$ it's efficiency and τ it's lifetime. As such, a small decrease in efficiency might still be profitable if the increase in lifetime is large enough.

When looking at the photo-luminescence spectra in figure A.2, we can see that the bandgap increases when the thickness decreases, in a non-linear fashion. This is the expected and experimentally observed behaviour. As such, the bandgap up to samples 5 cells thick is not changed much, but changes very quickly if one goes further beyond. The absolute value of the bandgap is however underestimated in

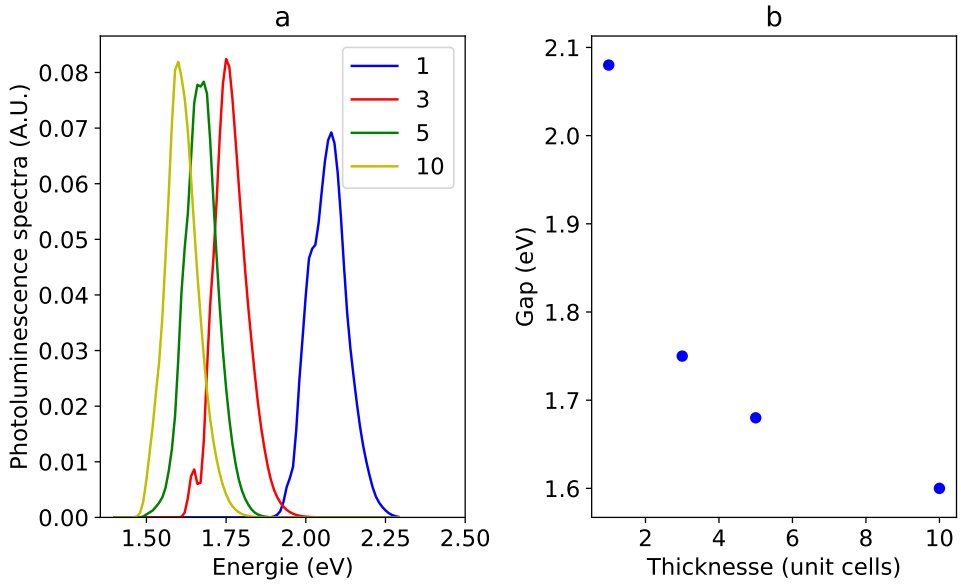

Figure A.2: **(a)**: Variation of the photo-luminescence spectra with respect to the thickness of the 2D layers. The maximum of intensities, corresponding to the bandgaps, are plotted as a function of the thickness in **(b)**. These results are for $\omega_{LO} = 12meV$.

our model, as we consider the potential in 2D MAPI to be the same as is the bulk material, which is an overestimation of the potential.

We show results of diffusion on 2D perosvskite cuts of different width in figure A.3. We find that quantum confinement strongly restricts mobilities in MAPI. Results with samples one cell thick show effects of confinement as strong as the most disordered samples of bulk MAPI we selected. These mobilities are expected to be even lower as extrinsic disorder is added, and is coherent with the measured mobilities. In this scenario the dephasing effect of the lattice appears to be the dominating factors, as charge carriers appear completely localized otherwise. These quantum confinement effects on mobilities and bandgap appear when samples are less than 10 cells thick. This implies that a trade-off in bandgap and mobilities with cell lifetime and stability is possible and 2D perovskite should not be ruled out completely for solar cell applications, even though the thinnest samples might not be the solution.

Studies have shown that 10 cells thick 2d perovskite show decrease of efficiency

of a few percent over 1440 hour illumination time, compared to 15% for bulk MAPI and an increase by a factor of a 100 in decomposition lifetime in humid environment [2]. Because of the quick variation of the bandgap away from the optimal value, and the drop in mobilities when going to small system size, we believe that perovskite less than 5 to 10 cells thick are better suited for optoelectronic devices than photovoltaic cells. Perovskite up to 10 cells small should however remain most of the interesting properties of 3D MAPI, while exhibiting highly increased lifetimes.

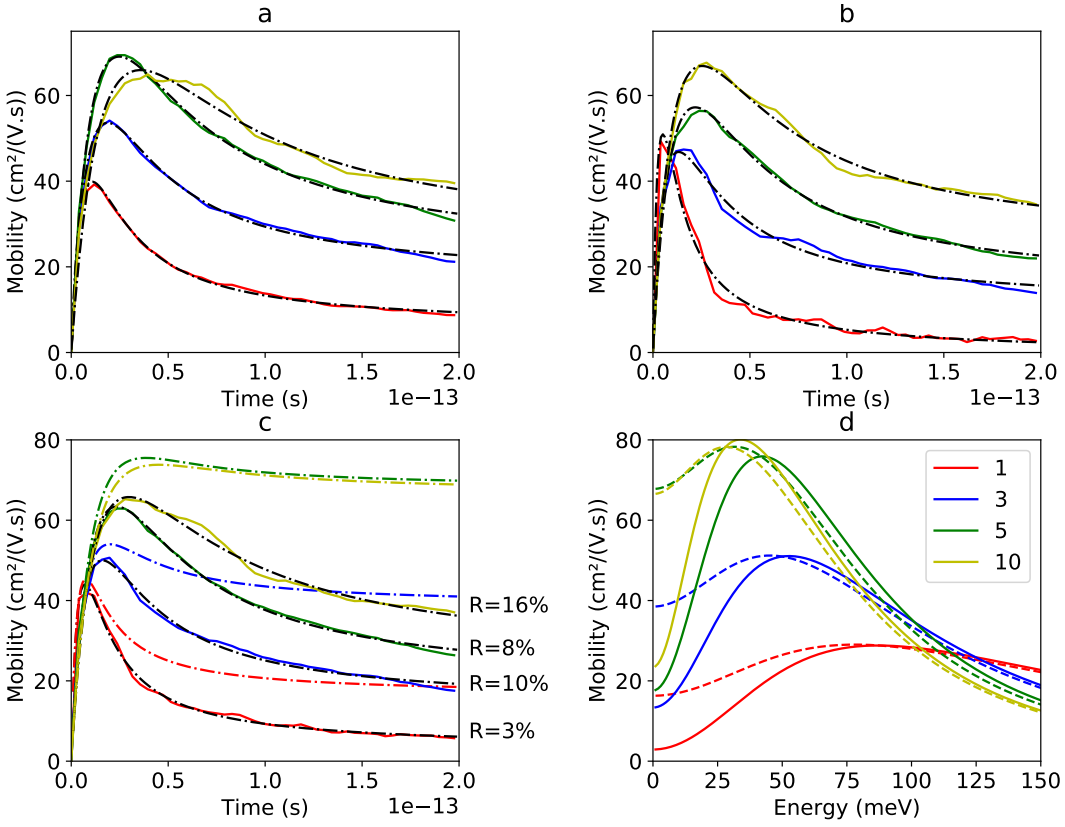

Figure A.3: Thermodynamically averaged mobilities as function time for different thickness, for holes **(a)**, electrons **(b)**, and averaged over both types of carrier **(c)**. The data *(full line)* are fitted using the Drude-Anderson model *(black dashed line)*. We derive from the fitted parameter the localisation ratio R and the mobilities with a de-phasing time $\tau_\phi = 1/\omega_{LO}$ *(coloured dotted line)*. We also compute from the parameters the static and dynamic mobility as a function of energy **(d)**.

Bibliography

[1] C. Lan, Z. Zhou, R. Wei, and J. C. Ho, "Two-dimensional perovskite materials: From synthesis to energy-related applications," *Materials Today Energy*, vol. 11, pp. 61 – 82, 2019.

[2] L. N. Quan, M. Yuan, R. Comin, O. Voznyy, E. M. Beauregard, S. Hoogland, A. Buin, A. R. Kirmani, K. Zhao, A. Amassian, D. H. Kim, and E. H. Sargent, "Ligand-stabilized reduced-dimensionality perovskites," *Journal of the American Chemical Society*, vol. 138, no. 8, pp. 2649–2655, 2016. PMID: 26841130.

Appendix B

Results with the first set of parameters

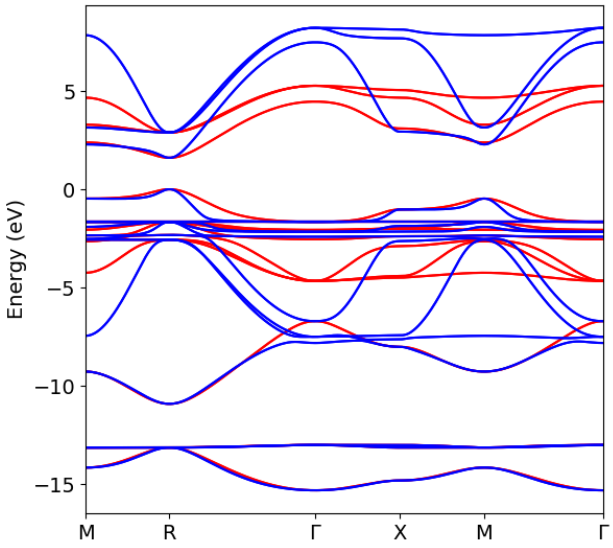

Figure B.1: Band structure of MAPI with different parameters. Our parameters are shown in red while the parameters of Boyer-Richard *et.al.* are shown in blue.

Here we show some of the results we had of quantum diffusion and photoluminescence on MAPI, using the parameters of Boyer-Richard *et.al.*. We realized in the middle of the summer of 2020 that these parameters were giving effective masses of around $0.07m_e$ for both holes and electrons, which is inconsistent with

the experimentally observed masses, and the band structure computed *ab-initio*. We traced the error to the parameter pp_σ which was approximately two times too big. We show the differences in band structure in figure B.1.

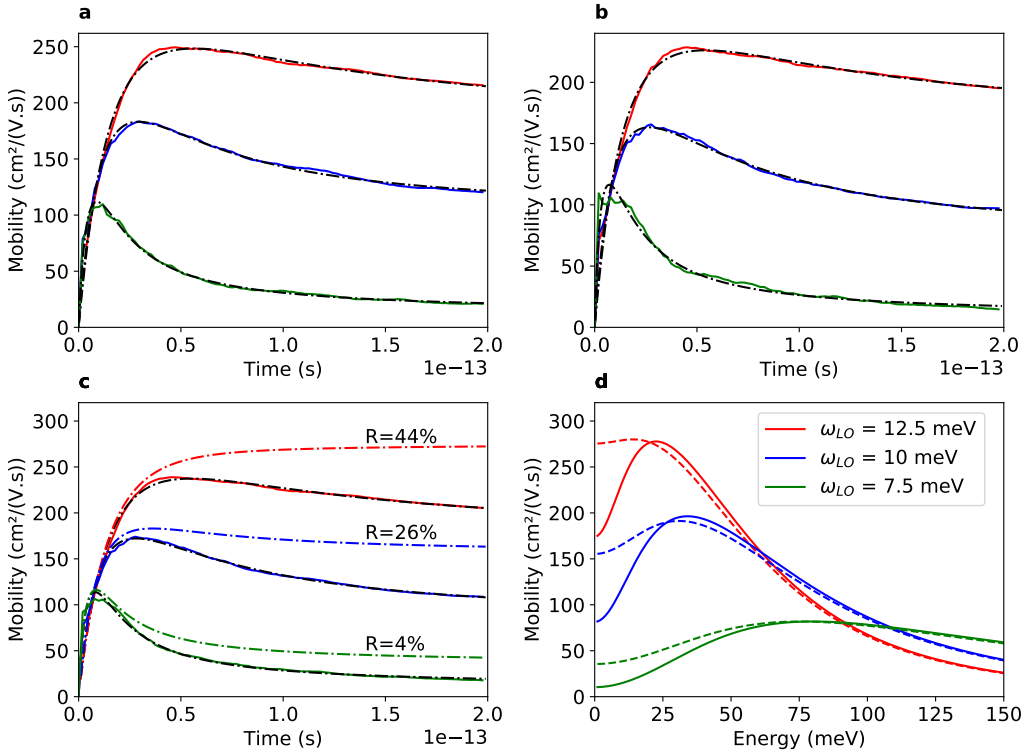

e

ω_{LO} (meV)	C_c $(10^{11}m^2/s^2)$	τ_c (fs)	C_B $(10^{11}m^2/s^2)$	τ_B (fs)	Mean free path (Å)	R (%)
12.5	2.30	8.92	0.26	44.17	24.02	43.87
10	2.94	5.61	0.41	29.96	16.72	25.55
7.5	6.53	2.24	1.57	9.00	9.19	3.66

Figure B.2: Thermodynamically averaged mobilities as a function of time for different values of ω_{LO}, for holes **(a)**, electrons **(b)**, and averaged over both types of carrier **(c)**. The data *(full line)* are fitted using the Drude-Anderson model *(black dashed line)*. We derive from the fitted parameter the localisation ratio R and the mobilities with a de-phasing time $\tau_\phi = 1/\omega_{LO}$ *(coloured dotted line)*. We also compute from the parameters the static and dynamic mobility as a function of energy **(d)**. The fitted parameters are shown in **(e)**.

Luckily with the progressed we made in the numerical program, we were able to

redo the computations with updated parameters. We still present here the results we obtained with these low effective masses, as we believe these could also prove useful in the study of other materials, and because it shows the resilience of our findings to the tight binding parameters.

These results are for a slightly bigger disorder than the one presented in the transport chapter, as at the time we considered value of the relative dielectric constant $\epsilon_r = 5$, and slightly lower values of ω_{LO}.

This gives us mobilities approximately two to three time bigger than what we found with our corrected parameters, as shown in figure B.2. This is expected as the effective mass is also bigger by such a factor. The scattering time and localization factor however remain in the same range, and the Drude-Anderson model fits the data equally well. For comparable values of mobilities the mean free path are of the same order. To us this reinforces the idea that the electrical disorder plays a major role in these perovskites, and that it is mostly this field, with it's values and spatial coherence, that defines the transport properties of the material.

Indeed, despite the factor two on the mobility values, the localization factors are also important, as they are always below 40%, and the lattice dynamics also has a strong impact on the mobilities.

When looking at the effect of temperature on mobilities, as shown in figure B.3, we find that the power law in $T^{-3/2}$ is also observed here, and transport is still not thermally activated in this scenario. We do not show results of photoluminescence as the computations were never carried out to the end for this set of parameters, but the tendency for diagonal disorder to decrease the bandgap and the tendency of off-diagonal disorder where also observed within this framework, while never quantified.

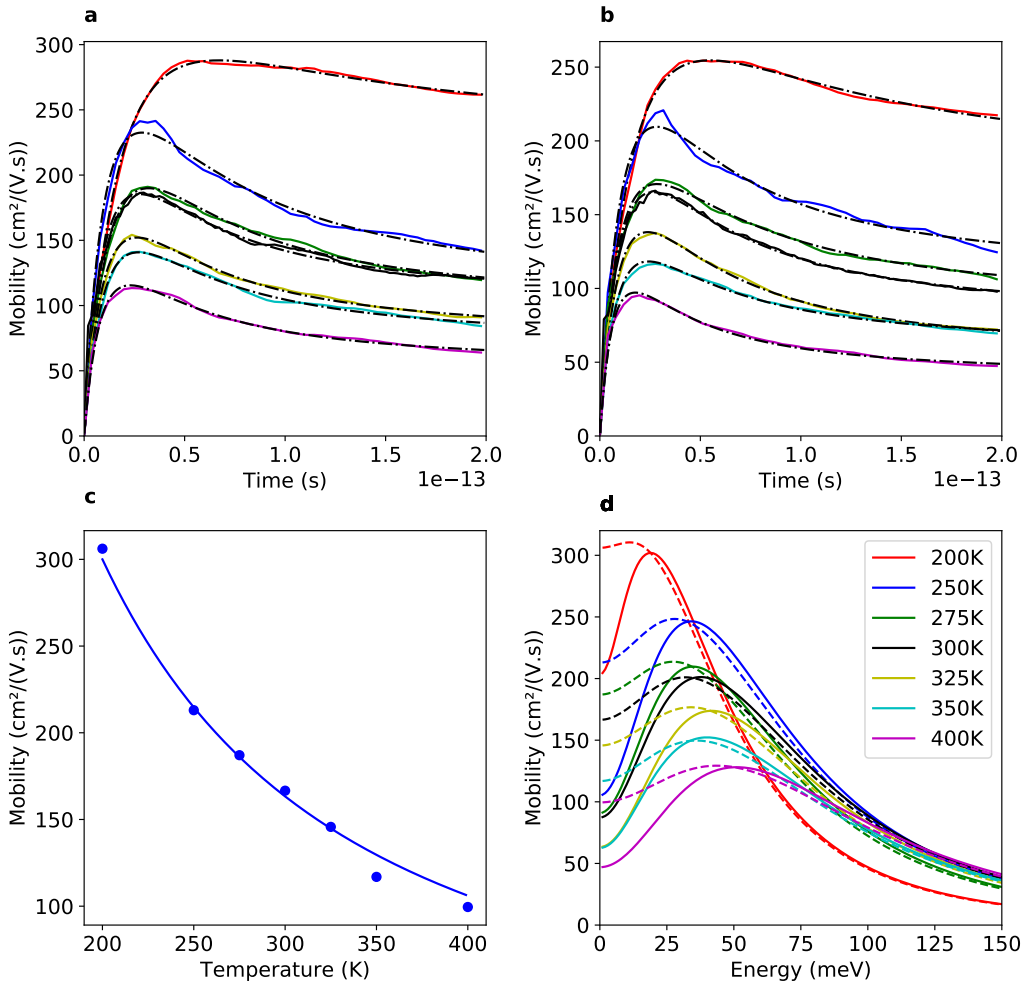

Figure B.3: Results for $\omega_{LO} = 10meV$ and $\epsilon_r = 5$. Thermodynamically averaged mobilities as function of time for different temperatures, for holes **(a)**, electrons **(b)**. The data *(full line)* are fitted using the Drude-Anderson model *(black dashed line)* **(c)** : Thermodynamically averaged mobilities as function of temperatures. The data *(blue dots)* are shown with a de-phasing time $\tau_\phi = 1/\omega_{LO}$, and fitted via a power law in $T^{-3/2}$. We derive from the parameters the static and dynamic mobility as function energy **(d)**, with and without dephasing.

Résumé en français

Le but de cette thèse est d'étudier les propriétés des pérovskites hybrides, en utilisant la pérovskite $MAPBI_3$ comme cas d'étude. Ces matériaux ont été le sujet de recherches intenses et font preuve de propriétés inhabituelles, tel que de longues durées de vies des porteurs de charge, une haute résistance aux défauts, et de hauts rendements photovoltaïques en général. Dans ce contexte, nous souhaitons approcher le problème d'un point de vue entièrement quantique. En effet, un brève analyse des propriétés du matériau montre que si l'on considère les mobilités et masses effectives typiques de MAPI, $\mu = 100cm^2/(V.s)$ et $m^* = 0.15me$, ainsi que la formule

$$\mu = \frac{e\tau}{m^*}, \tag{B.1}$$

alors nous trouvons des énergies caractéristiques $E = \hbar/\tau \simeq 80meV$. Cette énergie est bien plus grande que l'énergie thermique $k_BT \simeq 25meV$ et que l'énergie de formation du polaron $E_{polaron} \simeq 30meV$, souvent avancé comme hypothèse concernant le transport dans MAPI. Ce simple résultat montre qu'il n'est pas évident que le transport puisse-t-être traité de manière semi-classique, ce qui nous pousse vers une approche quantique du sujet.

Notre point de départ sont les méthodes qui ont déjà été développées et utilisées pour étudier le transport dans des matériaux tels que le graphène, les nanotubes de carbone ou les quasi-cristaux. Ces méthodes, qui sont basées sur la méthode de récursion et le développement en séries de polynômes de fonctions et d'opérateurs, sont, à notre connaissance, les seules capables de traiter des systèmes non périodiques de plusieurs millions d'orbitales. Cette méthode est complètement quantique et comprend entièrement la nature ondulatoire de l'électron, et les possibles interférences quantiques associées. En revanche, ces méthodes n'ont encore jamais été appliquées à des matériaux aussi complexes. En effet, tout les matériaux étudiés jusqu'à présent étaient mono-atomiques, avec un seul type d'orbitale, et ne contenaient pas de problèmes de spin-orbite.

Ainsi la première priorité a été de développer les programmes numériques pour prendre en compte l'hamiltonien beaucoup plus complexe de MAPI. Ces programmes ont été modifié à la fois d'un point de vue de la physique qu'ils conti-

ennent, avec l'addition des problématiques de spin-orbite, de moments dipolaires et autres, mais aussi d'un point de vue d'optimisation. Ainsi les programmes ont été pratiquement entièrement réécris pour être aussi rapides que possibles, et pour pouvoir résoudre les problèmes de manière parallèle. Ceci s'est avéré essentiel, en permettant à nos calculs de pouvoir être résolus en des temps acceptables. En effet, des calculs qui prenaient auparavant des semaines sont maintenant souvent résolus en une journée. Nous pensons que cet outils sera utile dans le futur, car il peut être utilisé sur de nombreux matériaux. Toutes ces méthodes sont présentées dans le Chapitre 2 de la thèse.

Ensuite, dans le chapitre 3, nous nous sommes penché sur la modélisation de MAPI, en commençant avec sa structure parfaite, avant d'introduire du désordre thermique. Nous avons développé notre propre jeu de paramètres après avoir réalisé que ceux que nous utilisions avaient besoin de corrections. Nous avons créé un modèle de désordre basé sur deux types d'oscillateurs d'Einstein. Le premier type d'oscillateur sert à modéliser le désordre sur les couplages inter-atomiques causé par le mouvement des atomes, alors que le deuxième type sert à modéliser les variations du champ électrostatique causées par le déplacement des charges des atomes.

Les modes de phonon responsables de ces deux phénomènes ont des énergies différentes, et aucun modèle d'Einstein avec un seul type d'oscillateur ne pourrait rendre compte des deux phénomènes. Nous trouvons que les couplages entre atomes varient fortement à cause du désordre, de l'ordre de 20%, ce qui a de forts effets sur le gap. Nous trouvons aussi que les variations du champ électrostatique sont importantes, et créent des régions de haut et bas potentiels dans le matériau, comme montré dans la figure B.4. Nous avons montré que pour le potentiels nous n'avions qu'une seule variable,

$$W = \frac{\sqrt{k_B T}}{\epsilon_r \omega_{LO}}, \tag{B.2}$$

ou T est la température, ϵ_r est la permittivité relative de MAPI, et ω_{LO} est l'énergie des phonons longitudinaux optiques. Ce modèle est, d'une certaine manière, le plus simple que nous puissions créer, mais nous permet pourtant d'observer beaucoup des propriétés de MAPI. Nous nous attendons à ce que ce

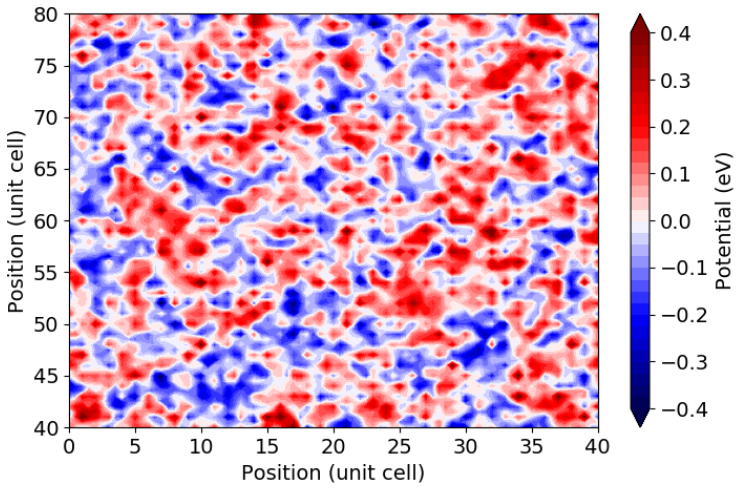

Figure B.4: Intensité du potentiel électrique causé par les phonons LO en fonction de la position pour une coupe dans un échantillon de MAPI. Les paramètres du désordre sont $W = \frac{\sqrt{k_B T}}{\epsilon_r \omega_{LO}}$, avec $\epsilon_r = 6$, $T = 300K$ et $\omega_{LO} = 12meV$.

genre de modèle marche bien pour plusieurs matériaux, y compris ceux de la famille des perovskites, dans lequel les charges de Born sont grandes, et où les fréquences des phonons acoustiques et longitudinaux optiques (LO) sont très différentes. Nous pensons que ce modèle d'Einstein a deux types d'oscillateurs peut être une approche alternative intéressante à la dynamique moléculaire, très couteuse, pour étudier des problèmes spécifiques, tels que le rôle de défauts locaux par exemple.

Dans le chapitre 4, nous construisons le modèle de Drude-Anderson, qui nous permet d'analyser finement nos résultats. Ce modèle est basé sur le modèle de Drude, dans lequel nous ajoutons le phénomène de backscattering pour les électrons. Ce modèle se base sur l'autocorrélation de la vitesse, et donne une forme analytique a de nombreuses variables. Nous présentons également le formalisme nécessaire pour arriver à ce modèle.

Enfin, dans le chapitre 5, nous simulons les propriétés de transport de charges de MAPI. Nous réalisons d'abord des simulations de photoluminescence, avec lesquels nous retrouvons l'évolution observée expérimentalement du gap de MAPI avec la température. Nous mettons en avant deux phénomènes qui ont des effets opposés. En effet, le désordre électrostatique à pour effet de réduire le gap de MAPI en poussant des états dans la zone interdite, alors que le désordre sur

les couplages inter-atomique a pour effet de repousser les niveaux d'énergie, et d'augmenter le gap. Ces effets ont tendance à s'annuler à température ambiante, ce qui a pour résultat une impressionnante résistance du gap de MAPI au désordre. De ces résultats nous trouvons que l'énergie naturelle des phonons LO se situe entre 12 et $14meV$.

Ensuite nous avons regardé comment le désordre affectait le transport de charges. Nous montrons rapidement que les phonons LO sont le facteur limitant les mobilités dans MAPI, alors que le désordre sur les couplages inter-atomiques et celui apporté par la molécule de méthylammonium sont négligeables pour le transport. Ces phonons limitent les mobilités a des valeurs de $100cm^2/(V.s)$, comme montré dans la figure B.5. Afin d'extraire le plus d'informations de notre diffusion résolue en temps, nous utilisons le modèle de transport de Drude-Anderson.

Ce modèle permet un très bon fit des données et nous donne accès aux propriétés fondamentales du transport. Ainsi nous avons accès au libre parcours moyen, que nous trouvons toujours inférieur à environ 20Å, au temps de libre parcours moyen, qui est de l'ordre de la dizaine de femtosecondes, et au rapport de localisation. Ce dernier nous indique l'impact des effets de localisation sur les mobilités. Le facteur R est défini comme le ratio entre la mobilité réelle, et la mobilité sans effets de localisation. Ce modèle nous a permis de nous rendre de compte de l'importance des effets de localisation dans MAPI, qui réduisent au minium de moitié les mobilités, et peuvent même complètement localiser les porteurs de charge.

Ce modèle nous permet également d'insérer des effets de déphasages causés par la dynamique du réseau. Ce déphasage vient briser le confinement des porteurs de charge, et augmente les mobilités par deux dans les cas les moins désordonnés, et plus encore quand le désordre augmente. Ceci a pour effet de rendre des échantillons pratiquement isolants conducteurs. Avec ces résultats nous pouvons discuter de la possibilité de formation de polarons dans MAPI, que nous jugeons improbable à température ambiante, à cause du rôle dominant des phonon LO, qui viennent détruire cet état. Nous proposons a la place un modèle de diffusion proche du modèle de Thouless. Ce mode de diffusion devient important dans MAPI lorsque les mobilités tombent en dessous de $30cm^2/(V.s)$. Dans ce modèle, les porteurs de charges sont rapidement localisés par le désordre électrostatique. Mais,

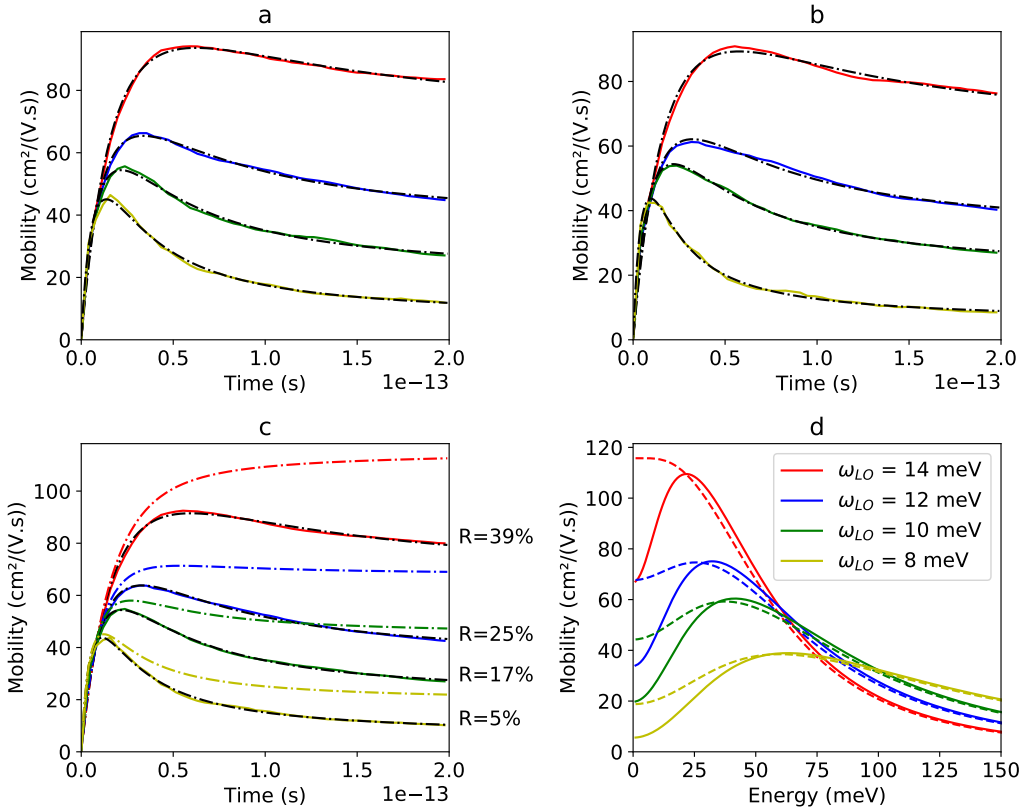

Figure B.5: Mobilités moyennées thermodynamiquement en fonction du temps pour différentes valeurs de ω_{LO}, pour les trous **(a)**, et les électrons **(b)**, et moyennée sur les deux types de porteur de charge **(c)**. Les données *(lignes continues)* sont fittées par le modèle de Drude-Anderson *(lignes noires pointillées)*. Nous dérivons des paramètres fittés le facteur de localisation R et les mobilités avec un temps de déphasage $\tau_\phi = 1/\omega_{LO}$ *(lignes colorées pointillées)*. Nous calculons aussi grâce aux paramètres la conductivité optique, en unité de mobilité **(d)**.

quand les atomes bougent et que le potentiel évolue, les porteurs de charge sont alors capables de suivre l'évolution du potentiel et de diffuser à travers l'échantillon. Ce régime est différent des régimes usuels de diffusion de bande ou de diffusion par sauts thermiquement activés.

Pour conclure sur les résultats de cette thèse. D'abord, les améliorations apportées aux méthodes et programmes numériques seront transmises et réutilisées. Ensuite, d'un point de vue théorique, nous avons développé un modèle d'Einstein avec deux types d'oscillateurs, le modèle de Drude-Anderson, et le modèle de dif-

fusion entrainée par le réseau. Nous pensons que ces modèles sont une approche originale de ces problèmes, et ont été des outils puissants dans notre compréhension de MAPI. Finalement, en terme de résultats, nous pensons avoir apporté des éclaircissements quand aux phénomènes intrinsèques à MAPI, quand à leur rôle, et aux limitations qu'ils apportent sur les mobilités. Nous pensons également que ces phénomènes peuvent être étendus au reste de la famille des perovskites hybrides.

Resumé

Les pérovskites halogénées sont des matériaux très prometteurs dans de nombreux domaines, allant du photovoltaïque à la détection des rayons X. Dans ce contexte nous cherchons à modéliser leur propriétés de structure électronique et de transport, et avons réalisé une étude de la pérovskite MAPbI3 (MAPI). Nous avons donc développé un modèle décrivant le désordre thermodynamique dans MAPI, et approchons le problème de la structure électronique et du transport de manière purement quantique. Ainsi nous déterminons l'impact du désordre sur la structure électronique et le gap semi-conducteur. Nous observons aussi que les phonons longitudinaux optiques limitent les mobilités à des valeurs d'environ $100cm^2/(V.s)$. De plus les effets de localisation sont forts, même dans les cas avec du désordre thermique uniquement. Dans certain cas avec un désordre supplémentaire, où la mobilité est inférieure à $30cm^2/(V.s)$, les porteurs de charges sont même pratiquement totalement localisés, mais cette localisation est brisée par la dynamique du réseau. Ce régime est différent des régimes usuels de diffusion de bande ou de diffusion par sauts thermiquement activés.

Abstract

Halide perovskites are very promising materials in various domains, ranging from photovoltaic to X-ray detection. In this context, we aim to model their electronic structure and transport properties, and have made a study of the perovskite MAPbI3 (MAPI). We developed a model describing thermodynamical disorder in MAPI and we approach the problem of electronic structure and transport from a purely quantum point of view. We determined the impact of disorder on the electronic structure and the semi-conductor bandgap. We also observed that the optical longitudinal phonons limit the mobilities to values around $100cm^2/(V.s)$. Furthermore, the quantum localisation effects are strong , even in cases with only thermal disorder. In some cases with additional disorder, where the mobility is below $30cm^2/(V.s)$, the charge carriers are almost totally localized, but this localisation is broken by the lattice's dynamic. This regime is different from the usual regimes of band diffusion or diffusion via thermally activated hopping.